# Tobacco Mosaic Virus coat protein disks as versatile templates for self-assembly

Omar Zahr

Department of Chemistry

McGill University

Montreal, Quebec, Canada

H3A 0B8

December, 2014

A thesis submitted to McGill University in partial fulfillment of the requirements of the degree of Doctor of Philosophy

# Table of Contents


| | | |
|---|---|---|
| | Abstract | v |
| | Acknowledgements | ix |
| | List of abbreviations | xi |
| | List of figures | xii |
| Chapter 1 | An overview of plasmonics and metamaterials | 1 |
| 1.1 | Plasmonics | 2 |
| 1.1.1 | Maxwell's equations | 3 |
| 1.1.2 | The dielectric function of the free electron gas | 5 |
| 1.1.3 | Plasmon modes of a sub-wavelength spherical nanoparticle | 7 |
| 1.1.4 | Considerations for real metals | 17 |
| 1.1.5 | Plasmon coupling | 18 |
| 1.1.6 | Summary | 22 |
| 1.2 | Negative index metamaterials | 23 |
| 1.2.1 | Artificial magnetism | 26 |
| 1.2.2 | Optical frequency metamaterials | 28 |
| 1.2.3 | Nanoparticle rings as optical metamaterials | 29 |
| 1.2.4 | Effective medium theory and the Maxwell-Garnet model | 32 |
| 1.2.5 | Loss and Q-factor | 35 |
| 1.3 | Summary | 36 |
| Chapter 2 | Biological templates for self-assembly and the Tobacco Mosaic Virus coat protein | 40 |
| 2.1 | Top-down, bottom-up | 41 |
| 2.1.1 | Lithography for nanostructure fabrication | 41 |
| 2.1.2 | Bottom-up self-assembly | 43 |
| 2.2 | Biological templates for self-assembly | 44 |
| 2.2.1 | DNA and protein templated self-assembly | 44 |
| 2.2.2 | An introduction to viruses | 47 |
| 2.2.3 | Viruses and VLPs in nanotechnology | 48 |
| 2.3 | The Tobacco Mosaic virus | 51 |
| 2.3.1 | Self-assembly of the Tobacco Mosaic virus coat protein | 53 |
| 2.3.2 | TMV and TMV capsids as templates for bottom-up self-assembly | 55 |
| 2.3.3 | Expression of the Tobacco Mosaic virus coat protein | 56 |
| 2.4 | Summary | 57 |

| | | |
|---|---|---|
| Chapter 3 | Gold nanoparticle rings on Tobacco Mosaic Virus coat protein disks by intermolecular interaction | 64 |
| 3.1 | Introduction | 65 |
| 3.2 | Site directed mutagenesis for templated ring assembly | 66 |
| 3.3 | Synthesis of BSPP-passivated nanoparticles | 67 |
| 3.4 | Assembly of nanoparticle rings | 68 |
| 3.5 | Monitoring nanoparticle rings by UV-Vis spectroscopy | 72 |
| 3.6 | Fluorescence spectroscopy | 74 |
| 3.7 | Gel electrophoresis and nanoparticle incorporation rate | 75 |
| 3.8 | Methods | 77 |
| 3.9 | Conclusions | 80 |
| Chapter 4 | Covalent modification of TMV coat protein N-terminus | 83 |
| 4.1 | Introduction | 84 |
| 4.2 | Conjugation of proteins by carbodiimides | 85 |
| 4.3 | Functionalization of S123C TMV coat protein N-terminus with α-lipoic acid | 87 |
| 4.4 | Functionalization of wild-type TMVcp N-terminus with 5-azidopentanoic acid | 94 |
| 4.5 | Methodologies | 96 |
| 4.6 | Conclusion | 97 |
| Chapter 5 | Gold nanoparticle rings on N-terminally modified TMVcp disks | 100 |
| 5.1 | Introduction | 101 |
| 5.2 | Assembly of nano-rings on α-lipoic acid functionalized TMVcp | 102 |
| 5.3 | Monitoring the growth of ring solutions using UV-Vis spectroscopy | 105 |
| 5.4 | Dark-field scattering spectroscopy and imaging | 106 |
| 5.5 | Methodologies | 109 |
| 5.6 | Conclusion | 110 |
| Chapter 6 | Azide-terminated TMVcp as a platform for click chemistry | 112 |
| 6.1 | Introduction | 113 |
| 6.2 | Fluorescein alkyne derivative to probe TMVcp conjugate efficiency | 116 |

| | | |
|---|---|---|
| 6.3 | Functionalization of TMVcp with polylysine and polyethyleneoxide by CuAAC | 117 |
| 6.4 | TMVcp-DNA hybrids for templated assembly of DNA conjugated gold nanoparticles | 123 |
| 6.5 | Methodologies | 125 |
| 6.6 | Conclusion | 126 |
| Chapter 7 | Conclusions and future work | 130 |
| 7.1 | Conclusion | 131 |
| 7.2 | Future work | 133 |

# Abstract

The field of metamaterials – nanostructured materials that possess effective optical properties undiscovered in nature - has illustrated the utility of plasmonically coupled nanostructures for the manipulation of electromagnetic radiation in novel ways. A negative refractive index has been predicted in systems of plasmonically coupled metal nanoparticles. Currently, efforts to construct such systems are limited by the difficulties presented in fabricating such structures at the required size scales. The use of capsid proteins as templates for the self-assembly of inorganic components simplifies the parallel fabrication of nanostructured materials on scales that are costly to achieve using lithographic techniques. Described herein is the use of Tobacco Mosaic Virus coat protein disks as templates for the self-assembly of gold nanoparticles to form plasmonically coupled nanoparticle rings in solution.

Reported in chapter 3 is the assembly of gold nanoparticles functionalized with bis(p-sulfonatophenyl)phenylphosphine (BSPP) on the surface of TMVcp 20S disks. The assembly is thought to be driven by hydrogen bonding between sulfonic acid moieties of BSPP and arginine 61 residues that circumscribe the upper face edge of the 20S disk. Additional nanoparticles can be introduced into the center of these rings by a similar interaction. The population of rings with central nanoparticles can be controlled with pH, which alters the protonation state of carboxylic acids adjacent to the center of the rings. In this manner the degree of electrostatic repulsion felt by the nanoparticles is changed. Solutions of these rings show intriguing absorption properties that are affected by pH due to the changing populations of rings with central nanoparticles.

To produce rings that are more precisely arranged and to allow one to take advantage of the intrinsic self-assembly properties of TMVcp, a method to bind nanoparticles to the edge of the disks rather than on the upper face was desired. Chapter 4 describes the attempted modification of the TMVcp N-terminus with α-lipoic acid using carbodiimide chemistry to provide handles for the binding of gold nanoparticles around the edge of the disks. Also reported is the attachment of 5-azidopentanoic acid to the N-terminus in an effort to create a

system that could take advantage of the more versatile azide-alkyne cycloaddition, 'click-chemistry' scheme. Both systems have been met with limited success due to what is believed to be a steric constraint on the availability of the N-terminus to reaction.

Chapter 5 describes the attachment of gold nanoparticles to α-lipoic acid modified TMVcp. It is found that despite the partial modification of the protein, rings can still be obtained around the edge of the disks due to the tendency of BSPP functionalized gold nanoparticles to associate in linear chains at certain ionic strength conditions. These rings also display interesting optical properties which have been obtained by dark-field spectroscopy, encouraging the possibility that such structures may display metamaterial behavior in solution.

5-azidopentanoic acid modified TMVcp is utilized as a click platform in chapter 6 in the attachment of synthetic polymers to modify the self-assembly properties of TMVcp itself. Also reported is the attempted attachment of nucleotide strands for the assembly of gold nanoparticles conjugated to complimentary nucleotide sequences. Both these efforts are severely hampered by the low modification yield of TMVcp due to the hindered N-terminus.

# Résumé

Le domaine des métamatériaux, c'est-à-dire des matériaux qui possèdent des propriétés optiques utiles et qui n'existent pas à l'état actuel, a déjà mis en évidence l'utilité de nanostructures couplés à un plasmon en manipulation du rayonnement électromagnétique de façons novatrices. Les propriétés telle que l'indice de réfraction négatif sont postulées dans les systèmes incorporant des nanoparticules qui exhibent le couplage plasmonique. Présentement, l'enquête est limitée par les difficultés à produire ces structures avec les mesures nécessaires. L'incorporation de protéines de capside comme modèles pour l'auto-assemblage de constituants inorganiques aide dans la fabrication en parallèle de nanomatériaux avec des mesures qui seraient couteux à atteindre par la lithographie. La présente dissertation décrit l'utilisation des protéines de capside du virus mosaïque du tabac comme infrastructures pour l'auto-assemblage de nanoparticules d'or en anneaux qui exhibent le couplage plasmonique en solution.

Le chapitre 3 aborde l'assemblage de nanoparticules d'or liées au bis(p-sulfonatophényle)phénylephosphine (BSPP) sur la surface de disques de protéine TMVcp 20S. La formation de liaisons hydrogène entre les regroupements d'acide sulfonique du BSPP et des résidus d'arginine-61 qui cernent le bord de la surface supérieure du disque 20S dirige ce processus. Des nanoparticules supplémentaires peuvent être introduites au centre de ces anneaux à l'aide d'interactions semblables. La population de nanoparticules au centre des anneaux peut être contrôlée en changeant le pH, qui engendre des changements dans l'état de protonation d'acides carboxyliques près du centre de ceux-ci. En ce faisant, le degré de répulsion électrostatique ressenti par les nanoparticules change. Les solutions de ces anneaux exhibent de fascinantes propriétés d'absorption dépendant du pH à cause du changement dans le nombre d'annaux qui comportent toujours des nanoparticules au centre. Afin de produire des anneaux qui sont arrangés de façon plus précise et de faciliter l'exploitation des propriétés d'auto-assemblage propres au TMVcp, une méthode de lier les nanoparticules au bord des disques, plutôt qu'à la surface supérieure, a été désirée. Le chapitre 4 décrit les tentatives de modification de la terminaison aminée du TMVcp par l'acide lipoïque en utilisant la chimie des

carbodiimides afin de produire des sites d'attachement sur le bord des disques où les nanoparticules auraient ensuite été liées. L'incorporation d'acide 5-azidopentanoïque à la terminaison aminée afin de pouvoir exploiter la chimie « click » de cycloaddition alcyne-azoture plus versatile est aussi abordée. Sur les deux plans, les efforts ont eu peu de succès à cause de ce qui est constaté comme étant une contrainte stérique sur la terminaison aminée qui lui empêche de réagir.

Le chapitre 5 aborde l'attachement de nanoparticules d'or au TMVcp qui a été modifié avec l'acide lipoïque. En dépit d'une modification partiale de la protéine, les anneaux peuvent être obtenus le long du périmètre des disques résultant de la tendance des nanoparticules fonctionnalisées au BSPP de s'associer en chaines linéaires en présence d'une force ionique appropriée. Ces anneaux possèdent aussi des propriétés optiques intéressantes, qui ont été observées par la microscopie en champ sombre, ce qui pointe vers la possibilité que de telles structures pourraient agir comme métamatériaux en solution.

Le TMVcp modifié par l'acide 5-azidopentanoïque est utilisé comme substrat pour la chimie « click » au chapitre 6 afin d'y lier des polymères et de modifier les propriétés d'auto-assemblage du TMVcp. Les tentatives d'y attacher des segments de nucléotides pour ensuite les assembler à des nanoparticules d'or conjuguées aux nucléotides complémentaires sont aussi examinées. Ces deux projets sont retardés en raison du faible rendement de TMVcp modifié, qui résulte de l'encombrement de sa terminaison aminée.

# Acknowledgements

My time at McGill has been overwhelmingly positive and has constituted some of the most fundamental formative years of my life. I am truly grateful for the experiences I have been given having spent both my undergraduate and graduate years at this exceptional institution. First and foremost, I would like to thank my supervisor Dr. Amy Blum whose brilliant ideas and patience for my incessant questions resulted in the successful culmination of this work. I am truly grateful, not only for your guidance, but for the infectious passion and excitement with which you approach the scientific endeavor that is a source of constant inspiration. I would, in turn, wish to thank my thesis committee members; Dr. Mark Andrews, Dr. Bruce Lennox and Dr. Theo van de Ven. I am honored to have been able to discuss the progress of my work and be privy to your invaluable advice.

To my colleagues and friends, Katalin Korpany, Julia Del Re, Josue Lucate and Serene Bayram, it has been an absolute pleasure working both with and alongside you throughout the years. Joel Poisson, I consider you an honorary Blum group member and thank you for all your help with the synthetic aspects of my project.

This work has truly been a collaborative effort and I would like to thank the following people and groups for their invaluable assistance and input; Dr. Alex Wahba who designed and carried out the experiments that allowed the characterization of our TMV coat protein conjugates. Dr. Matt Francis and the Francis group who provided us with the plasmid necessary to express TMV coat protein as well as the protocol for its expression (as well as answers to all our questions when we failed to apply it successfully). Dr. Guruswamy Kumaraswamy and Dr. Sayam Sen Gupta for a truly unforgettable experience in Pune, India and their expansive expertise and collaboration in the attachment of synthetic polymers to our virus coat protein. Dr. Jennifer Chen who provided us with the dark-field scattering data on our structures and thus an unmatched view into their spectroscopic properties. Dr. Peter Norlander and the Norlander group for their insight into the complex theoretical aspects of this work (filling in the ‘why’ after we obtained the ‘what’). Dr. Carissa Soto for her generous help with biochemical techniques. Dr. David Liu for his training, patience and time with the TEM techniques used extensively in

this work. Dr. Mohini Ramkaran for her expertise in surface probe microscopy and our entertaining conversations.

I would also like to thank the Chemistry department administrative staff with special mention to Karen Turner and Colleen McNamee who always have an answer to my administrative questions and Chantal Marotte for her herculean ability to make sure every graduate student is on track and still manage to find the time to send you an e-mail on your birthday.

Finally, I would like to thank my family for their love and support and instilling the love of science in me since I was a child. I would never have had the opportunity to be part of McGill, let alone accomplish what I have, without you.

# List of abbreviations

| | |
|---|---|
| 5-APA | 5-azidopentanoic acid |
| APTMS | (3-aminopropyl)trimethoxysilane |
| Asn | Aspargine |
| Asp | Aspartic acid |
| BMV | Brome Mosaic virus |
| BSPP | Bis(p-sulfonatophenyl)phenylphosphine |
| BSPP-AuNP | BSPP stabilized gold nanoparticle |
| CCMV | Cowpea Chlorotic Mottle virus |
| CuAAC | Copper catalyzed azide-alkyne cycloaddition |
| DCC | Dicyclohexylcarbodiimide |
| DMSO | Dimethylsulfoxide |
| DNA | Deoxyribonucleic acid |
| DTT | Dithiothrietol |
| EBL | Electron beam lithography |
| EDC | 1-ethyl-3-(3-dimethylaminopropyl)carbodiimide hydrochloride |
| EMT | Effective medium theory |
| FIB | Focused-ion beam milling |
| Gln | Glutamine |
| Glu | Glutamic acid |
| HPLC | High-pressure liquid chromatography |
| IPTG | Isopropyl-β-D-thio-galactoside |
| ITO | Indium tin oxide |
| LC-ESI MS | Liquid chromatogram electrospray ionization mass spectroscopy |
| Lys | Lysine |
| MO | Molecular orbital |
| NHS | N-hydroxysuccinimide |
| NIL | Nano-imprint lithography |
| NIM | Negative index material |
| PEO | Polyethylene oxide |
| PLYS | Polylysine |
| RCNMV | Red Clover Necrotic Mosaic virus |
| RNA | Ribonucleic acid |
| S123C-TMVcp | S123C mutant of Tobacco Mosaic virus coat protein |
| SEM | Scanning electron microscopy |
| SPM | Scanning probe microscopy |
| Sulfo-NHS | N-hydroxysulfosuccinimide |
| TEA | Triethanolamine |
| TEM | Transmission electron microscopy |
| THF | Tetrahydrofuran |
| THPTA | Tris(3-hydroxypropyltriazolylmethyl)amine |
| TMV | Tobacco Mosaic virus |
| TMVcp | Tobacco Mosaic virus coat protein |
| Tyr | Tyrosine |
| VLP | Virus-like particle |
| wt-TMVcp | Wild-type Tobacco Mosaic virus |
| αLA | α-lipoic acid |

# List of figures


1.1 Number of articles or reviews published per year with “plasmon” or “plasmonic” in title, abstract or keywaords. Data provided by SCOPUS.

1.2 Graphical representation of nanoparticle in spherical co-ordinates with incident electric field.

1.3 Plot of real and imaginary components of dielectric constant for the free electron gas (solid line) and the literature values for gold (dotted line)

1.4 Cartoon depicting dipoles in nanoparticles excited by transverse (above) and longitudinal (below) polarizations.

1.5 (Left) PSTM Image of well-spaced nanoparticles, scattering and interference effects are clearly visible. (Right) PSTM image of 1D closely-spaced nanoparticle chain. Electromagnetic fields are localized to the gaps and scattering is significantly reduced

1.6 Plasmon hybridization model showing hybridization between modes of two nanoparticles (orange) and higher-order mode mixing as inter-particle gap becomes very small (green).

1.7 Illustration of negative refraction across a boundary (left) and the inversion of the behavior of convex and concave lenses (right).

1.8 (a) Square array of metal cylinders. (b) Split-ring modification to cylinders.

1.9 (a) Split-Ring Resonator geometry. (b) Square array of Split-Ring Resonators.

1.10 Circular array of nano-spheres in the x-y plane excited by (a) a time varying magnetic field directed along z or (b) a time varying electric field directed along y. The vectors on each particle indicate the induced dipole moments in each case.

2.1 Generalized process flow for photolithography.

2.2 TEM image of lines of gold nanoparticles on carbon using a friction transferred poly(tetrafluoroethylene) template.

2.3 (a) Diagram of gold nanoparticle assembly onto columnar DNA scaffolding using complimentary ‘staple’ strands. (b) TEM image of chirally arranged nanoparticles based on scheme in (a). (c) Chirally arranged gold nanoparticles display circular dichroism.

2.4 (A) CCMV structural transitions upon change in pH and ionic strength. (B) Bacteriophage P22 structural transitions upon change in temperature.

2.5 Cartoon depiction of TMV coat protein (blue) protecting RNA (red). © 2014 David Goodsell & RCSB Protein

2.6 Pseudo-phase diagram of TMV coat protein assembly states with TEM images superimposed. Lines denote when each species becomes dominant in number. All three states exist in dynamic equilibrium

2.7 Possible packing arrangement of rings of TMV protein subunits. (A) Bipolar four-layer aggregate found in disk crystals. (B) Polar packing of subunits forming stacked disk observed in electron micrographs.

2.8 Top (A) and bottom (B) surface of TMV coat protein subunit colored from hydrophilic (blue), neutral (white) to hydrophobic (red) by the Kyte and Doolittle hydrophobicity scale86. Bottom surface displays more hydrophobic character and drives the formation of a two-layer disk by hydrophobic attraction. Similarly, hydrophobic groups on the side of the protein drive the assembly of the disk itself.

2.9 (A) Schematic drawing of a disk (left) and helix (right). Disk has larger area of contact for hydrophobic interaction but hydrogen bonding results in a twist (as represented in (B)) and helix formation.

3.1 Schematic of assembly of gold nanoparticles on S123C mutation of TMV 20S disk. Green colored residues are amines while blue colored residues are carboxylic acids. The red colored residues indicate the S123C cysteine mutation.
3.2 Molecular diagram of Bis(p-sulfonatophenyl)phenylphosphine
3.3 Particle analysis of BSPP-functionalized gold nanoparticles.
3.4 TEM images showing the contents of the assembly solution after incubating for five days. Red arrows indicate gold nanorings.
3.5 Summary of assembled nanoparticle rings along with the ratio of rings containing a central nanoparticle at each pH condition.
3.6 TEM images taken early in assembly period showing binding to (a) upper face edge of disk, (b) edge of inner pore and (c) on the pore itself. Schematic above illustrates the functionalities below each nanoparticle. Arginines are colored green, carboxylic acid residues in blue and the S123C cysteine mutation in red.
3.7 Increase in absorption at 600 nm. Signal is subtracted by a concentration matched nanoparticle control containing no TMV coat protein.
3.8 Spectra of assembly solutions at pH 6.0 (yellow), pH 6.5 (red), pH 7.0 (blue) and pH 7.5 (green), corrected by a concentration matched nanoparticle control containing no TMV coat protein.
3.9 Fluorescence spectra of assembly solutions excited at 280 nm before (red) and after (blue) the five day incubation period.
3.10 (Left) Photo taken of assembly solutions separated in agarose gel. (Middle) Image of agarose gel converted into greyscale. (Right) Gel band intensities are plotted and nanoparticle incorporation rate is determined by peak integration. Peaks are first fit to Gaussian curves.
3.11 Illustration of how full (F), partial (N-1) and incomplete (I) rings are identified and sorted.
4.1 Illustration of TMVcp subunit with primary amines (Lys53, Lys68 and N-terminus) shown in green.
4.2 Reactions of EDC with carboxylic acids. The O-acylisourea intermediate may react with a primary amine to form an amide linkage or react with another carboxylic acid to form an anhydride which similarly reacts with amines to form amides. An undesired rearrangement of O-acylisourea to N-acylurea is an undesired side reaction which negatively impacts yield.
4.3 Reaction of O-acylisourea with N-hydroxysuccinimide and its derivatives to form an 'activated' carboxylic acid NHS-ester. This long lived species can react with amines to form amides.
4.4 Reaction schemes illustrating activation of α-lipoic acid by either two-step conjugation with EDC and Sulfo-NHS in pH buffered aqueous solution or NHS-ester isolation by DCC and NHS in organic solvents.
4.5 HPLC trace (above) and mass spectrometry (below) of failed attempt at two-step EDC/sulfo-NHS conjugation of α-lipoic acid in phosphate buffer at pH 7.0 set at an ionic strength of 0.1 M. TMVcp occasionally appears as a dimer (34984.2132 g/mol). Ester:TMVcp ratio was 100:1.
4.6 ESI-LCMS data of the conjugation of TMVcp with N-lipoyloxy succinimide at pH 6.5 (a), pH 7.0 (c) and pH 8.0 (c). All reactions are in phosphate buffer set at an ionic strength of 0.1 M. Ester:TMVcp ratio was 300:1
4.7 ESI-LCMS data of the conjugation of TMVcp with N-lipoyloxy succinimide in carbonate buffer at pH 8.3 at (a) 50 mM ionic strength and (b) 0.4 M ionic strength. Ester:TMVcp ratio is 50:1.
4.8 Reaction scheme illustrating activation of 5-azidopentanoic acid by two-step conjugation with EDC and Sulfo-NHS in pH buffered aqueous solution.

4.9 ESI-LCMS data of the two-step EDC/sulfo-NHS conjugation of wild-type TMVcp with 5-azidopentanoic acid. Reaction is buffered with phosphate at pH 7.0 at an ionic strength of 0.1 M.
4.10 Conformation of TMV coat protein in a 20S disk (left) and lock-washer or helical rod (right). The red coloring shows the unstructured portion of the N-terminus. The green coloring shows the beta sheet formation responsible for retracting the N-terminus behind the unstructured C-terminus. The blue color illustrates the unstructured portion of the C-terminus which obscures the N-terminus in the 20S disk.
5.1 Schematic of the predicted effect of complete and partial conjugation on ring assembly.
5.2 Surveys of unpurified ring solutions (left) and cropped images of individual conjugated TMVcp templated rings.
5.3 Examples of rings with top-face nanoparticle clusters.
5.4 Surveys (left) and cropped images (right) of templated rings after purification by dialysis and spin filtration revealing incomplete nature of conjugation.
5.5 Change in UV-Vis spectrum over time as rings assemble on α-lipoic acid conjugated TMVcp. Solutions are blanked against matching concentration nanoparticle control solutions.
5.6 Dark-field imaging and spectra of diffraction limited spots located on a APTMS-functionalized glass substrate plated with an unpurified ring solution assembled at pH 7.0 (left) and pH 7.5 (right).
6.1 Mechanism of copper catalyzed azide-alkyne cycloaddition with possible intermediates.
6.2 UV-Vis Absorption spectra of azide-TMVcp conjugated before (black) and after (orange) click reaction with alkyne-derivatized fluorescein.
6.3 Schematic of ABAB assembly using TMVcp 20S functionalized with either PEO or PLYS.
6.4 TEM images of TMVcp after CuAAC reaction, purification by spin filtration and 24 hour dialysis.
6.5 Circular dichroism of TMVcp conjugated to 5-APA (black), after click reaction with polylysine (orange) and with polyethylene oxide (blue).
6.6 Control samples revealing the unexpected effects of sodium ascorbate and copper sulfate in the absence of reaction.
6.7 (a) Schematic for attachment of either the linear, flexible ALK3 oligonucleotide sequence or the 3D, rigid, ALK2 ‘rung’. (b) Schematic of subsequent attachment of DNA-nanoparticle conjugates possessing complimentary DNA sequence.
6.8 TEM images of possible assemblies utilizing ALK3 linear DNA conjugated to S123C TMVcp and mixed with nanoparticles conjugated to complimentary DNA strands.

# Chapter 1
# *An overview of plasmonics and metamaterials*

The first section of this chapter begins with an introduction to Maxwell's equations and the dielectric function of a free electron gas. The plasmonic modes of a sub-wavelength spherical nanoparticle are derived and considerations for real metals are discussed. This section concludes with a description of contemporary models for plasmonic coupling.

In the second section, the subject of negative index metamaterials is introduced and the generation of an artificial magnetic response is discussed. The application of plasmonically coupled metal structures to create negative refractive index materials is described in the context of gold nanoparticle rings.

## 1.1 Plasmonics

At its core, plasmonics is the study of electromagnetic wave confinement at interfaces through the excitement of unbound charges in metals and doped semiconductors. In essence, certain frequencies of incident electromagnetic waves can couple to free electrons in the conduction band of a material and trigger collective oscillations of the electron 'plasma', thus localizing the energy of the electromagnetic wave to the surface of the material.

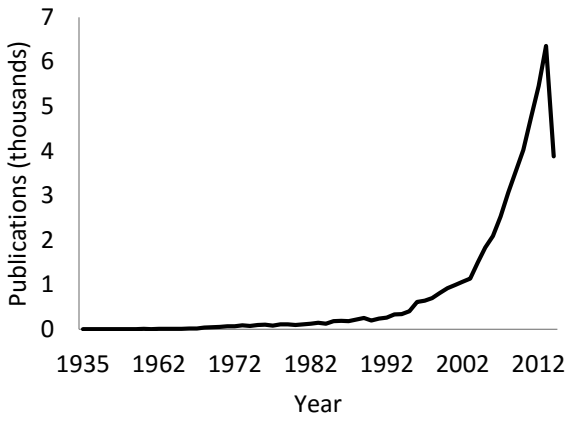


**Figure 1.1|** Number of articles or reviews published per year with "plasmon" or "plasmonic" in title, abstract or keywaords. Data provided by SCOPUS.

While academic interest in the field of plasmonics has increased exponentially only in the past decade or so (*Figure 1.1)* , its study can be traced as far back as 1899 with Arnold Sommerfield's study of the propagation of electromagnetic waves in the THz frequency along a single metal wire[1]. In 1907, Johnathan Zenneck produced a wave solution that was confined to the surface of a metallic interface[2] and exponentially attenuated in the direction of propagation and normal to it. It was not until 1968[3] that the term "localized surface plasmon" was coined to describe this phenomenon along with various anomalous attenuation affects at metallic diffraction gratings[4].

Nanoscale materials can also support plasmons if their electronic density of states is large. Unlike surface plasmons on bulk metals, plasmons excited in sub-wavelength particles oscillate throughout the volume of the particle and are termed local plasmon polaritons. These excitations were mathematically formulated much earlier than localized surface plasmons - in the context of Mie scattering by gold colloids in 1908.

The utility of plasmons was initially demonstrated when it was shown that the signal strength of Raman spectroscopy could be drastically improved when the analyte was in proximity to plasmonically active metals such as silver[5]. The concentrated electromagnetic energy in the vicinity of the metal enhances both the absorption and scattering of waves interacting with the

analyte, greatly improving the signal-to-noise ratio. It was not until recently, however, that the field truly gained traction when it was found that plasmonic metal nanowires could act as optical waveguides at scales that were inaccessible by traditional dielectrics[6], and that metallic films with sub-wavelength cylindrical cavities displayed extraordinary transmission efficiency[7]. Such findings suggested that plasmonics may provide a means to utilize the extraordinary properties of the photon at a scale that the fundamental diffraction limit implied one could not.

Despite the fact that plasmon driven phenomena occur at nanometer length scales, one does not have to resort to quantum electrodynamics to understand them. Indeed, most analytical models of such systems are derived from applications of Maxwell's Equations.

### 1.1.1 Maxwell's equations

The reason one can remain in the comfortable domain of classical physics in the study of plasmonics is due to the fact that plasmons are the oscillations of a high density of free electrons and their electronic energy levels are virtually continuous relative to thermal excitations ($K_BT$) at room temperature. The following analyses will be confined to a description of metals, however, plasmons can also be excited in semi-conductors and insulators under certain conditions[8].

The foundations of light-matter interaction are Maxwell's macroscopic equations:

$$\nabla \cdot \mathbf{D} = \rho_{free} \tag{1.1}$$

$$\nabla \cdot \boldsymbol{B} = 0 \tag{1.2}$$

$$\nabla \times \boldsymbol{E} = -\frac{\delta \boldsymbol{B}}{\delta t} \tag{1.3}$$

$$\nabla \times \boldsymbol{H} = \boldsymbol{J_{free}} + \frac{\delta \boldsymbol{D}}{\delta t} \tag{1.4}$$

where $\boldsymbol{E}$ and $\boldsymbol{B}$ are the electric and magnetic fields impinging on a material, $\boldsymbol{D}$ and $\boldsymbol{H}$ are the electric displacement and magnetizing field that constitute the material's response, and finally $\rho_{free}$ and $\boldsymbol{J_{free}}$ are the charge and current densities of free charges respectively. Each charged particle in a material behaves as a field source, and in virtually all real systems, the number of these charges is too large to consider a microscopic analysis of each. Furthermore, since the

driving field wavelengths are often much larger than the microscopic variations within a material, it is often the average field that provides a more meaningful picture of a material's behaviour. For these reasons, all four fields are *macroscopic fields* and represent average quantities.

The electric displacement and magnetizing fields are the result of interactions of the driving field with the polarization, $\boldsymbol{P}$, and magnetization, $\boldsymbol{M}$, fields within a material.

$$\mathbf{D}(\mathbf{r},\mathrm{t}) = \epsilon_0 \boldsymbol{E}(\mathbf{r},\mathrm{t}) + \boldsymbol{P}(\mathbf{r},\mathrm{t}) \tag{1.5}$$

$$\mathbf{H}(\mathbf{r},\mathrm{t}) = \frac{1}{\mu_0}\boldsymbol{B}(\mathbf{r},\mathrm{t}) - \boldsymbol{M}(\mathbf{r},\mathrm{t}), \tag{1.6}$$

where $\boldsymbol{r}$ is the position vector, $t$ is time, $\epsilon_0$ is the vacuum permittivity and $\mu_0$ is the vacuum permeability. Equations relating $\boldsymbol{E}$, $\boldsymbol{B}$, $\boldsymbol{H}$ and $\boldsymbol{D}$ are called constitutive relations. These relationships can vary widely in complexity and often cannot be solved exactly without applying approximations. If one assumes a linear medium with a response that can be averaged over a distance much larger than the microscopic variations of the material, then one obtains the following constitutive relations:

$$\mathbf{D}(\mathbf{r},\mathrm{t}) = \epsilon_0 \iint \epsilon(\boldsymbol{r}-\boldsymbol{r}', t-t')\boldsymbol{E}(\mathbf{r}',\mathrm{t}')\mathrm{d}t'\mathrm{d}\mathbf{r}' \tag{1.7}$$

$$\mathbf{H}(\mathbf{r},\mathrm{t}) = \frac{1}{\mu_0}\iint \frac{1}{\mu(\boldsymbol{r}-\boldsymbol{r}', t-t')}\boldsymbol{B}(\mathbf{r}',\mathrm{t}')\mathrm{d}t'\mathrm{d}\mathbf{r}' \tag{1.8}$$

where $\epsilon$ and $\mu$ are tensors called the electric permittivity (or dielectric constant) and magnetic permeability respectively. These two quantities completely describe a material's electromagnetic response. For materials displaying dispersion (ϵ or μ are not constants) it is often easier to describe the material response in the frequency domain. This is done using the *Fourier transform,* $f(\boldsymbol{k},\omega) = \iint f(\boldsymbol{r},t)e^{i(\boldsymbol{k}\cdot\boldsymbol{r}-\omega t)}d\boldsymbol{r}dt$, so that the four fields are represented in terms of wave vector, $\boldsymbol{k}$, and angular frequency $\omega$ rather than position and time. The result is a simplified set of constitutive relations for linear media:

$$\mathbf{D}(\mathbf{k},\omega) = \epsilon_0\epsilon(\boldsymbol{k},\omega)\boldsymbol{E}(\mathbf{k},\omega) \tag{1.9}$$

$$\mathbf{H}(\mathbf{k},\omega) = \frac{1}{\mu_0\mu(\boldsymbol{k},\omega)}\boldsymbol{B}(\mathbf{k},\omega) \tag{1.10}$$

The material parameters $\mu$ and $\epsilon$ are complex functions of frequency of the form, $y(\omega) = y_1(\omega) + iy_2(\omega)$. Their collective effect on the transmission or absorption of light is sometimes expressed as a complex *index of refraction*, ñ, which is related to the two parameters by:

$$\tilde{n} = n(\omega) + ik(\omega) = \sqrt{\epsilon(\omega)\mu(\omega)} \tag{1.11}$$

The imaginary component of the refractive index is related to the absorption of electromagnetic energy and thus $k$ is called the *extinction coefficient*. It is related to the Beer's Law absorption coefficient, $\alpha$, by:

$$I(x) = I_0 e^{-\alpha x} \tag{1.12}$$

$$\alpha = \frac{2k(\omega)\omega}{c} \tag{1.13}$$

where $c$ is the speed of light in vacuum and $I(x)/I_0$ is attenuation ratio of the intensity of light passing through a material. The imaginary components of both the permittivity and the permeability are also closely related to dissipation of electromagnetic radiation in a material.

### 1.1.2 The dielectric function of the free electron gas

As the frequency of interest increases into the infrared, the permeability of almost all materials approaches 1 and, therefore, they do not interact significantly with the magnetic component of light. In this case, one can completely describe the optical properties of a material by its dielectric (permittivity) function alone and ignore the effect of the magnetic field in an incident electromagnetic wave.

Metals are characterized by their large number of unbound electrons that move freely in the conduction band. In 1900, Paul Drude[9] proposed that one could model the transport properties of materials with a high density of free charges as a negatively charged gas, or *plasma*, that moves against a fixed background of positive ion cores. This assumption is reasonable due to the enormous difference in mass between an electron and an atomic nucleus. The plasma will oscillate in response to a driving electromagnetic field due to the interaction of electric force exerted on the plasma by the incident electric field, and the restoring force exerted on the plasma by the positive ion background. The oscillation of the plasma will be damped by inter-electron collisions that occur with a *characteristic collision frequency,* $\gamma = 1/\tau$*,* where $\tau$ is called

the *relaxation time* of the free electron gas. The *Drude model*[10,11] assumes all collisions are elastic and ignores electron-electron interactions as well as lattice potentials. An *effective optical mass* of the electron is introduced to account for some of the electronic properties of specific metals. The equation of motion for an electron in such plasma subjected to an electric field in one dimension is:

$$\boldsymbol{F_{total}} = -(\boldsymbol{F_{electric}} + \boldsymbol{F_{restore}}) \tag{1.14}$$

$$\mathrm{m_{eff}}\frac{\mathrm{d}^2\mathbf{x}(\mathrm{t})}{\mathrm{dt}^2} = -\mathrm{m_{eff}}\gamma\frac{\mathrm{d}\mathbf{x}(\mathrm{t})}{\mathrm{dt}} - \mathrm{e}\mathbf{E}(\mathrm{t}) \tag{1.15}$$

where *e* is the charge of an electron. The negative sign is best understood in the context of a spring, where the restoring force is always directed opposite to the driving force.

If one assumes a harmonic time dependence for the incident wave such that $\boldsymbol{E}(t) = \boldsymbol{E_0}e^{-i\omega t}$, then a solution to the linear differential equation (1.15) is $\boldsymbol{x}(t) = \boldsymbol{x_0}e^{-i\omega t}$. By substituting this back into (1.15) one obtains:

$$\boldsymbol{x_0} = \frac{e\boldsymbol{E_0}}{m_{eff}(\omega^2 + i\gamma\omega)}$$

And so,

$$\mathbf{x}(\mathrm{t}) = \frac{e}{m_{eff}(\omega^2 + i\gamma\omega)}\boldsymbol{E}(t) \tag{1.16}$$

These displaced electrons will create a macroscopic polarization field which will be the average electric dipole moment $\boldsymbol{p}$ produced per unit volume, $V$. For a system of electrons each producing the same dipole moment:

$$\boldsymbol{P} = \frac{\langle \boldsymbol{p} \rangle}{V} = -\frac{\langle e\boldsymbol{x}(t) \rangle}{V} = -ne\boldsymbol{x}(t) = -\frac{ne^2}{m_{eff}(\omega^2 + i\gamma\omega)}\boldsymbol{E}(t), \tag{1.17}$$

where $n$ is the number density of charges.

If one now substitutes this definition of $\boldsymbol{P}$ into equation (1.5), and recalls equation (1.9), one obtains the dielectric function for the free electron gas:

$$\boldsymbol{D} = \epsilon_0\boldsymbol{E} + \boldsymbol{P} = \epsilon_0\boldsymbol{E}\left(1 - \frac{ne^2}{\epsilon_0 m_{eff}(\omega^2 + i\gamma\omega)}\right) = \epsilon_0\epsilon(\omega)\boldsymbol{E}$$

So finally,

$$\epsilon(\omega) = 1 - \frac{ne^2}{\epsilon_0 m_{eff}(\omega^2 + i\gamma\omega)} = 1 - \frac{\omega_p^2}{\omega^2 + i\gamma\omega} \tag{1.18}$$

$\omega_p = \sqrt{\frac{ne^2}{\epsilon_0 m_{eff}}}$ is called the *plasma frequency.* Below this frequency, the dielectric constant is negative, and electromagnetic radiation cannot penetrate the material very far - photons are mostly reflected. Above the plasma frequency, the metal behaves as a dielectric and is transparent to incident radiation.

### 1.1.3 Plasmon modes of a sub-wavelength spherical nanoparticle

The classical Drude model for permittivity can be applied to metallic nanostructures that are coupled to an incident electromagnetic field[12]. A model can now be formulated to describe the plasmon excitations of an individual, sub-wavelength, metal nanoparticle. It will later be shown that the coupling of spherical nanoparticles into oligomers can be modelled as a linear combination of the plasmon modes of individual particles.

The local surface plasmons of an individual particle arise naturally when one considers the problem of the scattering of incident electromagnetic radiation by conduction band electrons of a nanoparticle. This involves the calculation of the electric field, $\boldsymbol{E}$, in the vicinity of the particle. As discussed in the previous section, the driving field is assumed to be harmonically oscillating. The curved surface of the nanoparticle means that the electrons at the surface of the particle can be excited from any angle. One can simplify this problem greatly if one considers that the size of the particle is significantly smaller than the wavelength of the incident light, which implies that the phase of a harmonically oscillating electromagnetic field is virtually constant over the particle's volume (*phase-retardation* is negligible). This *quasi-static approximation* allows us to utilize an electric field that is constant over time in order to solve its distribution over space. One can then add a harmonically oscillating term afterwards such that $\boldsymbol{E}(\boldsymbol{r}, t) = \boldsymbol{E}(\boldsymbol{r})e^{-i\omega t}$.

In order to determine $\boldsymbol{E}(r)$ one can begin with Coulomb's Law for a surface charge distribution $\rho(\boldsymbol{r})$ and a test charge $q$[13]:

$$\frac{\boldsymbol{F}(\boldsymbol{r})}{q} = \boldsymbol{E}(\boldsymbol{r}) = \frac{1}{4\pi\epsilon_0}\int \frac{\rho(\boldsymbol{r})}{\boldsymbol{r}^2} d\boldsymbol{r} = -\frac{1}{4\pi\epsilon_0}\boldsymbol{\nabla}\int \frac{\rho(\boldsymbol{r})}{\boldsymbol{r}} d\boldsymbol{r}$$

And so, $$\boldsymbol{E}(\boldsymbol{r}) = -\boldsymbol{\nabla}\Phi(\mathbf{r}) \tag{1.19}$$

$\Phi(\boldsymbol{r})$ is called the *scalar potential* and it is often easier to deal with this singular function of position rather than the vector field $\boldsymbol{E}$. One can substitute this expression into Gauss' law in differential form to obtain:

$$-\boldsymbol{\nabla}\cdot\boldsymbol{E} = -\frac{\rho}{\epsilon_0} = \boldsymbol{\nabla^2}\Phi(\mathbf{r}) \tag{1.20}$$

This is called the *Poisson Equation*. If the region of interest lies outside the vicinity of the charges (such as in our case outside of the nanoparticle), $\rho = 0$, and one obtains the *Laplace Equation:*

$$\boldsymbol{\nabla^2}\Phi(\mathbf{r}) = 0 \tag{1.21}$$

In the quasi-static approach, the Laplace equation will be solved for an isotropic sphere with dielectric constant $\epsilon$ and radius a embedded in an isotropic, transparent medium with dielectric constant $\epsilon_m$. Once the scalar potential, $\Phi\ (\boldsymbol{r})$, is obtained, the electric field will be determined through equation (1.19). The spherical symmetry of the particle allows the use of a spherical coordinate system which will facilitate the analysis *(Figure 1.2)*.

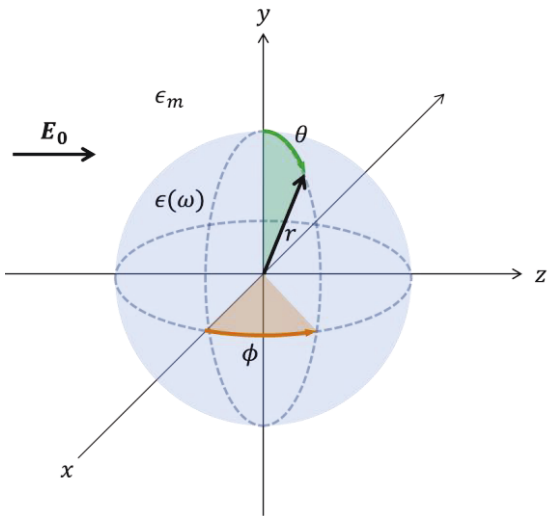


**Figure 1.2|** Graphical representation of nanoparticle in spherical co-ordinates with incident electric field.

The Laplace equation expressed in spherical co-ordinates takes the form[13]:

$$\nabla^2\Phi(\mathrm{r},\theta,\phi) = \frac{1}{\mathrm{r}}\frac{\delta^2(r\Phi)}{\delta r^2} + \frac{1}{r^2\sin\theta}\frac{\delta}{\delta\theta}\left(\sin\theta\frac{\delta\Phi}{\delta\theta}\right) + \frac{1}{r^2\sin^2\theta}\frac{\delta^2\Phi}{\delta\phi^2} = 0 \tag{1.22}$$

If one assumes that the three positional variables are separable, then the solution can be made into a product of three single-variable expressions:

$$\Phi(\mathrm{r},\theta,\phi) = \frac{\mathrm{U(r)}}{\mathrm{r}}\mathrm{P}(\theta)\mathrm{Q}(\phi) \tag{1.23}$$

Substituting this into (1.22):

$$\mathrm{P}(\theta)\mathrm{Q}(\phi)\frac{\mathrm{d}^2U(r)}{\mathrm{dr}^2} + \frac{\mathrm{U(r)Q}(\phi)}{\mathrm{r}^2\sin\theta}\frac{\mathrm{d}}{\mathrm{d}\theta}\left(\sin\theta\frac{\mathrm{dP}(\theta)}{\mathrm{d}\theta}\right) + \frac{\mathrm{U(r)P}(\theta)}{\mathrm{r}^2\sin^2\theta}\frac{\mathrm{d}^2\mathrm{Q}(\phi)}{\mathrm{d}\phi^2} = 0 \tag{1.24}$$

The dependence on the azimuth,ϕ is isolated by multiplying by, $\frac{r^2\sin^2\theta}{U(r)P(\theta)Q(\phi)}$ , on both sides:

$$r^2\,sin^2\,\theta\left[\frac{1}{U(r)}\frac{d^2U(r)}{dr^2} + \frac{1}{P(\theta)r^2\sin\theta}\frac{d}{d\theta}\left(\sin\theta\frac{dP(\theta)}{d\theta}\right)\right] + \frac{1}{Q(\phi)}\frac{\mathrm{d}^2\mathrm{Q}(\phi)}{\mathrm{d}\phi^2} = 0 \tag{1.25}$$

The term at the right must be equal to a constant since no other part of the equation depends on $\phi$ and the total sum of all terms must equal zero. The term will be set to $-m^2$ (This will not be the last time a seemingly arbitrary expression for a constant is used. Their use comes from the benefit of hindsight as the choice of these constants results in an expression with a known solution).

$$\frac{1}{\mathrm{Q}(\phi)}\frac{d^2Q(\phi)}{d\phi^2} = -m^2 \tag{1.26}$$

This has solutions,

$$Q(\phi) = e^{\pm im\phi} \tag{1.27}$$

$Q(\phi)$ will not be single valued for $\phi = 0$ and $\phi = 2\pi$ (which is the same point in space) unless $m$ is restricted to integer values only[14]. Separating the remaining variables in (1.25):

$$\frac{\mathrm{r}^2\sin^2\theta}{\mathrm{U(r)}}\frac{\mathrm{d}^2U(r)}{\mathrm{dr}^2} + \frac{\sin\theta}{\mathrm{P}(\theta)}\frac{\mathrm{d}}{\mathrm{d}\theta}\left(\sin\theta\frac{\mathrm{dP}(\theta)}{\mathrm{d}\theta}\right) - \mathrm{m}^2 = 0$$

Dividing by $\sin^2\theta$,

$$\left\{\frac{\mathrm{r}^2}{\mathrm{U(r)}}\frac{\mathrm{d}^2U(r)}{\mathrm{dr}^2}\right\}+\left\{\frac{1}{\mathrm{P}(\theta)\sin\theta}\frac{\mathrm{d}}{\mathrm{d}\theta}\left(\sin\theta\frac{\mathrm{dP}(\theta)}{\mathrm{d}\theta}\right)-\frac{\mathrm{m}^2}{\sin^2\theta}\right\}=0 \tag{1.28}$$

The first term in curly brackets is only dependent on the radial variable while the second term in curly brackets depends only on the polar angle. As before these two terms must each be equal to constants which, when added together, cancel out. The radial term will be set to $l(l+1)$ while the polar term is set to $-l(l+1)$. The radial expression shall be solved first:

$$\frac{\mathrm{r}^2}{U(r)}\frac{d^2U(r)}{dr^2}=l(l+1)$$

Rearranging,

$$r^2\frac{d^2U(r)}{dr^2}-l(l+1)U(r)=0 \tag{1.29}$$

This expression has the form of a Euler equation, $ax^2y''+bxy'+cy=0$. Euler equations can be transformed into linear differential equations (the dependency notation of functions will be omitted temporarily for simplicity):

Let $z$ be a variable of $r$ such that,

$$r=e^z \text{ and } \frac{dr}{dz}=e^z$$

By the chain rule,

$$\frac{dU}{dr}=\frac{dU}{dz}\cdot\frac{dz}{dr}=e^{-z}\frac{dU}{dz}$$

And so,

$$\frac{d^2U}{dr^2}=\frac{d}{dr}\left(\frac{dU}{dr}\right)=\frac{d}{dz}\left(\frac{dU}{dr}\right)\frac{dz}{dr}=\frac{d}{dz}\left(e^{-z}\frac{dU}{dz}\right)\frac{dz}{dr}$$

Differentiating the term in brackets using the product rule and substituting $dz/dr$ gives,

$$\frac{d^2U}{dr^2}=\left(-e^{-z}\frac{dU}{dz}+e^{-z}\frac{d^2U}{dz^2}\right)e^{-z}=r^{-2}\left(\frac{d^2U}{dz^2}-\frac{dU}{dz}\right) \tag{1.30}$$

Substituting this back into the radial equation (1.29) results in a second-order, homogeneous differential equation with constant coefficients:

$$\frac{d^2U(z)}{dz^2} - \frac{dU(z)}{dz} - l(l+1)U(z) = 0 \tag{1.31}$$

The characteristic equation, with roots, $\Gamma$, such that, $U(z) = e^{-\Gamma z}$, is:

$$\Gamma^2 - \Gamma - l(l+1) = (\Gamma + l)(\Gamma - l - 1) = 0$$

This gives $\Gamma_1 = l - 1$, and, $\Gamma_2 = -l$, so the solution for $U(z)$ becomes:

$$U(z) = Ae^{(l-1)z} + Be^{-lz}$$

Recalling that $r = e^z$,

$$U(r) = Ar^{l-1} + Br^{-l} \tag{1.32}$$

The coefficients $l$, $A$ and $B$ remain undetermined. In order to find them, boundary conditions will have to be set, but first, the angular equation must be solved:

$$\frac{1}{\sin\theta}\frac{d}{d\theta}\left(\sin\theta\,\frac{dP(\theta)}{d\theta}\right) + \left[l(l+1) - \frac{m^2}{\sin^2\theta}\right]P(\theta) = 0 \tag{1.33}$$

This equation can be expressed in a form that has a well-known solution:

Let $x = \cos\theta$, so $\frac{dx}{d\theta} = -\sin\theta$, and,

$$\frac{dP(\theta)}{d\theta} = \frac{dP(x)}{dx}\cdot\frac{dx}{d\theta} = -\sin\theta\,\frac{dP(x)}{dx}$$

Substituting this into (1.33),

$$-\frac{d}{dx}\left(-\sin^2\theta\,\frac{dP(x)}{dx}\right) + \left[l(l+1) - \frac{m^2}{\sin^2\theta}\right]P(x) = 0$$

Recalling that $x = \cos\theta$ and the trigonometric identity, $\sin^2\theta = 1 - \cos^2\theta$,

$$\frac{d}{dx}\left((1-x^2)\frac{dP(x)}{dx}\right) + \left[l(l+1) - \frac{m^2}{1-x^2}\right]P(x) = 0 \tag{1.34}$$

This is called the *generalized Legendre equation*, named after the French mathematician who studied it and its solutions, the *Legendre Polynomials*, $P_l^m(x)$, or in this case, $P_l^m(\cos\theta)$ so,

$$P(\theta) = P_l^{|m|}(\cos\theta)$$

One of the properties of this set of orthogonal polynomials is that $l$ can only be zero or a positive integer while $m$ is limited to integers between the range $-l$ and $l$. Combining the solutions, the complete solution for the scalar potential is:

$$\Phi(r,\theta,\phi) = e^{im\phi}[A_l r^l + B_l r^{-(l+1)}]P_l^{|m|}(\cos\theta)$$

With $l = 0,1,2,\ldots$ and $m = -l, -l+1, \ldots, -1,0,1, \ldots, l-1, l$.

The azimuthal symmetry of the spherical system means that one only needs to consider $m = 0$ which leaves us with:

$$\Phi(r,\theta) = \left[A_l r^l + B_l r^{-(l+1)}\right]P_l^0(\cos\theta) \tag{1.35}$$

All that remains is to determine the coefficients $A_l$ and $B_l$. In order to do this, some boundary conditions[15] must be applied in the context of a metal spherical nanoparticle. The driving field is incident parallel to the z-axis such that, $\boldsymbol{E} = E_0\hat{\boldsymbol{z}}$.

Condition 1: *The $\boldsymbol{E}$ field inside the sphere, $\boldsymbol{E_{in}}$, will be different from the field outside the sphere, $\boldsymbol{E_{out}}$.* This requires that one formulate two separate equations for the scalar potential:

$$\Phi_{\text{in}}(r,\theta) = \left[A_l r^l + B_l r^{-(l+1)}\right]P_l^0(\cos\theta)$$
$$\Phi_{\text{out}}(r,\theta) = \left[C_l r^l + D_l r^{-(l+1)}\right]P_l^0(\cos\theta)$$

Condition 2: *The field at the center of the sphere should have a finite value ($r \to 0$, $\boldsymbol{E_{in}} \to finite$).*

Due to the $r^{-(l+1)}$ factor, $\Phi_{in}$ will always go to infinity as $r \to 0$, which will result in $\boldsymbol{E_{in}} \to \infty$. In order to satisfy this condition, $B_l$ must be zero for all values of $l$ which gives us:

$$\Phi_{\text{in}}(r,\theta) = A_l r^l P_l^0(\cos\theta)$$

This leaves only three coefficients to determine.

Condition 3: *The electric field outside the sphere becomes indistinguishable from the incident electric field as one moves further away from the sphere along the z-axis. ($r \to \infty$, $\boldsymbol{E_{out}} \to E_0\hat{\boldsymbol{z}}$, $\Phi_{out} = E_0 z = -E_0 r\cos\theta$)*

This condition allows one to find the possible values of $l$. The Legendre polynomials, $P_l(\cos\theta)$, are listed below for the first four values of $l$ at $m = 0$:

$l = 0, m = 0 \qquad P_0^0(\cos\theta) = 1$

$l = 1, m = 0 \qquad P_1^0(\cos\theta) = \cos\theta$

$l = 2, m = 0 \qquad P_2^0(\cos\theta) = \frac{1}{2}(3\cos^2\theta - 1)$

$l = 3, m = 0 \qquad P_3^0(\cos\theta) = \frac{1}{2}(5\cos^3\theta - 3\cos\theta)$

It is clear that only $l = 1$ will satisfy the condition, so for $l \neq 1$, $C_l$ and $D_l$ must equal zero. For the $l = 1$ case:

$$\Phi_{\text{out}}(r,\theta) = C_1 r cos\,\theta + D_1 r^{-2}\cos\theta = -E_0 r\cos\theta$$

As $r \to \infty$, $r^{-2} \to 0$ which implies that $C_1 = -E_0$.

The next two conditions involve the boundary at $r = a$, the radius of the particle. At this interface, both the displacement fields and tangential electric fields inside and outside the sphere must be equal in order to create a continuous system. Using the results from condition 3 one can conclude that since $C_l$ and $D_l$ are equal to zero for all values $l \neq 1$, then $A_l$ must also be equal to zero for $l \neq 1$ in order to satisfy the equality of the two fields at the $r = a$ boundary. So for the remainder of this analysis, one only has to evaluate $\Phi$ at $l = 1$.

Condition 4: *The displacement fields* $\boldsymbol{D_{in}} = \epsilon_0\epsilon\boldsymbol{E_{in}}$ *and* $\boldsymbol{D_{out}} = \epsilon_0\epsilon_m\boldsymbol{E_{out}}$ *must be equal at* $r = a$.

In order to satisfy this condition, the following must be true:

$$\epsilon\frac{\delta\Phi_{\text{in}}(r,\theta)}{\delta r} = \epsilon_m\frac{\delta\Phi_{\text{out}}(r,\theta)}{\delta r} \tag{1.36}$$

Evaluating each differential at $l = 1$ and $r = a$,

$$\frac{\delta\Phi_{\text{in}}(r,\theta)}{\delta r} = \frac{\delta}{\delta r}\,A_1 r cos\,\theta = A_1\cos\theta \tag{1.37}$$

And,

$$\frac{\delta\Phi_{\text{out}}(r,\theta)}{\delta r} = \frac{\delta}{\delta r}\left[C_1 r\cos\theta + \frac{D_1}{r^2}\cos\theta\right] \tag{1.38}$$

$$= C_1\cos\theta - \frac{2D_1}{a^3}\cos\theta$$

Substituting (1.37) and (1.38) into (1.36) and setting $C_1 = -E_0$ gives:

$$\epsilon A_1\cos\theta = -\epsilon_m E_0\cos\theta - \frac{2\epsilon_m D_1}{a^3}$$

$$A_1 = -\frac{E_0\epsilon_m}{\epsilon} - \frac{2\epsilon_m D_1}{\epsilon a^3} \tag{1.39}$$

With two unknowns one requires one more equation to solve for the coefficients, this will be obtained from the final boundary condition.

Condition 5: *The tangential components of the electric fields inside and outside the sphere must be equal at $r = a$.*

For this to be satisfied, the following must be true:

$$\frac{\delta\Phi_{\text{in}}(r,\theta)}{\delta\theta} = \frac{\delta\Phi_{\text{out}}(r,\theta)}{\delta\theta} \tag{1.40}$$

Evaluating each differential at $l = 1$ and $r = a$,

$$\frac{\delta\Phi_{\text{in}}(r,\theta)}{\delta\theta} = -A_1 a\sin\theta$$

$$\frac{\delta\Phi_{\text{out}}(r,\theta)}{\delta\theta} = -C_1 a\sin\theta - \frac{D_1}{a^2}\sin\theta = E_0 a\sin\theta - \frac{D_1}{a^2}\sin\theta$$

Equating the two differentials,

$$-A_1 a\sin\theta = E_0 a\sin\theta - \frac{D_1}{a^2}\sin\theta$$

$$A_1 = -E_0 + \frac{D_1}{a^3} \tag{1.41}$$

With two equations and two unknowns, the coefficients $A_1$ and $D_1$ can be solved and one obtains:

$$A_1 = -\frac{3\epsilon_m}{\epsilon + 2\epsilon_m}E_0$$

$$D_1 = a^3 E_0 \frac{\epsilon - \epsilon_m}{\epsilon + 2\epsilon_m}$$

Finally, the potentials are:

$$\Phi_{in} = -\frac{3\epsilon_m}{\epsilon + 2\epsilon_m} E_0 \, r \cos\theta$$

$$\Phi_{out} = -E_0 r cos\ \theta + \frac{\epsilon - \epsilon_m}{\epsilon + 2\epsilon_m} a^3 E_0 \frac{\cos\theta}{r^2}$$

The second term in $\Phi_{out}$ has the form of the scalar potential of an electric dipole moment. If one defines the dipole moment as, $= 4\pi\epsilon_0\epsilon_m a^3 \frac{\epsilon-\epsilon_m}{\epsilon+2\epsilon_m} \boldsymbol{E_0}$ , then:

$$\Phi_{out} = -E_0 r cos\ \theta + \frac{\boldsymbol{p} \cdot \boldsymbol{r}}{4\pi\epsilon_0\epsilon_m r^3}$$

The applied field induces a dipole moment proportional to $|\boldsymbol{E_0}|$. Often the dipole moment is expressed as:

$$\boldsymbol{p} = \epsilon_0 \epsilon \alpha \boldsymbol{E_0}, \tag{1.42}$$

where $\alpha$ is the polarizability. Therefore,

$$\alpha = 4\pi a^3 \frac{\epsilon - \epsilon_m}{\epsilon + 2\epsilon_m} \tag{1.43}$$

This is the complex polarizability of a sub-wavelength nanoparticle in the quasi-static limit. The polarizability of such a sphere will experience a resonant enhancement when $|\epsilon + 2\epsilon_m| \to 0$ which for a small, or slow-varying imaginary component of $\epsilon$ near the resonance wavelength simplifies to the *Fröhlich resonance condition:*

$$Re(\epsilon) = -2\epsilon_m \tag{1.44}$$

This analysis will be completed by retrieving the electric fields inside and outside the metal sphere:

$$\mathbf{E}_{\boldsymbol{in}} = \frac{3\epsilon_m}{\epsilon + 2\epsilon_m} \boldsymbol{E_0} \tag{1.45}$$

$$\mathbf{E}_{\boldsymbol{out}} = \boldsymbol{E_0} + \frac{3\boldsymbol{n}(\boldsymbol{n}\cdot\boldsymbol{p}) - \boldsymbol{p}}{4\pi\epsilon_0\epsilon_m r^3}, \tag{1.46}$$

where $\boldsymbol{n}$ is the unit vector in the direction of interest. In summary, an electromagnetic field incident on a sub-wavelength metal nanoparticle will couple to the free electron plasma and

generate a dipole moment due to the displacement of the center of mass of the electron cloud against the positive ion background. This moment has a resonant character due to the restoring force asserted by the shape of the particle and one obtains a resonant electric field enhancement inside and outside the nanoparticle at specific wavelengths. The oscillating mode is known as a plasmon mode and can be approximated as dipolar. Most applications of plasmonic metals rely on this enhancement. It can be seen from (1.42) that the electric field enhancement is strongly dependent on the dielectric constant of the surrounding medium. This is the incentive behind plasmon-based sensing devices, since a small change in the dielectric environment surrounding a plasmonically active material will elicit a strong change in the plasmonic response.

Until now the nanoparticle has been analyzed under an electrostatic regime, and the oscillating nature of the incident electromagnetic field has been neglected. The second part of the quasi-static approximation involves adding this time dependent property. If one assumes a plane wave illumination such that the incident field takes the form $\boldsymbol{E}(\boldsymbol{r},t) = \boldsymbol{E_0}e^{-i\omega t}$ then the polarizability becomes time dependent as well $\boldsymbol{p}(t) = \epsilon_0\epsilon\alpha\boldsymbol{E_0}e^{i\omega t}$. The crux of the quasi-static limit in the sub-wavelength particle system is that it enables one to approximate a plasmonic particle as a radiating point dipole. Having added the time dependence, all that remains is to determine the effect of the plasmonic nanoparticle on the incident field itself.

When light impinges on particles within a transparent medium, it loses power to absorption and scattering by the particles. These effects are often measured in terms of a 'cross-section' since light from a single direction observes a 2D projection of the particle. While one can approximate our system as a point dipole as illustrated above to arrive at a result, the problem of scattering and absorption by a small sphere is solved completely without approximations by Mie theory, named after Gustav Mie who worked extensively on understanding the color of gold colloids[16]. By following this model, one obtains the following expressions for the scattering, $C_{sca}$, and absorption, $C_{abs}$, cross-sections of a sphere with the polarizability $\alpha$ that we formulated previously[17]:

$$C_{sca} = \frac{k^4}{6\pi}|\alpha|^2 = \frac{8\pi}{3}k^4a^6\left|\frac{\epsilon - \epsilon_m}{\epsilon + 2\epsilon_m}\right|^2 \quad (1.47)$$

$$C_{abs} = kIm[\alpha] = 4\pi ka^3 Im\left[\frac{\epsilon - \epsilon_m}{\epsilon + 2\epsilon_m}\right] \quad (1.48)$$

There are two important observations to be made from these expressions. The first is that both absorption and scattering are resonantly enhanced at the plasmon resonance. The second is that absorption dominates the extinction at small particle sizes, while scattering becomes dominant at larger values of $a$. This result is important because it highlights the need to tailor the size of a nanoparticle to the application for which it shall be used. In a plasmonic metal nanoparticle, the mechanism of absorption is the formation of electron-hole pairs as electrons undergo intra-band transitions within the conduction band or inter-band transitions (such as from the d-band to the sp-band in noble metals). Absorption is not the only efficiency loss mechanism for plasmon enhancement. Despite the fact that scattering is enhanced as particle size increases, there is an upper limit imposed by radiation damping, a process whereby plasmons decay into photons.

### 1.1.4 Considerations for real metals

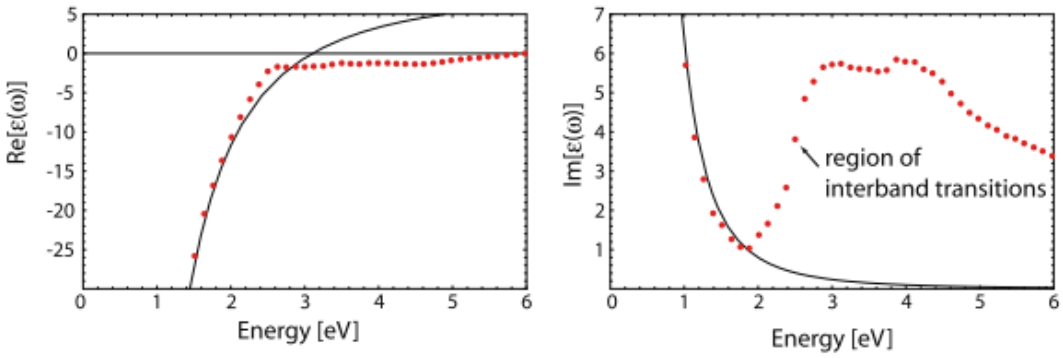


**Figure 1.3|** Plot of real and imaginary components of dielectric constant for the free electron gas (solid line) and the literature values for gold (dotted line)[10]. 

While Mie theory provides a complete and exact analysis of the interaction of light with small spheres, the assumptions made in formulating a dielectric constant for a plasmonic nanoparticle can lead to significant deviations from real systems. For example, in many cases the dielectric constant for the free electron gas (1.18) must be modified such that:

$$\epsilon(\omega) = \epsilon_\infty - \frac{\omega_p^2}{\omega^2 + i\gamma\omega} \tag{1.49}$$

The added $\epsilon_\infty$ term accounts for residual polarization due to the nature of the orbitals from which conduction electrons are being excited. Despite this correction, electronic inter-band transitions can cause significant deviations from the Drude model *(Figure 1.3)* because they represent a competing pathway which results in a damping of the plasmon excitation. This is a problem that arises in noble metals such as gold and silver which have inter-band transitions in the optical frequency spectrum, and it can be overcome by adding an additional term in (1.15):

$$\mathrm{m_{eff}}\frac{\mathrm{d}^2\mathbf{x}(\mathrm{t})}{\mathrm{dt}^2} = -\mathrm{m_{eff}}\gamma\frac{\mathrm{d}\mathbf{x}(\mathrm{t})}{\mathrm{dt}} - \mathrm{m}\omega_0^2\mathbf{x}(\mathrm{t}) - \mathrm{e}\mathbf{E}(\mathrm{t}) \tag{1.50}$$

This accounts for the inter-band transition as a bound electron with a resonance frequency, $\omega_0$.

Another issue arises when one observes that Mie theory and the Drude model do not account for the readily observable size dependence of plasmon resonance frequency with particle size for particles below 30 nm[18]. The reason for this inaccuracy is a consequence of the classical foundation from which these models arise. As the size of a particle decreases below the mean-free path of an electron, electron scattering events at the surface of the particle will elicit size dependence in the dielectric constant.

### 1.1.5 Plasmon coupling

One of the most important properties of plasmons in their application to metamaterials, and nanotechnology in general, is the propensity for adjacent plasmon modes to couple, or hybridize, altering the plasmon resonances of the original particles, and creating even larger field enhancements in the space where the plasmons interact. As illustrated previously, the plasmons of small particles can be approximated as radiating dipoles, and thus a particle ensemble can be approximated as a system of interacting point dipoles. The electric and magnetic fields radiated by an oscillating dipole are:

$$\boldsymbol{E} = \frac{1}{4\pi\epsilon_0}\left\{k^2(\boldsymbol{n}\times\boldsymbol{p})\times\boldsymbol{n}\frac{e^{ikr}}{r} + [3\boldsymbol{n}(\boldsymbol{n}\cdot\boldsymbol{p}) - \boldsymbol{p}]\left(\frac{1}{r^3} - \frac{ik}{r^2}\right)e^{ikr}\right\} \quad (1.51)$$

$$\boldsymbol{H} = \frac{ck^2}{4\pi}(\boldsymbol{n}\times\boldsymbol{p})\frac{e^{ikr}}{r}\left(1 - \frac{1}{ikr}\right) \quad (1.52)$$

These expressions can be simplified if two regimes are distinguished, near-field coupling, when the gap distance is much smaller than the wavelength ($kr = \frac{2\pi r}{\lambda} \ll 1$), and far-field coupling, when the gap is larger than the wavelength ($kr = \frac{2\pi r}{\lambda} \ll 1$). In the case of plasmonic coupling between sub-wavelenth nanoparticles, the near-field regime is most relevant, and one observes in this case that the $1/r^3$ term dominates the expression in this regime, obtaining the electrostatic result (1.46). It should be noted that while small, the gap size must remain much larger than the size of the nanoparticles themselves in order to maintain the assumption of a point dipole. Equation (1.46) suggests that the two particles in proximity will influence each other's polarization fields, since the charge distribution of a neighboring particle will assert Coulombic forces on other particles in its proximity. The effect of neighboring particles on a particle's plasmon will depend on the polarization of the driving field *(Figure 1.4)*. If transverse modes are excited, then neighboring dipoles compliment the restoring force on the charges and increase the resonance frequency of the plasmon. If longitudinal modes are excited, neighboring particle

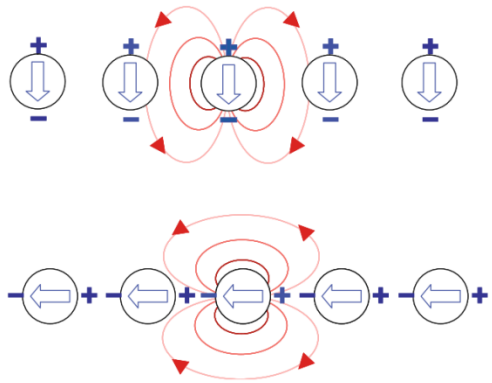

**Figure 1.4|** Cartoon depicting dipoles in nanoparticles excited by transverse (above) and longitudinal (below) polarizations. © 2007 Reprinted with permission from Springer.

polarization fields will inhibit the restoring force and decrease the plasmon resonance frequency[19]

Perhaps one of the most significant properties of plasmons is revealed when one considers the effect of neighboring particles on the electromagnetic energy that would otherwise be lost to scattering or radiative decay if a plasmonic particle was in isolation. Krenn et al.[20] studied this problem experimentally in the context of a linear chain of silver nanoparticles *(Figure 1.5)*. Using Photon Scanning Tunelling Microscopy (PSTM) they observed a severe suppression of the scattered field in a chain of plasmonically coupled nanoparticles and a confinement of electromagnetic energy in the gaps between nanoparticles. The term 'hot-spot' has been coined to describe such gaps containing highly localized electromagnetic fields, and this phenomenon has been pivotal in the rapid development of Surface Enhanced Raman Spectroscopy. It also plays a central role in the application of plasmonic particles to metamaterials.

While a dipolar interaction model has been found to adequately describe the inter-particle spacing dependence of plasmon resonance for spherical particles[21], variations in shape – such

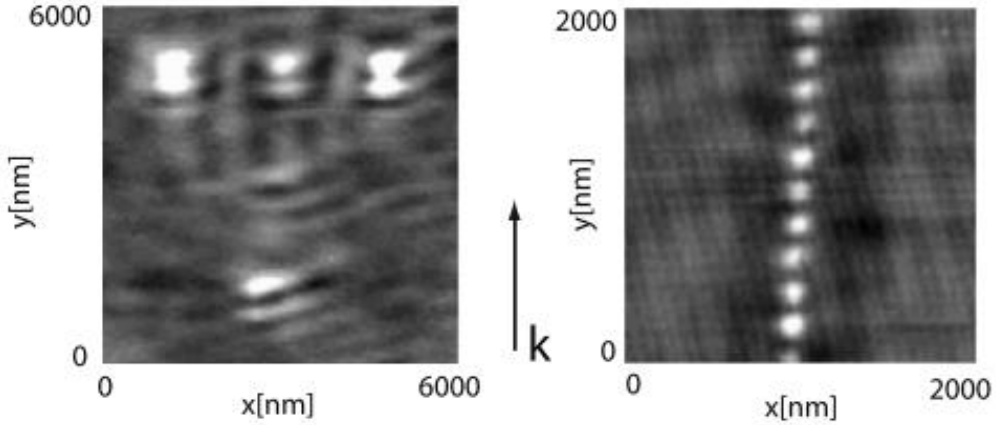


**Figure 1.5|** (Left) PSTM Image of well-spaced nanoparticles, scattering and interference effects are clearly visible. (Right) PSTM image of 1D closely-spaced nanoparticle chain. Electromagnetic fields are localized to the gaps and scattering is significantly reduced.[20] © 2003 Reprinted with permission from Elsevier.

as elliptical particles – have found an exponential dependence instead[22]. It has, therefore, become increasingly important that a more generalized model be formulated that can describe a wider variety of systems with fewer limitations on applicability. This challenge has been recently addressed from the perspective akin to that of molecular orbital hybridization theory -

which a chemist working in the field of plasmonics may find pleasantly familiar. Norlander et al[23] studied the prototypical system of nanoparticle dimers, modelling conduction electrons as an incompressible fluid superimposed on a rigid positive charge that is distributed evenly across the volume of the particles. Plasmon modes would then be represented as deformations in this fluid, which would generate surface charges on the rigid core. This approximation, known as the Jellium Approximation, is a hydrodynamic limit that has previously been found to accurately represent such systems for nanoparticles larger than a few nanometers[24].

The deformation of the electron fluid by the driving field is modelled in the electrostatic limit - similar to the treatment in section 1.1.3 – resulting in a function for surface charge, $\sigma$, that depends on the angular solutions to the Laplace equation. The dynamics of the plasmon coupling is then determined by the instantaneous Coulomb potential, $V(D)$, between the surface charges of two adjacent nanoparticles:

$$V(D) = \int R_1^2 d\Omega_1 \int R_2^2 d\Omega_2 \frac{\sigma_1(\Omega_1)\sigma_2(\Omega_2)}{|\boldsymbol{r_1}-\boldsymbol{r_2}|}, \tag{1.52}$$

where $\Omega$ is the solid angle, $R$ is the radius, and the subscripts 1 and 2 denote each particle in the dimer. This interaction potential is a function of the angular momentum, $l$, as well as the azimuthal number, $m$. By choosing a polar axis along the nanoparticle dimer axis, modes with different values of m decouple and can be solved separately. For each azimuthal number an eigenvalue problem arises with solutions analogous to the hybridization of atomic orbitals.

While Norlander et al create a complete framework for this model, the idea of treating plasmons as atomic orbitals has been alluded to previously[25]. Electrostatic potentials take the place of electronic wavefunctions, and instead of atomic energy levels, one deals with spherical harmonics. In contrast to atomic theory, the fundamental excitation is the dipolar $(l = 1)$ excitation due to the fact that a polarization is necessary to interact with the incident wave. Norlander is able to create a complete picture for the interaction between two dipolar, $(l = 1)$, plasmons as their inter-particle spacing decreases *(Figure 1.6)*.

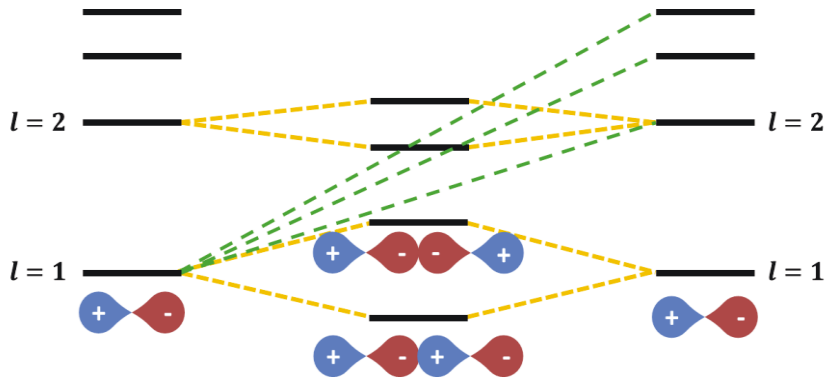


**Figure 1.6|** Plasmon hybridization model showing hybridization between modes of two nanoparticles (orange) and higher-order mode mixing as inter-particle gap becomes very small (green).

At relatively large separations in the near-field, the plasmon modes of the two particles begin to overlap and create symmetric (bonding) and anti-symmetric (anti-bonding) mode configurations which possess a symmetric energy splitting that grows with inverse cubic dependence - in agreement with the classical point dipole approximation. Bonding modes represent a configuration where the electric fields of each particle oscillate in phase with one another while anti-bonding modes represent a completely out-of-phase oscillation. The net dipole moment of a bonding mode is positive and is thus easily excited by an incident electromagnetic field. Such modes have been named 'bright' or 'luminous' modes for their ability to interact with light. In contrast, anti-bonding configurations have no net dipole moment and are not easily 'seen' by the incident field and have been aptly named 'dark' modes.

As the dimer separation decreases, higher order plasmon modes, $l > 2$, are able to 'mix' which results in asymmetric contributions to the energy splitting between the bonding and anti-bonding modes. This results in the exponential dependence of plasmon frequency with inter-particle spacing that has been observed in certain systems. The plasmon hybridization model has been used to predict the responses of non-trivial nanoparticle geometries such as nanoshells[26] and provides a relatively straightforward method of predicting the response of complex nanoparticle arrangements without resorting to time consuming computational methods[27].

### 1.1.6 Summary

In essence, plasmons are a pathway that allow for the manipulation of electromagnetic fields on a scale that was previously barred by the diffraction limit. On the basis of optical

confinement alone one can envision intriguing applications in nanophotonic circuitry, utilizing the rapid information transmission capability of the photon at the scale of the electron[28]. The resonant absorption properties of plasmons and the energy enhancement that they provide are already being utilized to enhance photovoltaic light trapping and thus the efficiency of thin film solar cells[29]. While many have bemoaned the lossy nature of plasmons in noble metals, it has been shown that this loss-property can be utilized to as a method for targeted, photothermally induced morbidity in tumor cells[30]. Finally, the enhanced emission that can be obtained in the vicinity of a plasmonic resonance can enhance non-linear optical phenomena[31] and greatly improve detection capabilities for analytical techniques such as single molecule fluorescence[32].

While the properties of individual plasmonic structures have a great deal of potential applications, an even greater potential is unlocked when one begins to manipulate not only the geometry of a plasmonic structure itself but the organization of many such structures on a macroscopic scale. In such systems each sub-wavelength plasmonic structure is observed as a single pseudo or 'meta' atom by an incoming electromagnetic field. A material consisting of many such meta-atoms can be tailored to interact with light in ways that have yet to be observed in naturally occurring materials. The characteristics of such 'metamaterials' and how they can be designed and fabricated shall be explored next.

## 1.2 Negative index metamaterials

The broad scope of what has been referred to as a metamaterial in the literature today is partially due to its nebulous definition[33]. The Greek origin of the prefix 'meta' (meaning 'beyond) does little to illuminate. To avoid offense by exclusion, this thesis will use its broadest definition, that is, a material with properties that emerge as a result of the sub-wavelength unit structure of the material rather than the constituent atomic structure of the material itself. In the interest of brevity, only one class of such materials will be discussed in detail, metamaterials that display a negative refractive index.

The optical properties of a conventional material are determined by the atoms that constitute the material itself. As discussed previously these properties can be completely described by the

optical parameters; the permittivity and permeability. These parameters are macroscopic in nature, describing the homogenized interaction of light with the electronic structure of the constituent atoms on the spatial and temporal scale of the incident light wave. If one were to embed a large number of gold nanoparticles into a transparent medium and observe the effect on an electromagnetic field passing through it, one would see that the material would behave differently from a material that was simply a homogeneous mixture of gold atoms and the transparent medium. The incident field interacts, not only with the atoms within the material, but with the collective electric (or magnetic) response of the nanoparticles themselves - it is unable to distinguish between the microscopic fields generated in the material. The result is an interaction that can be described with an effective permittivity and permeability. The nanoparticles themselves are 'meta-atoms' making up the metamaterial. This example has a fourth century embodiment in the Lycurgus Cup, a Roman glass challis displayed at the British Museum. The cup is a composite of ruby glass with embedded gold nanoparticles and appears green when light reflects off its surface and red when light is transmitted through it.

The groundwork for contemporary research in negative index metamaterials was laid by Victor Veselago in his paper "Electrodynamics of substances with simultaneously negative values of ϵ and μ."[34], however, the idea has been considered as early as 1904 by Sir Arthur Schuster[35]. Veselago provided a systematic theoretical investigation into the implications of a material having both a negative permittivity and permeability in the same frequency range. Recalling Maxwell's equations and the definition of refractive index, $n^2 = \epsilon\mu$, one can observe that there is a mathematical ambiguity in the sign of the root when solving for $n$. The conventional choice of the positive root does not originate from any physical law, and is a consequence of the fact that no known natural materials have ever displayed a case whereby the negative root need be considered. In order for such a case to arise, the real components of $\epsilon$ and $\mu$ must be simultaneously negative – the imaginary components of these two parameters must always be positive in order to satisfy causality.

The index of refraction is a fundamental material parameter that appears in almost all basic optical relations, and the possibility of a negative value of $n$ has far reaching implications. In the

context of a monochromatic plane wave propagating on the z-axis with a wave-vector $k$ and angular frequency $\omega$, Maxwell's equations (1.3) and (1.4) reduce to:

$$\boldsymbol{k} \times \boldsymbol{H} = -\omega \epsilon_0 \epsilon \boldsymbol{E} \tag{1.53}$$

$$\boldsymbol{k} \times \boldsymbol{E} = \omega \mu_0 \mu \boldsymbol{H} \tag{1.54}$$

These two equations are the progenitors of the 'right-hand rule'. Positive values of $\epsilon$ and $\mu$ result in a right-handed coordinate system for the vectors $\boldsymbol{k}$, $\boldsymbol{E}$ and $\boldsymbol{H}$. The wave-vector, $\boldsymbol{k}$, represents a photon's phase velocity. For a monochromatic plane wave it is parallel to the Poynting vector, $\boldsymbol{S} = \boldsymbol{E} \times \boldsymbol{H}$, the direction of energy flux. In a negative index material (NIM), both $\epsilon$ and $\mu$ are negative, and the three vectors instead form a left-handed coordinate system – this has led to the term 'Left-Handed Materials' to describe NIMs. A left-handed coordinate system results in a wave-vector that is anti-parallel to the Poynting vector, and one is left with the unintuitive result of a phase velocity that propagates in an opposite direction to the energy flux.

A more visual illustration of the implications of a negative-refractive index can be obtained by observing the effect of a change in the sign of the refractive index in Snell's Law *(Figure 1.7)*:

$$\frac{n_1}{n_2} \sin \theta_1 = \sin \theta_2 \tag{1.55}$$

One immediately observes that at the boundary between a positive refractive index and a negative refractive index, a ray will refract on the same side of the normal. Consequently, the behavior of convex and concave lenses will be reversed, with concave lenses diverging rays while convex lenses converge them.

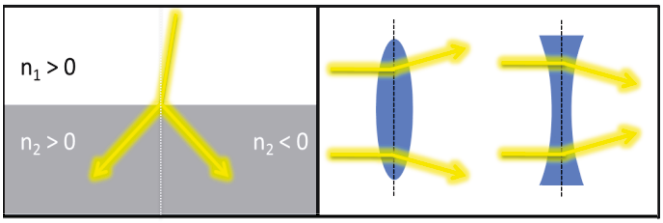


**Figure 1.7|** Illustration of negative refraction across a boundary (left) and the inversion of the behavior of convex and concave lenses (right).

Other physical phenomena that will undergo a reversal are the Doppler effect – the frequency of a wave will decrease as the observer moves towards the source – and a reversed Vavilov-Cerenkov effect –

the phase velocity of radiation emitted by a moving charged particle will be directed towards the particle rather than away.

These predictions have lacked an experimental demonstration because no known natural materials display simultaneous values of $\epsilon$ and $\mu$ at the same frequency and, until recently, no synthetic material has either. Smith et al. produced the first composite material which displayed a negative permittivity and permeability and have since shown that such a material can be used to 'cloak' an object from an electromagnetic field[36,37]. Pendry – another pioneer in this field - has shown that a NIM can be engineered to focus both far and evanescent fields of an image and thus bypass the resolution limit of light in a 'super-lensing' effect[38].

While the seminal work in metamaterials began with the fabrication of a NIM, the definition of metamaterials has since expanded to encompass any material that can assert an unprecedented level of control over the optical parameters $\epsilon$ and $\mu$ on the sub-wavelength scale. From an alternate perspective, metamaterials are materials that transform the space through which light is travelling, guiding its path with sub-wavelength precision. The application of metamaterials to this purpose has been named 'transformation optics'[39].

### 1.2.1 Artificial magnetism

In section 1.1.2 it was shown that below the plasma frequency of a metal, the real component of the permittivity is negative. This is true of all metals, such that light which is incident on metals below their plasma frequency is mostly reflected, giving metals their characteristic lustre. It is thus relatively simple to produce a negative permittivity in a wide range of the electromagnetic spectrum by modifying the properties of a metal that affect its plasma frequency. This is not the case for permeability. Inherently magnetic materials obtain their magnetic character from the aligned spins of electrons which can be excited in the radio frequency spectrum. When the frequency of incident electromagnetic radiation increases beyond the radio frequencies, the oscillations of the electron spins can no longer keep up with the time scale of the electromagnetic wave, and the material no longer elicits a magnetic response – the permeability of the material approaches unity. There is no equivalent of a magnetic plasma for any known natural material and thus no manner to tailor at what

frequency the magnetic response for a material can occur. The reason for this lies in a natural asymmetry, namely that there is an abundance of electric charges and a complete absence of magnetic ones.

Maxwell's equations in the absence of a source are completely symmetric, and the lack of magnetic monopoles in nature remains an empirical observation, accounted for in theory by the phenomenological fine structure constant, $\alpha = \frac{e^2 c\mu_0}{2h} = \frac{e^2}{4\pi\epsilon_0}$. This fundamental constant expresses the electromagnetic coupling strength between elementary charged particles and illustrates the miniscule magnitude of the free space permeability compared to the free space permittivity.

The main challenge in the fabrication of a NIM has thus been the generation of a magnetic plasma in the same frequencies for which an electric plasma can form. This problem was considered by Pendry for a system of square arrays of very long metal cylinders *(Figure 1.8(a))* with horizontal dimensions much smaller than the wavelength of the driving field, such that the microscopic fields produced in the material can be averaged into an effective permeability and permittivity for the whole structure[40]. He posited that the driving field would induce a current around the circumference of the cylinders which, by Faraday's Law, would result in an induced magnetic field whose magnitude depended on the cylinder dimensions and electric properties.

The induced magnetic field is quite limited, but Pendry showed that by replacing each cylinder with two concentric metal tubes with gaps placed on opposite ends - known as a split ring – a large capacitance could be introduced between the two cylinders which would greatly magnify the magnetic response *(Figure 1.8(b))*. The capacitance balances the inductance present – by virtue of the ring-shaped cylinders – resulting in a resonant response akin to an LC electronic circuit.

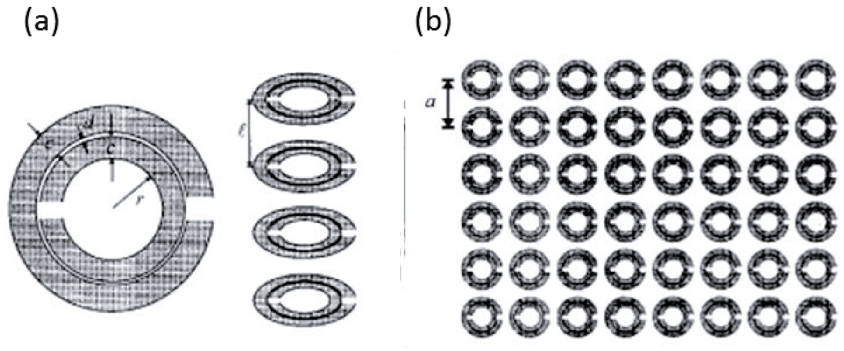


**Figure 1.9|** (a) Split-Ring Resonator geometry. (b) Square array of Split-Ring Resonators.[40] © 2000 Reprinted with permission from APS.

This resonant response manifests in the effective permeability of the whole structure and one obtains a "magnetic plasma frequency" at which the effective permeability is greatly enhanced – a facsimile to the electric plasma frequency of metals.

It is not necessary to extrude the split-ring geometry into cylinders to obtain this effect. Indeed, Pendry has shown that a two dimensional square array of split-rings *(Figure 1.9)* will elicit a similar phenomenon. The relevance of this is that a magnetic plasma effect could be induced in an isotropic structure such that all polarizations of an electromagnetic field would induce a response (in the cylindrical case only a field polarized along the axes of the cylinders would do so). For a three-dimensional array of these two-dimensional split ring resonators, he obtains the following expression for the effective permeability:

$$\mu_{eff} = \frac{1-\frac{\pi r^2}{a^2}}{1+\frac{2l\sigma_1}{\omega r \mu_0 i}-\frac{3lc_0^2}{\pi\omega^2 r^3 \ln\frac{2c}{d}}}, \tag{1.56}$$

where $\sigma_1$ is the resistance per unit length around the circumference of the ring, $c_0$ is the speed of light in vacuum, $\omega$ is the driving field frequency, $d$ is the size of the gap between the two rings, $r$ is the inner radius of the inner ring, $c$ is the thickness of the rings, $l$ and $a$ the vertical and horizontal distance between split rings respectively. The effective permeability will be resonantly enhanced at:

$$\omega_{p,\mu_{eff}} = \frac{3lc_0^2}{\pi r^3 \ln\frac{2c}{d}} \tag{1.57}$$

One can see that there is a scaling of the resonant frequency with the size of the split rings and that higher plasma frequencies are obtained by shrinking the unit structure.

### 1.2.2 Optical frequency metamaterials

Pendry's analysis resulted in the fabrication of the first NIM by Smith et al. at GHz (microwave) frequencies, printed on a circuit board[41]. The design incorporated Pendry's split ring resonators to produce a negative permeability with a set of metal wires to create an electric plasma in the same frequency. He demonstrates the presence of a negative refractive index by showing how each structure individually (the split rings or the wires) do not allow the transmission of a

microwave field (since the refractive index becomes imaginary and virtually all radiation is absorbed) but when incorporated together create a passband at around 5 Ghz.

Since then, the one of the most desired goals has been to produce NIM at increasingly higher frequencies with the optical frequencies in mind. The importance lies in the previously alluded to observation that there are no materials with magnetic properties in that part of the electromagnetic spectrum. The split ring resonator design has been further refined over time[36,42] to elevate the magnetic plasma frequency into the THz (optical) region and other geometries have also been explored[43–45], however, as the frequency of operation increases, the scaling law illustrated by Pendry begins to break down[46].

Below the optical frequency, the kinetic energies of electrons in a metal and the loss associated with collisions can be largely neglected due to the fact that the magnetic response generated is much larger. Disregarding the challenge of fabricating metal structures at scales small enough such that the driving field still only perceives an effective response (which will be discussed later), at high frequencies, the kinetic energy of the electrons becomes high enough to open numerous competing pathways for energy transfer (such as electron-phonon interactions) that lead to significant losses in conduction. These Ohmic losses decrease the displacement current elicited by the incoming field and, consequently, hamper the magnetic response. The current consensus is that any system based on conventional current is limited to operational frequencies up to the near-IR.

### 1.2.3 Nanoparticle rings as optical metamaterials

Conventional current is not necessary to create a magnetic response. Maxwell's equation (1.4) tells us that a changing displacement current, $\delta \boldsymbol{D}/\delta t$ , can still induce a magnetic field if $\boldsymbol{J}_{\boldsymbol{free}} = 0$. Unlike the traditional current of moving charges, a displacement current comes about through the oscillations of relatively bound charges, and is a sum of the impinging field and the induced polarization in the material as formulated in equation (1.5).

This type of induction has been found to occur in systems known as sub-wavelength plasmonic crystals[47] – arrays of clusters of plasmonic nanoparticles called inclusions – where the

oscillation of plasmons coupled to one another constitute a displacement current. Even a simple array of plasmonically coupled dimers can produce a non-negligible magnetic response. As discussed in section 1.1.5, one expects plasmon modes to hybridize and form symmetric and anti-symmetric modes[26]. In a symmetrical resonance, the dipoles generated by plasmonic excitation in adjacent particles move in phase and behave as one plasmon. In the anti-symmetric 'dark' mode, on the other hand, the electrons in neighboring particles move exactly out of phase with each other and the net electric dipole is cancelled out[48]. This leaves behind only magnetic dipole and quadrupolar responses, and a displacement current loop is formed between two particles that is analogous to a current loop of freely moving charges. The result is a net magnetic dipole moment generated between the two particles.

Unfortunately, plasmonic systems are highly sensitive to loss mechanisms, and thus the choice of an appropriate geometry is essential to a functional metamaterial[49]. Higher order multipolar electric modes divert power away from the magnetic dipole and must be minimized or eliminated by symmetry in order to maximize the efficiency of the desired magnetic response[50]. Engheta et al. were the first to consider an array of plasmonically coupled nanoparticles arranged in a ring *(Figure 1.10)*, a sub-wavelength ring inclusion that could create a magnetic response analogous to that of a conventional wire loop[51]. In the process of forming an analytical model for such a system, they determine that the symmetry of such an arrangement will diminish or completely cancel higher order multipoles and increase the quality of the magnetic dipolar response.

By assuming that the inclusions are very small compared to the wavelength (to allow the use of the quasi-static approximation), and that the distance between the nanoparticles in the ring is relatively large compared to their diameters (in order to treat them as point electric dipoles), Engheta et al. determine the following expression for the magnetic polarizability, $\alpha_{mm}^{-1}$, of a nano-ring:

$$\alpha_{mm}^{-1} = \frac{4\epsilon_b}{Nk_b^2R^2}\alpha^{-1} - i\left(\frac{k_b^3}{6\pi} - \frac{2k_b}{3\pi NR^2}\right) + \frac{1}{16\pi Nk_b^2R^5}\sum_{l\neq n}^{N}\frac{3+\cos[2\pi(l-n)/N]}{|\sin[\pi(l-n)/N]|^3} \quad (1.58)$$

Where $\epsilon_b$ is the permittivity of the background medium, $k_b = \omega/\sqrt{\epsilon_b\mu_0}$ is the background wave number, $N$ is the number of particles in the loop, and $R$ is the radius of the ring. For a small homogeneous nanosphere with permittivity $\epsilon$, the polarizability, $\alpha$, is given by[17]:

$$\alpha = \left[\left(4\pi\epsilon_b a^3\frac{\epsilon-\epsilon_b}{\epsilon+2\epsilon_b}\right)^{-1} - i\frac{k_b^3}{6\pi\epsilon_b}\right]^{-1},$$

which is a rearrangement of equation 1.47 to solve for the polarizability. Note that the resonance of the magnetic polarizability is slightly shifted from that of an individual nanosphere due to the coupling between the nanospheres constituting the ring.

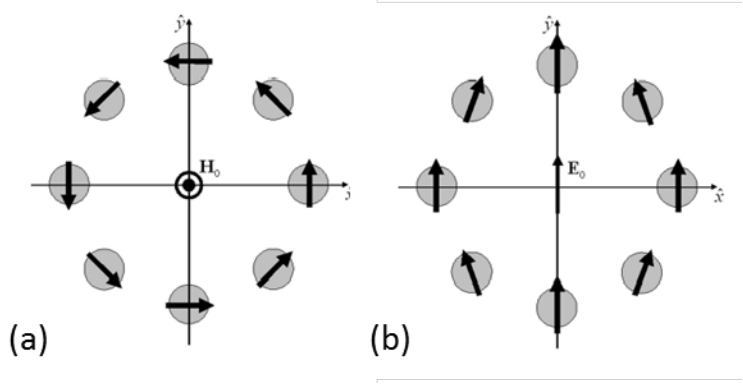


**Figure 1.10|** Circular array of nano-spheres in the x-y plane excited by (a) a time varying magnetic field directed along z or (b) a time varying electric field directed along y. The vectors on each particle indicate the induced dipole moments in each case[51]. © 2006 Reprinted with permission from Optics Infobase.

To ensure that the magnetic field incident on the ring is uniform across the whole structure so that the quasi-static approximation will hold, a single ring is modelled as being excited by $N$ symmetrical plane waves that are impinged through the center of each particle tangent to the arc of the ring. This model ensures that the magnetic component of each impinging wave is passing perpendicular through the plane of the ring. This method of excitation will also ensure that the electric dipoles excited by the generated electric field cancel each other out by symmetry, allowing one to extract the magnetic and electric polarizability

separately[52]. The electric polarizability,$\alpha_{ee}$, is isolated by impressing a different set of plane waves on the ring and can be solved numerically to determine the induced dipole moments.

In order to obtain the effective permeability and permittivity from $\alpha_{mm}$ and $\alpha_{ee}$ respectively, an effective medium theory (EMT) is required which can predict the response of a composite material consisting of numerous ring inclusions embedded in a background medium since attempting to solve such a system exactly using Maxwell's equations and accounting for every inter-particle interaction would be a herculean task. There is no general theory that can be applied to all metamaterial systems, however, there are analytical approaches that attempt to homogenize such composites to obtain average values for optical parameters[53]. The effective permittivity and permeabilities obtained are formulas that involve the responses of the individual inclusions combined with some sort of mixing rule.

### 1.2.4 Effective medium theory and the Maxwell-Garnet model

One of the most commonly used EMT models is the Maxwell-Garnett theory[54] which, instead of considering all possible interactions between inclusions under an electromagnetic field, only looks at the difference between the local field felt by an inclusion and the average field across the whole composite.

The local field felt by an inclusion is the sum of the external field and the electric fields generated by all other particles in the composite:

$$\boldsymbol{E_{loc}} = \boldsymbol{E_{ext}} + \sum_{j\neq i} \boldsymbol{E_{ij}},$$

where $\boldsymbol{E_{ij}}$ is the field created at $i$ by $j$. The average field across the composite, on the other hand, is given by:

$$\widehat{\boldsymbol{E}} = \frac{1}{V} + \int_V \boldsymbol{E}(\boldsymbol{r})dV,$$

where $V$ is the volume of the composite and $\boldsymbol{r}$ is a position vector. The difference between these two fields gives:

$$\boldsymbol{E_{loc}} - \widehat{\boldsymbol{E}} = \boldsymbol{E_{ext}} - \widehat{\boldsymbol{E}}_{\boldsymbol{ext}} + \sum_{j\neq i}\left(\boldsymbol{E_{ij}} - \widehat{\boldsymbol{E}}_{\boldsymbol{ij}}\right) - \widehat{\boldsymbol{E}}_{\boldsymbol{ii}} \tag{1.59}$$

This problem can be drastically simplified with two reasonable assumptions. In most cases, the source of the impinging electromagnetic field can be assumed to be far enough away that the whole composite experiences the same field across its volume, thus the difference between the external field at any point and the average external field is zero, $\boldsymbol{E_{ext}} - \widehat{\boldsymbol{E}}_{\boldsymbol{ext}} \approx 0$.

If all the microscopic dimensions inside the composite are much smaller than the wavelength of the driving field, then one can apply the quasi-static approximation and the fields of distant inclusions can be perceived as point dipoles. In a periodic or completely random arrangement of such inclusions, the radiation from all dipoles surrounding the inclusion of interest will cancel each other out and the summation term above is also nil, $\sum_{j\neq i}\left(\boldsymbol{E_{ij}} - \widehat{\boldsymbol{E}}_{\boldsymbol{ij}}\right) \approx 0$**,** as long as one only studies the inclusions far from the boundary of the composite.

The main contribution to the difference between the local field and the average field is thus the average field of the inclusion in question, and one only need determine the local effect of the inclusion, $\widehat{\boldsymbol{E}}_{\boldsymbol{ii}}$. In order to do this, each inclusion is partitioned into a spherical cell of volume $V$. The inclusion itself is modelled as a collection of $m$ point charges, $q_m$, located at $\boldsymbol{r_m}$ within the cell. The value of the local electric field for a superposition of $m$ charges at any point is given by:

$$\boldsymbol{E_{ii}}(\boldsymbol{r}) = \sum_m \boldsymbol{\nabla}_{\mathrm{m}} \frac{q_m}{4\pi\epsilon_0|\boldsymbol{r} - \boldsymbol{r_m}|}$$

The averaged field is then,

$$\widehat{\boldsymbol{E}}_{\boldsymbol{ii}} = \frac{1}{V}\sum_m \boldsymbol{\nabla}_{\mathrm{m}} \int_V \frac{q_m}{4\pi\epsilon_0|\boldsymbol{r} - \boldsymbol{r_m}|} dV = -\sum_m \mathbf{E}_{\mathrm{m}}$$

where,

$$\boldsymbol{E}_m = -\boldsymbol{\nabla}_{\mathrm{m}} \int_V \frac{q_m}{4\pi\epsilon_0 V|\boldsymbol{r} - \boldsymbol{r_m}|} dV$$

$\boldsymbol{E_m}$ takes the form of Gauss' Law such that,

$$\boldsymbol{\nabla}_{\mathrm{m}} \cdot \boldsymbol{E}_m = \frac{\rho}{\epsilon_0} = \frac{q_m}{V\epsilon_0}$$

where $\rho$ is the charge density. Since the cell takes the shape of a sphere the volume depends only on $\boldsymbol{r}_m$ and thus:

$$\boldsymbol{E}_m = -\frac{\mathrm{q_m}}{3\epsilon_0 V}\boldsymbol{r}_m$$

Substituting this back into the expression for $\widehat{\boldsymbol{E}}_{\boldsymbol{ii}}$,

$$\widehat{\boldsymbol{E}}_{\boldsymbol{ii}} = -\sum_m \mathbf{E}_\mathrm{m} = -\frac{1}{3\epsilon_0 V}\sum_m \mathrm{q_m}\boldsymbol{r}_m$$

The product $q_m\boldsymbol{r}_m$ is the electric dipole moment, $\boldsymbol{p}$, and its sum across all dipoles divided by the volume yields the average polarization, $\boldsymbol{P}$. Therefore,

$$\widehat{\boldsymbol{E}}_{\boldsymbol{ii}} = -\frac{\boldsymbol{P}}{3\epsilon_0} \tag{1.60}$$

Substituting this back into (1.59) with the approximations discussed earlier one obtains:

$$\boldsymbol{E}_{\boldsymbol{loc}} = \widehat{\boldsymbol{E}} + \widehat{\boldsymbol{E}}_{\boldsymbol{ii}} = \widehat{\boldsymbol{E}} + \frac{\boldsymbol{P}}{3\epsilon_0} \tag{1.61}$$

This expression is known as the Lorenz-Lorentz formula. The average field $\widehat{\boldsymbol{E}}$ is simply the macroscopic field measured in the medium and is often simply denoted by $\boldsymbol{E}$.

The average polarization, $\boldsymbol{P}$, is also given by:

$$\boldsymbol{P} = \frac{\boldsymbol{p}}{V} = N_d\boldsymbol{p} = N_d\alpha\boldsymbol{E}_{\boldsymbol{loc}}$$

Where $N_d$ is the number density of dipoles with polarizability $\alpha$. Substituting (1.61) into this expression,

$$\boldsymbol{P} = \frac{N_d\alpha}{1 - \frac{N_d\alpha}{3\epsilon_0}}\boldsymbol{E}$$

Now, recalling the definition of the displacement field, $\boldsymbol{D}$:

$$\boldsymbol{D} = \epsilon_0\boldsymbol{E} + \boldsymbol{P} = \epsilon_{eff}\boldsymbol{E}$$

Where $\epsilon_{eff}$ is the homogenized permittivity of an isotropic composite. We can deduce that,

$$\epsilon_{eff} = \epsilon_0 + \frac{N_d\alpha}{1 - \frac{N_d\alpha}{3\epsilon_0}} \tag{1.62}$$

This is known as the Clausius-Mossotti formula. A similar treatment yields an identical form for $\mu_{eff}$ involving the magnetic polarizability.

Using this formula one obtains the effective permittivity and permeability for a composite consisting of randomly arranged ring inclusions by utilizing the magnetic and electric polarizabilities obtained by Engheta et al. as described in section 1.2.3:

$$\mu_{eff} = \mu_0 \left( 1 + \frac{1}{N_d^{-1}\alpha_{mm}^{-1} - \frac{1}{3}} \right) \tag{1.63}$$

$$\epsilon_{eff} = \epsilon_0 \left( 1 + \frac{1}{\epsilon_0 N_d^{-1}\alpha_{ee}^{-1} - \frac{1}{3}} \right) \tag{1.64}$$

### 1.2.5 Loss and Q-factor

It should be noted that the above analysis of plasmonically coupled rings neglects the radiation contribution from the individual dipoles of the particles to the local electric and magnetic fields. The result of this is the violation of energy conservation relations. Additionally, the imaginary component of the polarizabilities is not taken into account, and thus the above static model does not consider radiation and Ohmic losses. A more detailed analysis was carried out by Engheta et al. that treats the rings in a dynamic environment[50] and determines some fundamental limits to the nanoring geometry. It is found that the amplitude of the induced magnetic dipole moment is limited by radiation damping and ohmic losses. It is also determined that the detrimental effect of higher order electric multipoles is reduced by increasing the number of particles in the ring and decreasing the ring diameter.

Using this dynamical theory, a Q-factor of the magnetic resonance can be evaluated for a ring of plasmonic spheres with radius $a$ and a permittivity determined by the Drude model with resonance frequency, $\omega_0$, that neglects the effects of plasmonic losses. The magnetic resonance frequency of the ring is given by,

$$\omega_{m0} = \omega_0 \sqrt{1 - \frac{a^3}{16R^3} \sum_{j=1}^{N-1} \frac{3 + \cos\frac{2j\pi}{N}}{\sin^3\frac{j\pi}{N}}} \tag{1.64}$$

The Q-factor, which is the ratio of the energy stored by the rings and the energy dissipated in one oscillation of the induced magnetic dipole, is then obtained via:

$$Q = \frac{6\omega_{m0}^2}{N\tilde{k}_b^5 a^3 R^2} \tag{1.64}$$

where $\tilde{k}_b = \omega_{m0}/\sqrt{\epsilon_b \mu_0}$.

It can be seen that the quality factor increases with a reduction in ring radius and a lower particle radius.

## 1.3 Summary

This chapter has highlighted the utility of plasmonically coupled particles in the pursuit of obtaining negative index metamaterials with an emphasis on plasmonically coupled nanoparticle rings. With a theoretical framework now detailed, the question of how such structures may be fabricated is pertinent. The challenges of top-down fabrication methodologies in accessing the necessary sub-wavelength scale are described and the possible use of bottom-up templated self-assembly to address those challenges will be addressed in Chapter 2.

## Citations


1. Sommerfeld, A. About the propagation of electrodynamic waves along a wire. *Ger. Ann. d. Phys* **67,** 233–290 (1899).

2. Zenneck, J. Propagation of plane EM waves along a plane conducting surface. *Ann. Phys.(Leipzig)* **23,** 907 (1907).

3. Ritchie, R. H. & Marusak, A. L. The surface plasmon dispersion relation for an electron gas. *Surf. Sci.* **4,** 234–240 (1966).

4. Kretschmann, E. & Raether, H. Radiative decay of non radiative surface plasmons excited by light(Surface plasma waves excitation by light and decay into photons applied to nonradiative modes). *Zeitschrift Fuer Naturforschung, Tl. A* **23,** 2135 (1968).

5. Fleischmann, M., Hendra, P. J. & McQuillan, A. J. Raman spectra of pyridine adsorbed at a silver electrode. *Chem. Phys. Lett.* **26,** 163–166 (1974).

6. Takahara, J., Yamagishi, S., Taki, H., Morimoto, A. & Kobayashi, T. Guiding of a one-dimensional optical beam with nanometer diameter. *Opt. Lett.* **22,** 475 (1997).

7. Ebbesen, T. W., Lezec, H. J., Ghaemi, H. F., Thio, T. & Wolff, P. A. Extraordinary optical transmission through sub-wavelength hole arrays. *Nature* **391,** 667–669 (1998).

8. Egri, I. Excitons and plasmons in metals, semiconductors and insulators: A unified approach. *Phys. Rep.* **119,** 363–402 (1985).

9. Drude, P. Zur Elektronentheorie der Metalle. *Ann. Phys.* **306,** 566–613 (1900).

10. Maier, S. A. *Plasmonics: Fundamentals and Applications*. *tu-chemnitz.de* (Spring Science and Business Media LLC, 2007).

11. Marder, M. P. *Condensed matter physics*. 895 (John Wiley, 2000).

12. Moores, A. & Goettmann, F. The plasmon band in noble metal nanoparticles: an introduction to theory and applications. *New J. Chem.* **30,** 1121 (2006).

13. Jackson, J. *Classical electrodynamics*. (John Wiley & Sons, Inc., 1962).

14. Fayer, M. D. *Elements of Quantum Mechanics*. 320 (Oxford University Press, 2001).

15. Willets, K. a & Van Duyne, R. P. Localized surface plasmon resonance spectroscopy and sensing. *Annu. Rev. Phys. Chem.* **58,** 267–97 (2007).

16. Mie, G. Beiträge zur Optik trüber Medien, speziell kolloidaler Metallösungen. *Ann. Phys.* **330,** 377–445 (1908).

17. Bohren, C. F. & Huffman, D. R. *Absorption and Scattering of Light by Small Particles*. 544 (John Wiley & Sons, 2008).

18. Kelly, K. L., Coronado, E., Zhao, L. L. & Schatz, G. C. The Optical Properties of Metal Nanoparticles: The Influence of Size, Shape, and Dielectric Environment. *J. Phys. Chem. B* **107,** 668–677 (2003).

19. Maier, S. A., Kik, P. G. & Atwater, H. A. Observation of coupled plasmon-polariton modes in Au nanoparticle chain waveguides of different lengths: Estimation of waveguide loss. *Appl. Phys. Lett.* **81,** 1714 (2002).

20. Krenn, J. R. *et al.* Light field propagation by metal micro- and nanostructures. *J. Microsc.* **202,** 122–128 (2001).

21. Rechberger, W. *et al.* Optical properties of two interacting gold nanoparticles. *Opt. Commun.* **220,** 137–141 (2003).

22. Ghosh, S. K. & Pal, T. Interparticle coupling effect on the surface plasmon resonance of gold nanoparticles: from theory to applications. *Chem. Rev.* **107,** 4797–862 (2007).

23. Nordlander, P., Oubre, C., Prodan, E., Li, K. & Stockman, M. I. Plasmon Hybridization in Nanoparticle Dimers. *Nano Lett.* **4,** 899–903 (2004).

24. Prodan, E. & Nordlander, P. Structural Tunability of the Plasmon Resonances in Metallic Nanoshells. *Nano Lett.* **3,** 543–547 (2003).

25. Gersten, J. & Nitzan, A. Photophysics and photochemistry near surfaces and small particles. *Surf. Sci.* **158,** 165–189 (1985).

26. Prodan, E., Radloff, C., Halas, N. J. & Nordlander, P. A hybridization model for the plasmon response of complex nanostructures. *Science* **302,** 419–22 (2003).

27. Hentschel, M. *et al.* Transition from isolated to collective modes in plasmonic oligomers. *Nano Lett.* **10,** 2721–6 (2010).

28. Guo, X. *et al.* Direct coupling of plasmonic and photonic nanowires for hybrid nanophotonic components and circuits. *Nano Lett.* **9,** 4515–9 (2009).

29. Gan, Q., Bartoli, F. J. & Kafafi, Z. H. Plasmonic-enhanced organic photovoltaics: breaking the 10% efficiency barrier. *Adv. Mater.* **25,** 2385–96 (2013).

30. Hirsch, L. R. *et al.* Nanoshell-mediated near-infrared thermal therapy of tumors under magnetic resonance guidance. *Proc. Natl. Acad. Sci. U. S. A.* **100,** 13549–54 (2003).

31. Genevet, P. *et al.* Large enhancement of nonlinear optical phenomena by plasmonic nanocavity gratings. *Nano Lett.* **10,** 4880–3 (2010).

32. Zhang, J., Fu, Y., Chowdhury, M. H. & Lakowicz, J. R. Metal-enhanced single-molecule fluorescence on silver particle monomer and dimer: coupling effect between metal particles. *Nano Lett.* **7,** 2101–7 (2007).

33. Sihvola, A. Metamaterials in electromagnetics. *Metamaterials* **1,** 2–11 (2007).

34. Veselago, V. G. The Electrodynamics of Substances with Simultaneously Negative Values of $\epsilon$ and μ. *Sov. Phys. Uspekhi* **10,** 509–514 (1968).

35. Schuster, S. A. *An Introduction to the Theory of Optics*. 340 (E. Arnold, 1904).

36. Shelby, R., Smith, D. & Schultz, S. Experimental verification of a negative index of refraction. *Science (80-. ).* **77,** (2001).

37. Schurig, D. *et al.* Metamaterial electromagnetic cloak at microwave frequencies. *Science* **314,** 977–80 (2006).

38. Pendry, J. B. Negative Refraction Makes a Perfect Lens. *Phys. Rev. Lett.* **85,** 3966–3969 (2000).

39. Pendry, J. B., Aubry, A., Smith, D. R. & Maier, S. A. Transformation optics and subwavelength control of light. *Science* **337,** 549–52 (2012).

40. Pendry, J. B., Holden, A. J., Robbins, D. J. & Stewart, W. J. Magnetism from conductors and enhanced nonlinear phenomena. *IEEE Trans. Microw. Theory Tech.* **47,** 2075–2084 (1999).

41. Smith, D., Padilla, W., Vier, D., Nemat-Nasser, S. & Schultz, S. Composite medium with simultaneously negative permeability and permittivity. *Phys. Rev. Lett.* **84,** 4184–7 (2000).

42. Enkrich, C. *et al.* Magnetic Metamaterials at Telecommunication and Visible Frequencies. *Phys. Rev. Lett.* **95,** 203901 (2005).

43. Bayindir, M., Aydin, K., Ozbay, E., Markoš, P. & Soukoulis, C. M. Transmission properties of composite metamaterials in free space. *Appl. Phys. Lett.* **81,** 120 (2002).

44. Zhang, S. *et al.* Experimental Demonstration of Near-Infrared Negative-Index Metamaterials. *Phys. Rev. Lett.* **95,** 137404 (2005).

45. Dolling, G., Wegener, M., Soukoulis, C. M. & Linden, S. Negative-index metamaterial at 780 nm wavelength. (2006).

46. Zhou, J. *et al.* Saturation of the Magnetic Response of Split-Ring Resonators at Optical Frequencies. *Phys. Rev. Lett.* **95,** 223902 (2005).

47. Shvets, G. & Urzhumov, Y. A. Electric and magnetic properties of sub-wavelength plasmonic crystals. *J. Opt. A Pure Appl. Opt.* **7,** S23–S31 (2005).

48. Grigorenko, a N. *et al.* Nanofabricated media with negative permeability at visible frequencies. *Nature* **438,** 335–8 (2005).

49. Urzhumov, Y. A. & Shvets, G. Optical magnetism and negative refraction in plasmonic metamaterials. *Solid State Commun.* **146,** 208–220 (2008).

50. Alù, A. & Engheta, N. Dynamical theory of artificial optical magnetism produced by rings of plasmonic nanoparticles. *Phys. Rev. B* **78,** 1–10 (2008).

51. Alù, a, Salandrino, a & Engheta, N. Negative effective permeability and left-handed materials at optical frequencies. *Opt. Express* **14,** 1557–67 (2006).

52. Ishimaru, A., Kuga, Y. & Jandhyala, V. Generalized constitutive relations for metamaterials based on the quasi-static lorentz theory. *IEEE Trans. Antennas Propag.* **51,** 2550–2557 (2003).

53. Cai, W. & Shalaev, V. *Optical Metamaterials*. (Springer New York, 2010). doi:10.1007/978-1-4419-1151-3

54. Tretyakov, S. *Analytical Modeling in Applied Electromagnetics*. 272 (Artech House, 2003).

# Chapter 2
# *Biological templates for self-assembly and the Tobacco Mosaic Virus coat protein*

This chapter details various methods of nanostructure fabrication through both top-down and bottom-up approaches. This is followed by a review of the use of biological templates for self-assembly with attention to proteins and DNA. Finally, the use of viruses in nanotechnology is introduced and the behavior and expression of the Tobacco Mosaic Virus coat protein is detailed.

## 2.1 Top-down, bottom-up

Methods for the fabrication of nanoscale structures can be generally categorized as either *top-down* or *bottom-up* depending on the initial state of the building materials. A top-down approach begins with a bulk material and sculpts the desired shape, whereas a bottom-up approach arranges pre-formed building blocks into a larger structure under the direction of a command surface or programmed moieties. Virtually all contemporary electronic and optical technologies are heavily reliant on top-down fabrication methods, as they provide highly reproducible results on a large scale. Unfortunately, the cost and time requirements of such technologies applied at the lower end of the nanometer scale become prohibitively large, and prohibitively long.

Bottom-up self-assembly is well situated to address many of the issues that top-down fabrication currently struggles with, however, before the 'what' and 'how' of self-assembly are discussed, some of the most prominent top-down methodologies will be described to better illustrate the problems that self-assembly methods may help to solve.

### 2.1.1 Lithography for nanostructure fabrication

Most top-down lithographic techniques involve the transfer of a desired geometric pattern onto a protective surface called a *resist* which covers the material to be shaped. The resist is patterned chemically using a mask. When the resist is rinsed with an etching agent, either the chemically unaltered areas (a *negative* resist) or the altered areas (a *positive* resist) are removed. Further treatment removes the parts of the material that are not protected by the patterned resist, resulting in the desired geometry[1] *(Figure 2.1)*.

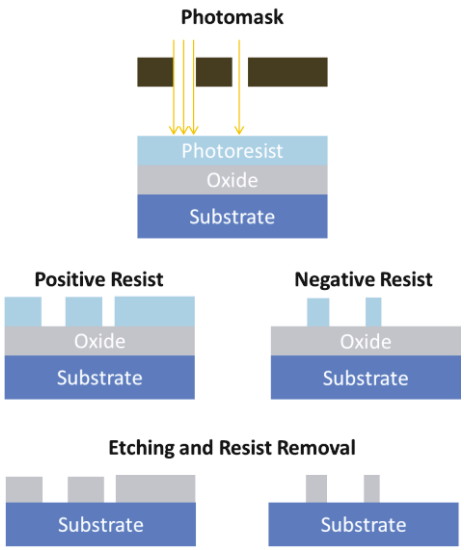


**Figure 2.1|** Generalized process flow for photolithography.

The most prominent micromachining technique in commercial use is *photolithography*. The resist in these systems is designed to react to light irradiation through a *photomask* that transfers the desired

pattern. Irradiated sections of the resist are then removed, exposing the material underneath for etching. This method has succeeded for large-scale applications due to its speed and low-cost, however, due to its dependence on light, it is subject to the diffraction limit. UV radiation allows feature sizes around 193 nm and a resolution enhancing technique called *high-index immersion lithography* has increased the resolution to 22 nm with the potential for greater enhancement. However, as the resolution increases, the process suffers unreproducible results and defect formation[2].

To avoid the diffraction limit of photons, electrons can be used to pattern the resist instead of light. This process, known as *electron beam lithography (EBL)*, utilizes a beam width on the order of nanometers[3]. Most research into metamaterials has been driven by EBL[4,5], however, it is a serial process – the resist is modified one 'pixel' at a time – and is, therefore, time consuming. The operating conditions of the electron beam also come at significant cost. These limitations have placed a practical upper limit on the total print size of approximately 100 $\mu m^2$, hindered this high-resolution technique from industry applications.

The slow processing time of EBL often leads to the use of *Focused-Ion Beam Milling (FIB)* for rapid prototyping to optimize a structure before fabrication using a technique such as EBL. FIB does not require a resist and uses a focused beam of gallium ions to sputter away atoms directly off the surface of the material, essentially carving a pattern into a predeposited layer[6]. FIB is limited to prototyping due to its relatively low resolution (~10 nm feature size) and the prevalence of gallium atoms in the finished product which causes alters electrical and optical material properties.

A method that approaches the rapid rate of FIB and, simultaneously, the high resolution of EBL is *Nano-Imprint Lithography (NIL)*. This process mechanically deforms a resist layer by using a stamp that is previously prepared by another printing technique. The use of a stamp allows for parallel processing and thus NIL is commercially viable. Fabrication of the stamp, however, can be very challenging since other lithographic methods are required and, therefore, NIL is rarely used for prototyping.

Many intriguing properties of metamaterials can only truly be realized in a three-dimensional system. For lithography, the most common methods used to achieve three-dimensional materials involve layer-by-layer techniques where planar structures are layered on top of one another[7–9]. Often such systems are limited by the thicknesses they can achieve and are mostly confined to periodic feature arrangements.

Lithography has dominated the fabrication of nanostructured components for decades, and researchers have worked hard to alleviate the shortcomings described above due to the absence of any other alternative. As human understanding of biological systems has increased over time, it has become apparent that the low-cost, parallel and efficient nature of bottom-up self-assembly systems may provide an alternate pathway in situations where lithographic methods are impractical.

### 2.1.2 Bottom-up self-assembly

*Self-assembly* is the spontaneous association of objects into defined shapes in specific conditions. Such systems, once assembled, exist at a thermodynamic equilibrium, with a higher level of order than the unassembled components. While human derived technology mostly depends on top-down fabrication techniques, self-assembly is the chief paradigm of almost all biological systems. With billions of years of natural selection, nature has mastered the implementation of function with the highest level of energy and mass efficiency. This remarkable achievement has inspired scientists to attempt to replicate such systems in the laboratory[10].

Self-assembled systems can be separated into two broad categories. The first involves *programed building blocks*, where the colloidal or molecular components possess some sort of functionality that complements other building blocks in the system, resulting in self-organization. Examples of such systems include the formation of micelles[11], microtubules[12] and the DNA double helix. The second category involves the organization of components onto a

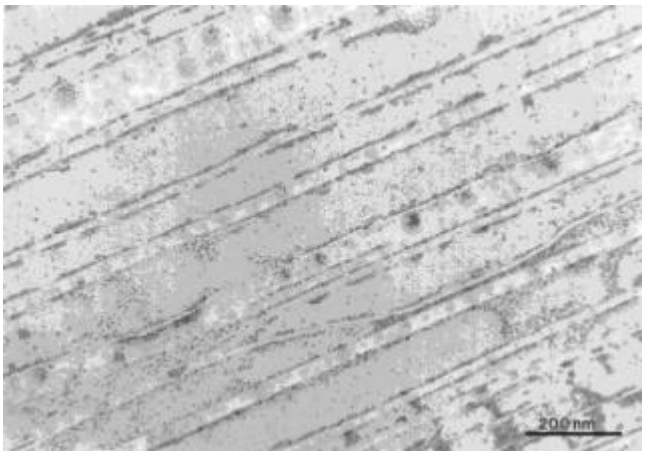


**Figure 2.2|** TEM image of lines of gold nanoparticles on carbon using a friction transferred poly(tetrafluoroethylene) template.[15] © 2001 Reprinted with permission from Wiley.

template or *command surface*. In this instance, the surface plays a central role in determining the final structure. There have been several studies utilizing synthetic templates to assemble colloids into geometrically precise arrangements such as the organization of polystyrene beads[13] or spherical block co-polymers[14] into two-dimensional arrays on a patterned photoresist and gold nanoparticles into parallel lines on carbon[15] *(Figure 2.2)*. In virtually all cases, synthetic templates limit the achievable complexity and dimensionality due to the reliance on top-down methodologies to produce them. These limitations have inspired many to utilize the ubiquitous structural motifs already present in natural materials. Biochemists have developed numerous techniques to modify existing systems and thus implement functionality that can direct self-assembly[16].

## 2.2 Biological templates for self-assembly

There are a wide variety of biologically sourced templates that have been explored in the literature, from whole organisms such as bacterial colonies[17], fungal colonies[18], and the silica cell walls of diatoms[19,20], down to individual proteins[21,22] and deoxyribonucleic acids (DNA)[23]. Proteins and DNA in particular are an intriguing set of materials to consider because they may inherently possess their own self-assembly dynamics. Multi-step assembly is required to impart hierarchal complexity in a nanostructured material[24]. Therefore, taking advantage of the intrinsic assembly behaviour of biomolecules may pave the way to more complex geometries that are currently inaccessible with synthetic templates.

### 2.2.1 DNA and protein templated self-assembly

Proteins and DNA as biological polymers are utilized quite differently. DNA consists of alternating phosphate and 2-deoxyribose sugar groups bound to a nucleobase. A monomer of

this chain is called a nucleotide. There are four variants depending on which nucleobase is bonded to the sugar moiety; adenine, cytosine, guanine or thymine. The principal interaction governing the self-assembly of DNA is hydrogen bonding. Adenine and thymine can form two intramolecular hydrogen bonds while cytosine and guanine can form three. The variation in hydrogen-bond capability leads to a thermodynamically driven recognition system called Watson-Crick base-paring whereby two DNA sequences prefer to interact such that adenine pairs with thymine and cytosine with guanine.

Using these simple rules, a magnificent variation of template geometries both two-dimensional[25–28] and three-dimensional[29–31] have been realized by a clever technique named *DNA origami* – a process where long DNA strands are folded in predetermined positions using shorter DNA strands called 'staple strands'[25]. The resulting folded structures can be used as templates for assembly of inorganic components by functionalizing them with complimentary DNA strands designed to bind to particular sites on the original template *(Figure 2.3)*. The versatility of DNA scaffolding derives itself from the fact that DNA can be used as both a programmable building block as well as a command surface and thus bridges both categories mentioned above. The predictable nature of Watson-Crick base pairing and the algorithmic nature of DNA sequence programming has led to the development of powerful software such as SARSE[32] that can design the necessary DNA strands required to assemble particular geometries.

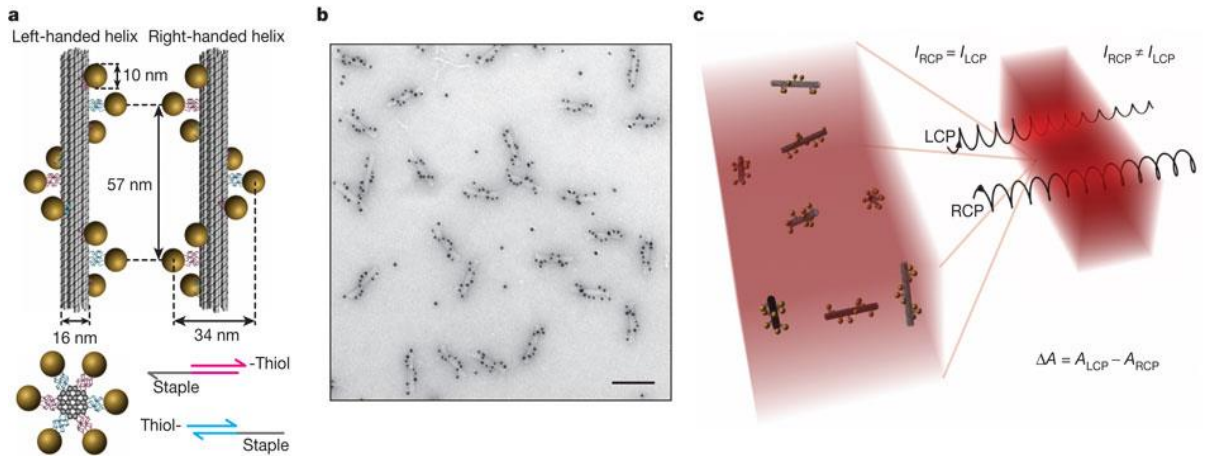


**Figure 2.3|** (a) Diagram of gold nanoparticle assembly onto columnar DNA scaffolding using complimentary 'staple' strands. (b) TEM image of chirally arranged nanoparticles based on scheme in (a). (c) Chirally arranged gold nanoparticles display circular dichroism.[29] © 2012 Reprinted with permission from Nature.

With such a powerful and versatile system in DNA it is not unreasonable to ask why one would endeavor to utilize the significantly more complex and less-understood protein biomolecules as templates. The 21 amino acids that natural proteins consist of possess several different chemical functionalities through their side groups both hydrophilic and hydrophobic. The complex interactions of these groups determine the shape and functionality of a protein as well as its intermolecular assembly properties. This chemical diversity makes elusive the pursuit of designing proteins with predetermined functionality, as one can with DNA, but simultaneously allows proteins to function as templates in a wider variety of conditions. Heavy utilization of ionic groups allows natural systems to survive extreme temperatures (such as the enzymes found in hyperthermophilic organisms[33]), while proteins that display a large number of acidic or basic groups on their solvent exposed surface have been observed in bacteria that survive harsh chemical environments[34]. In short, the larger chemical variability of amino acids, while hindering a full understanding of protein dynamics, imbues a greater degree functional plasticity for protein-based templates.

A subset of protein templates, viruses and their capsids, has recently garnered a great deal of attention due to their strict monodispersity, the wide variety of available geometries, and the ease by which they can be produced and manipulated using well established biochemical techniques.

### 2.2.2 An introduction to viruses

Viruses are macromolecule complexes that, through natural evolution, have developed a capacity to propagate themselves in a host cell by implementing the genetic information they enclose into the host cell's molecular manufacturing system. Historically, they have been considered a deleterious element of Earth's ecosystem by the disease and damage they have caused to humanity and human society. With the development of molecular biology and high resolution microscopy techniques such as Transmission Electron Microscopy (TEM) and Scanning Probe Microscopy (SPM), the mechanisms by which viruses function have been elucidated. It has become apparent that viruses are a marvel of biomolecular machinery. Revealing the relationships between their structure and function has aided biochemists in better understanding other biological systems and may perhaps open new frontiers in nanoscale engineering for material scientists.

The basic composition of a virus consists of a genetic sequence contained within one or more proteins called a *capsid* or *coat*. They may also be enveloped in a lipid bilayer and are thus classified as *enveloped* or *non-enveloped*[35]. The capsid plays a central role in the structure and function of the virus as a whole and is the focus of attention for material scientists. It is an association of protein subunits into a quaternary structure producing a hollow oligomer that houses the genetic information. The most common geometries are symmetrical helices or icosahedra. Icosahedral viruses often deviate from the ideal geometry of 60 subunits with 3 subunits on each face in order to enclose more genetic material.

As platforms for templated self-assembly, plant viruses have the advantage of having no pathogenicity towards humans and can often be utilized without their infectious genome. This is because most of the chemical functionality that assembles the capsid is incorporated into the proteins themselves. As a result, they can often assemble independently[36] or around a simulant of the genetic material such as a charged colloid[37] or polymer[38]. These *Virus-Like Particles* (VLPs) assemble into a variety of geometries and can also respond to chemical and physical changes in their environment such as pH and temperature.

### 2.2.3 Viruses and VLPs in nanotechnology

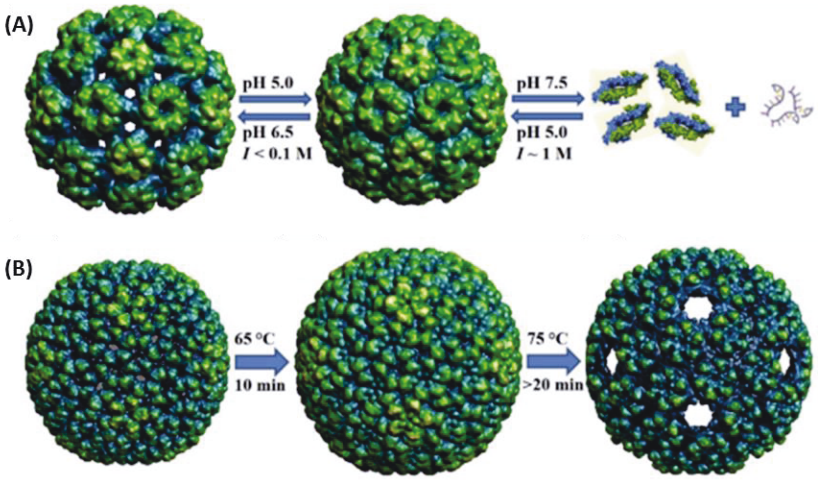


**Figure 2.4|** (A) CCMV structural transitions upon change in pH and ionic strength. (B) Bacteriophage P22 structural transitions upon change in temperature.[41] © 1995 Reprinted with permission from Elsevier.

Viruses and VLPs have been applied in several distinct ways for the fabrication of new nanomaterials. Perhaps the most obvious of which is the encapsulation of materials other than the original virus payload. Such endeavours utilize the functional component of a capsid to its fullest, often taking advantage of a capsid's preprogrammed assembly and disassembly mechanisms. The Cowpea chlorotic mottle virus (CCMV) has been used extensively in this manner. CCMV is a T=3 icosahedral virus with a capsid consisting of 180 identical coat protein subunits which – like many plant viruses – can be separated from the viral genome or expressed separately in yeast[39] or *E.coli*[40]. The CCMV capsid undergoes a reversible structural transition controlled by pH and ionic strength whereby the capsid swells as pH increases from 5.0 to 6.5 at low ionic strength. In the process it develops 60 perforations that are 2 nm in diameter. This reproducible change acts as a molecular gating mechanism, allowing ions and small molecules to diffuse in and out of its internal cavity and then preventing their escape when the process is reversed [41] *(Figure 2.4)*. The red clover necrotic mosaic virus (RCNMV) undergoes a similar mechanism in response to a decrease in divalent cation concentration[42] while bacteriophage P22 undergoes a comparable but irreversible transformation in response to heat[43]. These responses, originally evolved for the release of a viral payload once inside a target host, have been appropriated for the encapsulation of drug molecules for targeted drug delivery[44,45], or chromophores for *in vivo* imaging[46] and single molecule enzyme assays[47].

In a variation of this motif, some capsid subunits will encapsulate a large molecule or colloid as long as they fulfill electrostatic requirements dictated by the charge of the capsid interior. In such cases the amino acids that populate the interior of the capsid will possess a characteristic charge. CCMV, for example, has a positively charged interior and will assemble around negatively charged polyelectrolytes such as polyferrocenylsilane[38]. The encapsulated object may influence and alter the structure of the capsid itself. The brome mosaic virus (BMV) can encapsulate various sizes of gold nanoparticles but will appear in one of three different icosahedral forms depending on the nanoparticle diameter[37].

The utilization of capsids as scaffolds for templated self-assembly, in contrast to simple encapsulation, makes more extensive use of the particular chemical functionalities displayed on the capsid's inner and outer surfaces. These sites provide an opportunity to add addressable handles for the self-assembly of inorganic components, antibodies[48] and other molecules for applications in nanotechnology. There are generally two ways to introduce 'active sites' for self-assembly, mutation of the capsid's primary sequence, or chemical modification of the protein capsid itself. Mutation alters the genes encoding the expression of the virus capsid prior to its introduction into the system which produces the protein (the expression and harvesting of capsid proteins in will be discussed in Section 2.3)[49]. This can be an elaborate, time-consuming and costly process but is somewhat facilitated by numerous commercial kits that standardize the procedure. One is also limited to chemical moieties provided by the nature's library of amino acids. The key advantage of mutation, however, is the guarantee that every capsid protein will share the same mutation identically with 100% yield. Furthermore, once the mutated genes are produced, they can be propagated indefinitely at a significantly lower cost.

The complex self-assembly properties of protein capsids are derived from the rich variety of chemical groups such as carboxylates from aspartic (Asp) and glutamic (Glu) acid, amines from lysines (Lys) and phenols from tyrosine (Tyr) residues. In many cases, chemical modification of these groups does not compromise the structural integrity of the virus, and many bioconjugation protocols have been developed[16] for their orthogonal modification. Chemical methods have the advantage of being generally cheap to execute and a larger collection of chemical moieties are available. Unfortunately, it is difficult to achieve complete

functionalization of all capsids in solution and thus post-modification purification techniques are often necessary. Chemical modification of capsid proteins in the context of the Tobacco Mosaic Virus will be covered in detail in Chapter 4.

One of the earliest examples of virus-templated self-assembly utilized mutants of the Cowpea mosaic virus (CPMV), an icosahedral virus (T=3) consisting of 60 protein subunits with a spherically averaged diameter of 30 nm. Ratna et al.[50] utilize several mutants of CPMV where cysteine is introduced into different locations on the capsid surface. The thiol side-group of cysteine residues has a high affinity to gold nanoparticles and thus when the CPMV mutants are mixed with solutions of gold colloids, the nanoparticles assemble in geometric correspondence with the location of the cysteine mutation. These conjugates display optical properties associated with plasmonic coupling between adjacent particles[51]. Additionally, incorporation of conjugated oligomers such as oligophenylenevinylene[52] under the direction of the arranged nanoparticles has illustrated the utility of such a system for use in nanoscale sensing[53].

Components in virus templated systems need not be prefabricated. Often the surface charge characteristics of virus capsids result in an affinity for metal precursors such that one can achieve selective reduction and metal precipitation in predefined locations on the protein surface. This form of biotemplation is reminiscent of the spatially controlled biomineralization observed in biosilicifying organisms[54] and has been effective in the fabrication of nanowires[55] and the size-controlled crystallization of polyoxometalate minerals[56].

## 2.3 The Tobacco Mosaic virus

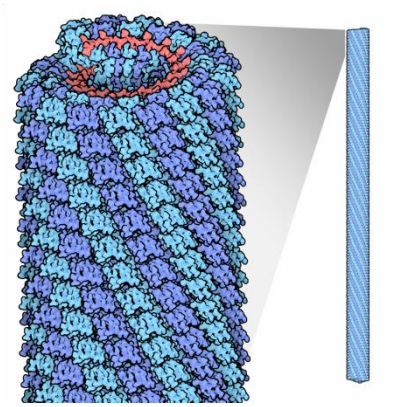

**Figure 2.5|** Cartoon depiction of TMV coat protein (blue) protecting RNA (red). © 2014 Reprinted with permission from David Goodsell & RCSB Protein.

The discovery of the Tobacco Mosaic Virus (TMV) can be attributed to Adolf Mayer, a chemist and microbiologist who first observed the disease that afflicted tobacco plants, resulting in lower growth yields and plant decay. Manifested as a discoloration of the leaves, Mayer coined the name Tobacco Mosaic to describe what was only understood as a non-bacterial infectious agent[57]. In 1898, Beijerinck confirmed the continued infectivity of TMV diseased plant extracts after filtration and concluded that this was indeed a new infectious agent, designating it as a virus[58]. The first purified and crystallized preparation of TMV was obtained by Stanley[59] and the concept of a virus as a nucleic acid sequence protected by a protein coat was shortly fully established by Bawden et al.[60] in 1936. The self-assembly properties of the TMV coat protein in the absence of the infectious RNA have been extensively characterized[61] and TMV is often cited as a paradigm for biological assembly[62]. Its relative simplicity of design and function as well as its remarkable stability has made it a model for biomolecular self-assembly and a popular substrate for material science.

TMV is a 300 nm rod-shaped virus with an 18 nm diameter and channel that runs through its central axis with a diameter of 4 nm. It is a helical arrangement of 2130, 17.5kDa identical protein subunits which pack the RNA between its turns *(Figure 2.5)*. When the RNA and coat protein are separated by chemical means[63], the protein capsid aggregates into several structures based on pH, ionic strength and temperature[64]. These aggregates play an important functional role in the assembly and disassembly of TMV and can be distinguished into three classes of structures that interconvert reversibly and are named by their sedimentation

coefficients; 4S *α-protein*, 20S *disk* and *helix (Figure 2.6)*. The a-protein is a mixture of small aggregates of protein subunits that occur at basic conditions. The helix, on the other hand, occurs at acidic pH and is a helical array of protein subunits forming a rod that resembles that of a complete TMV virus but with a polydispersity in length. The 20S disk is a two-layer aggregate consisting of 34 subunits with a diameter of 18 nm. It has a 17-fold symmetry and as with the helix it possesses a pore, 4 nm in diameter, at its center.

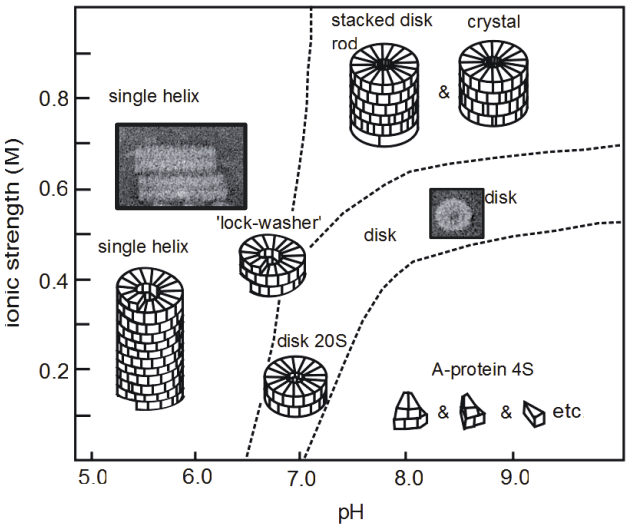


**Figure 2.6|** Pseudo-phase diagram of TMV coat protein assembly states with TEM images superimposed. Lines denote when each species becomes dominant in number. All three states exist in dynamic equilibrium.[62] © 2006 Reprinted with permission from Elsevier.

The 20S disk occurs at intermediate pH and ionic strength and has been closely scrutinized due to its role in the assembly of the complete virion. The disk has historically generated controversy among laboratories studying how TMV assembles *in vivo*[65]. It is now understood that the infectious RNA folds into a hair-pin loop that binds TMV coat protein through a sequence known as the 'origin of assembly'. This induces a conformational change that nucleates the growth of the full capsid[66,67]. The RNA is encapsulated by the coat proteins through an electrostatic attraction between negatively charged phosphate groups on the RNA and positively charged arginine side chains. The interaction is buttressed through hydrogen bonding to threonine residues. Despite this understanding, contention remains as to the

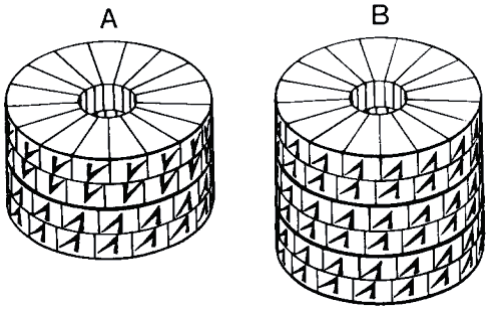


**Figure 2.7|** Possible packing arrangement of rings of TMV protein subunits. (A) Bipolar four-layer aggregate found in disk crystals. (B) Polar packing of subunits forming stacked disk observed in electron micrographs.[68] © 1990 Reprinted with permission from Elsevier.

structure of disk which nucleates TMV rod assembly. Studies involving monoclonal antibodies specific to one side of the coat protein subunit are shown to bind both ends of the disk and X-ray diffraction of crystallized TMV coat protein disks reveal a four layer bipolar arrangement[68] (*Figure 2.7(A)*). However, analyses utilizing electron microscopy suggest that the 20S disk exists as layers of 17 subunit rings in a polar (top to bottom) orientation[69–71] (*Figure 2.7(B)*). These studies have concurrently shown that the bipolar disk aggregate is incapable of nucleating rod assembly. Since the transition to helices does indeed occur, it may be the case that both polar and bipolar forms exist in solution.

### 2.3.1 Self-assembly of the Tobacco Mosaic Virus coat protein

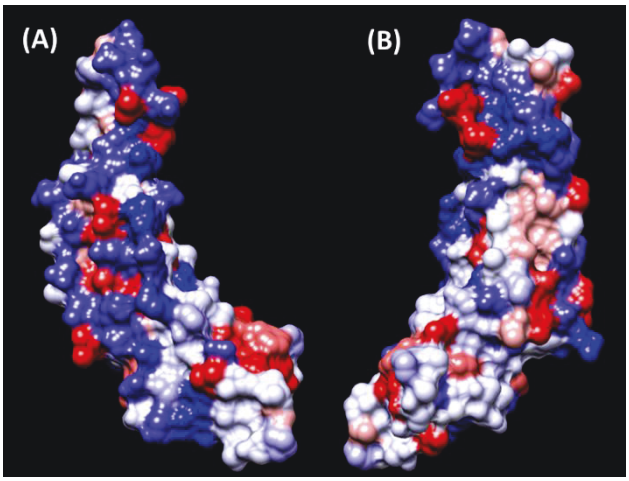


**Figure 2.8|** Top (A) and bottom (B) surface of TMV coat protein subunit colored from hydrophilic (blue), neutral (white) to hydrophobic (red) by the Kyte and Doolittle hydrophobicity scale[92]. Bottom surface displays more hydrophobic character and drives the formation of a two-layer disk by hydrophobic attraction. Similarly, hydrophobic groups on the side of the protein drive the assembly of the disk itself.

TMV coat proteins self-assemble into complex structures through an interplay of hydrophobic attraction, electrostatic repulsion and hydrogen-bonding. Scanning calorimetry investigations into the transition from a-protein to disks reveals that the process is endothermic and promoted by increasing temperature[72,73]. Kegel and van der Schoot[61] thus conclude that the 20S disk is formed by a hydrophobic interaction between protein subunits. This attractive force competes with a mutual electrostatic repulsion between individual subunits produced by the numerous negatively charged residues on the protein surface *(Figure 2.7)*. The distribution of charged residues on the protein is such that the sides of the protein have more hydrophobic character - which drives side-by-side aggregation into a disk.

As the ionic strength increases, the negative residues are screened and the Debye length decreases. This allows hydrophobic patches to approach and make contact, increase their interfacial free energy. If the pH is decreased then the number of negatively charged groups per subunit decreases by protonation, which promotes disk formation as fewer electrolytes are required to screen the electrostatic repulsion. The disk geometry is thus a consequence of the drive to maximize the contact area between hydrophobic regions on the sides of the coat protein.

The helical rod arrangement decreases the contact between hydrophobic surface groups and, therefore, cannot be explained by electrostatic screening. High resolution X-ray diffraction[74] has suggested that two pairs of carboxylate groups interact with one another in the helical state across protein subunits, Glu50 and Asp77 interact axially while Asp95 and Asp106 interact laterally. The importance of these residues in the helical polymerization of the protein subunits has been confirmed by site-directed mutagenesis where replacement of Asp and Glu with glutamine (Gln) and asparagine (Asn) impairs the capsid's helix assembly[75]. Finally, titration studies have revealed that at least one pair of these carboxylates is protonated upon decreasing the pH below an anomalous pKa of approximately 7.1[76]. The anomalously high pKa of the transition is due to the apolar, low-dielectric environment created by hydrophobic residues adjacent to the carboxylates on the protein[77].The protonation coincides with the first appearance of helically polymerized protein and it has thus been concluded that the helical geometry is a result of hydrogen bonding between the carboxylate pairs *(Figure 2.8)*. The directional nature of the hydrogen bond induces a 2.5° twist about the horizontal axis and a 4.5° twist about the radial axis. These *Caspar pairs* act as electrostatic switches in numerous viruses[78], triggered by the binding of protons or calcium ions and playing an important role in capsid disassembly. Upon invading a host cell, the lower proton and

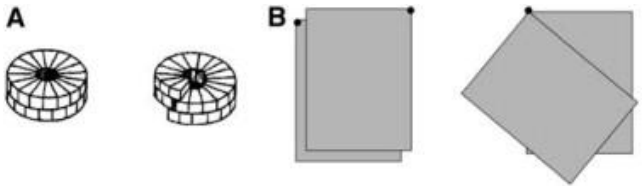


**Figure 2.9|** (A) Schematic drawing of a disk (left) and helix (right). Disk has larger area of contact for hydrophobic interaction but hydrogen bonding results in a twist (as represented in (B)) and helix formation.[61] © 2006 Reprinted with permission from Cell press.

calcium concentrations within the cell results in the dissociation of the Caspar pairs and a disassembly of the capsid, exposing the infectious RNA[68].

### 2.3.2 TMV and TMV capsids as templates for bottom-up self-assembly

Virtually all studies that have utilized TMV as a template for self-assembly have taken advantage of the complete virion or the helix form of the coat protein. Both the inner channel surface and the outer virion surface are hydrophilic, exposing glutamic and aspartic acids, arginines and lysines to the solvent. The functional groups within the inner channel are predominantly negative with pKa values within the carboxylate standard range of 1-3 or the anomalously high pKa discussed earlier between 6 and 8[79]. The outer surface of the virus, on the other hand, has numerous amines due to the N-termini of the protein subunits and arginine residues. Such groups have pKa values between 11 and 13. Mann and coworkers[80] took advantage of this differential to selectively complex and mineralize various metal salts[81]. By choosing an appropriate pH, one can alter the relative surface charge of the inner and outer surfaces. For example, at a pH of 3, the inner cavity is virtually neutral while the outer surface is positively charged, allowing the selective binding of anionic metal precursors like $AuCl_4^-$ or $PtCl_4^{2-}$. Upon reduction, only the outer surface of the virus is metallized[82]. On the other hand, above neutral pH, cationic metal precursors such as silver will selectively associate with the inner cavity and, when reduced, form size controlled nanoparticles with equal spacing. Using electroless deposition rather than direct chemical reduction has been observed to alter the morphology of the fabricated metal, resulting in continuous metal nanowires rather than nanoparticles[83,84].

The empty TMV capsid has not been utilized as frequently for metal nanoparticle templating. Instead, use of the coat protein in isolation often involves appropriating the natural self-assembly properties of the capsid to produce functional materials. Francis et al.[85] utilized a mutant of the TMV coat protein with a point mutation of Ser123 to Cys to create handles for the binding of thiol-reactive chromophores to the mutant. By exploiting the natural self-assembly mechanism of the capsid, they produced helical rods incorporating FRET donor and acceptor dyes that behaved as light-harvesting assemblies. Similarly, Endo et al. [86] bound

pyrene maleimide to a cysteine mutant of TMV to create conjugated pyrene stacks in the inner cavity that displayed electron transport.

Cysteine mutation is not the only popular method of TMV modification, for example, tyrosine residues on the surface of the TMV coat protein have been modified by electrophilic substitution with diazonium salts to introduce new functionalities such as alkynes[87]. Alkynes can be reacted with azide-functionalized molecules by the highly specific copper-catalyzed azide-alkyne cycloaddition (discussed in more detail in Chapter 6). This has enabled the conjugation of TMV with fluorogenic labels which only fluoresce upon conjugation at the locations of tyrosine residues[88].

The TMV rod itself has been utilized as a self-assembling constituent in numerous cases. An electrostatically driven head-to-tail assembly of TMV into composite fibers has been stimulated via the *in situ* polymerization of aniline[89]. TMV coat protein mutated with a hexahistidine tag at the C-terminus has been observed to assemble side-by-side through pi-stacking into long fibers or hexagonal disk arrays depending on the conditions of assembly[90].

### 2.3.3 Expression of the Tobacco Mosaic virus coat protein

There are two predominant methods to obtain TMV. The first method, *transgenesis*, involves the infection of tobacco plants with TMV by mechanical abrasion. The virus replicates in its natural host over a period of three to four weeks and is then harvested from ground plant tissue. The coat protein can be isolated through an acetic acid degradation procedure devised by Fraenkel-Conrat[63]. TMV can be isolated in excess of a gram per kilogram of plant leaves.

The second method, *heterologous expression*, utilizes the protein fabrication machinery of yeast or bacteria such as *Escherichia coli (E. coli*) to produce a desired protein. Expression yields the capsid protein in isolation and thus eliminates the need to handle infectious virus. In short, a gene coding for the coat protein is synthesized and inserted into to the structural section of a gene sequence called an *operon*. TMV coat protein is most often used in conjunction with the *lac operon*[91], a gene sequence normally used to control the production of enzymes involved in the digestion of lactose in *E. coli*. Upon exposure to increasing concentrations of lactose, the *lactose repressor* is unbound and the structural gene sequence is made available to T7 RNA

polymerase which transcribes the gene sequence into RNA for translation into proteins in ribosomes.

The customized genes are inserted into *E. coli* cells in the form of a single stranded circular DNA called a plasmid and a culture is then grown at physiological conditions in a broth containing required nutrients. Once an appropriately large population of cells have developed, lactose or lactose derivatives such as isopropyl-β-D-thio-galactoside (IPTG) are added to the cells, triggering the protein expression mechanisms. The cells are allowed to produce the protein for a predetermined amount of time before they are lysed and the protein is harvested. While yields are generally inferior by this method, the process is much faster and the failure rate much lower.

## 2.4 Summary

In summary, top-down lithographic approaches meet significant challenges at feature lengths below 50 nm. Bottom-up templated self-assembly utilizing biologically sourced templates may provide a means to produce complex three-dimensional structures at the nanoscale. Virus capsids are a promising example of such templates due to their monodispersity, stability and ease of manipulation. Of relevance to this thesis is the Tobacco Mosaic Virus, a helical virus with a coat protein that has its own system of self-assembly and can provide helical and disk shaped templates depending on pH, temperature and ionic strength.

## Citations


1. P. Rai-Choudhury. *Handbook of Microlithography, Micromachining, and Microfabrication: Microlithography*. 776 (IET, 1997).

2. Wei, Y. & Brainard, R. L. *Advanced Processes for 193-nm Immersion Lithography*. 315 (SPIE Press, 2009). at <http://books.google.com/books?id=Sx39H8XR1FcC&pgis=1>

3. Boltasseva, A. & Shalaev, V. M. Fabrication of optical negative-index metamaterials: Recent advances and outlook. *Metamaterials* **2,** 1–17 (2008).

4. Dolling, G., Enkrich, C., Wegener, M., Soukoulis, C. M. & Linden, S. Simultaneous negative phase and group velocity of light in a metamaterial. *Science* **312,** 892–4 (2006).

5. García-Meca, C., Ortuño, R., Salvador, R., Martínez, A. & Martí, J. Low-loss single-layer metamaterial with negative index of refraction at visible wavelengths. *Opt. Express* **15,** 9320–9325 (2007).

6. Cai, W. & Shalaev, V. *Optical Metamaterials*. (Springer New York, 2010). doi:10.1007/978-1-4419-1151-3

7. Dolling, G., Wegener, M. & Linden, S. Realization of a three-functional-layer negative-index photonic metamaterial. *Opt. Lett.* **32,** 551 (2007).

8. Morita, T. *et al.* Nanomechanical switch fabrication by focused-ion-beam chemical vapor deposition. *J. Vac. Sci. Technol. B Microelectron. Nanom. Struct.* **22,** 3137 (2004).

9. Valentine, J. *et al.* Three-dimensional optical metamaterial with a negative refractive index. *Nature* **455,** 376–9 (2008).

10. Mann, S. On the nature of boundary-organized biomineralization (BOB). *J. Inorg. Biochem.* **28,** 363–371 (1986).

11. Chayen, J. Micelles, monolayers and biomembranes. M. N. Jones and D. Chapman. Wiley–Liss, New York and Chichester. xii + 252 pages, £36.75 (1995). *Cell Biochem. Funct.* **14,** 75–75 (1996).

12. KIRSCHNER, M. Beyond self-assembly: From microtubules to morphogenesis. *Cell* **45,** 329–342 (1986).

13. Yin, Y., Lu, Y., Gates, B. & Xia, Y. Template-Assisted Self-Assembly: A Practical Route to Complex Aggregates of Monodispersed Colloids with Well-Defined Sizes, Shapes, and Structures. *J. Am. Chem. Soc.* **123,** 8718–8729 (2001).

14. Bita, I. *et al.* Graphoepitaxy of self-assembled block copolymers on two-dimensional periodic patterned templates. *Science* **321,** 939–43 (2008).

15. Hutchinson, T. O., Liu, Y.-P., Kiely, C., Kiely, C. J. & Brust, M. Templated Gold Nanowire Self-Assembly on Carbon Substrates. *Adv. Mater.* **13,** 1800–1803 (2001).

16. Hermanson, G. T. *Bioconjugate Techniques*. 1323 (Academic Press, 2010).

17. Davis, S. A., Burkett, S. L., Mendelson, N. H. & Mann, S. Bacterial templating of ordered macrostructures in silica and silica-surfactant mesophases. *Nature* **385,** 420–423 (1997).

18. Li, Z., Chung, S.-W., Nam, J.-M., Ginger, D. S. & Mirkin, C. A. Living templates for the hierarchical assembly of gold nanoparticles. *Angew. Chem. Int. Ed. Engl.* **42,** 2306–9 (2003).

19. Andrews, M. P. *et al.* Nanoplasmonic photonic crystal diatoms and phytoliths. in *SPIE OPTO* (Adibi, A., Lin, S.-Y. & Scherer, A.) 79461S–79461S–12 (International Society for Optics and Photonics, 2011). doi:10.1117/12.881467

20. Bao, Z., Ernst, E. M., Yoo, S. & Sandhage, K. H. Syntheses of Porous Self-Supporting Metal-Nanoparticle Assemblies with 3D Morphologies Inherited from Biosilica Templates (Diatom Frustules). *Adv. Mater.* **21,** 474–478 (2009).

21. Hu, M., Qian, L., Briñas, R. P., Lymar, E. S. & Hainfeld, J. F. Assembly of nanoparticle-protein binding complexes: from monomers to ordered arrays. *Angew. Chem. Int. Ed. Engl.* **46,** 5111–4 (2007).

22. McMillan, R. A. *et al.* Ordered nanoparticle arrays formed on engineered chaperonin protein templates. *Nat. Mater.* **1,** 247–52 (2002).

23. Le, J. D. *et al.* DNA-Templated Self-Assembly of Metallic Nanocomponent Arrays on a Surface. *Nano Lett.* **4,** 2343–2347 (2004).

24. Lee, Y. S. *Self-assembly and nanotechnology*. *1996 Symp. Smart …* (John Wiley & Sons, Inc., 2008).

25. Rothemund, P. W. K. Folding DNA to create nanoscale shapes and patterns. *Nature* **440,** 297–302 (2006).

26. Geng, Y. *et al.* Electrically conductive gold- and copper-metallized DNA origami nanostructures. *Langmuir* **29,** 3482–90 (2013).

27. Sharma, J., Chhabra, R., Liu, Y., Ke, Y. & Yan, H. DNA-templated self-assembly of two-dimensional and periodical gold nanoparticle arrays. *Angew. Chem. Int. Ed. Engl.* **45,** 730–5 (2006).

28. Fan, Z., Zhang, H. & Govorov, A. O. Optical Properties of Chiral Plasmonic Tetramers: Circular Dichroism and Multipole Effects. *J. Phys. Chem. C* **117,** 14770–14777 (2013).

29. Kuzyk, A. *et al.* DNA-based self-assembly of chiral plasmonic nanostructures with tailored optical response. *Nature* **483,** 311–4 (2012).

30. Zhang, C. *et al.* DNA nanocages swallow gold nanoparticles (AuNPs) to form AuNP@DNA cage core-shell structures. *ACS Nano* **8,** 1130–5 (2014).

31. Tørring, T., Voigt, N. V, Nangreave, J., Yan, H. & Gothelf, K. V. DNA origami: a quantum leap for self-assembly of complex structures. *Chem. Soc. Rev.* **40,** 5636–46 (2011).

32. Andersen, E. S. *et al.* DNA origami design of dolphin-shaped structures with flexible tails. *ACS Nano* **2,** 1213–8 (2008).

33. Vetriani, C. *et al.* Protein thermostability above 100 C: A key role for ionic interactions. *Proc. Natl. Acad. Sci.* **95,** 12300–12305 (1998).

34. Menzel, U. & Gottschalk, G. The internal pH of Acetobacterium wieringae and Acetobacter aceti during growth and production of acetic acid. *Arch. Microbiol.* **143,** 47–51 (1985).

35. Mateu, M. G. *Structure and Physics of Viruses*. **68,** (Springer Netherlands, 2013).

36. Lavelle, L., Michel, J.-P. & Gingery, M. The disassembly, reassembly and stability of CCMV protein capsids. *J. Virol. Methods* **146,** 311–6 (2007).

37. Sun, J. *et al.* Core-controlled polymorphism in virus-like particles. *Proc. …* **104,** 1354–9 (2007).

38. Minten, I. J. *et al.* CCMV capsid formation induced by a functional negatively charged polymer. *Org. Biomol. Chem.* **7,** 4685–8 (2009).

39. Brumfield, S. *et al.* Heterologous expression of the modified coat protein of Cowpea chlorotic mottle bromovirus results in the assembly of protein cages with altered architectures and function. *J. Gen. Virol.* **85,** 1049–53 (2004).

40. Zhao, X., Fox, J. M., Olson, N. H., Baker, T. S. & Young, M. J. In vitro assembly of cowpea chlorotic mottle virus from coat protein expressed in Escherichia coli and in vitro-transcribed viral cDNA. *Virology* **207,** 486–94 (1995).

41. Wu, Y., Yang, H. & Shin, H.-J. Viruses as self-assembled nanocontainers for encapsulation of functional cargoes. *Korean J. Chem. Eng.* **30,** 1359–1367 (2013).

42. Sherman, M. B. *et al.* Removal of divalent cations induces structural transitions in red clover necrotic mosaic virus, revealing a potential mechanism for RNA release. *J. Virol.* **80,** 10395–406 (2006).

43. Teschke, C. M., McGough, A. & Thuman-Commike, P. A. Penton release from P22 heat-expanded capsids suggests importance of stabilizing penton-hexon interactions during capsid maturation. *Biophys. J.* **84,** 2585–92 (2003).

44. Ma, Y., Nolte, R. J. M. & Cornelissen, J. J. L. M. Virus-based nanocarriers for drug delivery. *Adv. Drug Deliv. Rev.* **64,** 811–25 (2012).

45. Li, J., Fan, C., Pei, H., Shi, J. & Huang, Q. Smart drug delivery nanocarriers with self-assembled DNA nanostructures. *Adv. Mater.* **25,** 4386–96 (2013).

46. Jung, B., Rao, A. L. N. & Anvari, B. Optical nano-constructs composed of genome-depleted brome mosaic virus doped with a near infrared chromophore for potential biomedical applications. *ACS Nano* **5,** 1243–52 (2011).

47. Glasgow, J. E., Capehart, S. L., Francis, M. B. & Tullman-Ercek, D. Osmolyte-mediated encapsulation of proteins inside MS2 viral capsids. *ACS Nano* **6,** 8658–64 (2012).

48. Sapsford, K. E. *et al.* A cowpea mosaic virus nanoscaffold for multiplexed antibody conjugation: application as an immunoassay tracer. *Biosens. Bioelectron.* **21,** 1668–73 (2006).

49. Dieckman, L., Gu, M., Stols, L., Donnelly, M. I. & Collart, F. R. High throughput methods for gene cloning and expression. *Protein Expr. Purif.* **25,** 1–7 (2002).

50. Blum, A. S. *et al.* Cowpea Mosaic Virus as a Scaffold for 3-D Patterning of Gold Nanoparticles. *Nano Lett.* **4,** 867–870 (2004).

51. Fontana, J. *et al.* Virus-Templated Plasmonic Nanoclusters with Icosahedral Symmetry via Directed Self-Assembly. *Small* 1–6 (2014). doi:10.1002/smll.201400470

52. Blum, A. S. *et al.* An engineered virus as a scaffold for three-dimensional self-assembly on the nanoscale. *Small* **1,** 702–6 (2005).

53. Blum, A. S. *et al.* Molecular electronics based nanosensors on a viral scaffold. *Biosens. Bioelectron.* **26,** 2852–7 (2011).

54. Nudelman, F. & Sommerdijk, N. a. J. M. Biomineralization as an Inspiration for Materials Chemistry. *Angew. Chemie Int. Ed.* n/a–n/a (2012). doi:10.1002/anie.201106715

55. Oh, D. *et al.* M13 virus-directed synthesis of nanostructured metal oxides for lithium-oxygen batteries. *Nano Lett.* **14,** 4837–45 (2014).

56. Douglas, T. & Young, M. Host-guest encapsulation of materials by assembled virus protein cages. **393,** 152–155 (1998).

57. A., M. Über die Mosaikkrankheit of Tabaks. *die-landwirtschaftlichen Versuchs Station.* 451–467 (1886).

58. Beijerinck, M. W. in *Phytopathol. Class.* (Johnson, J.) **7,** 33–52 (Americal Phytopathological Society, 1898).

59. Stanley, W. M. ISOLATION OF A CRYSTALLINE PROTEIN POSSESSING THE PROPERTIES OF TOBACCO-MOSAIC VIRUS. *Science* **81,** 644–5 (1935).

60. Bawden, F. C., Pirie, N. W., Bernal, J. D. & Fankuchen, I. Liquid crystalline substances from virus-infected plants. *Nature* **138,** 1051–1052 (1936).

61. Kegel, W. K. & van der Schoot, P. Physical regulation of the self-assembly of tobacco mosaic virus coat protein. *Biophys. J.* **91,** 1501–12 (2006).

62. Klug, a. The tobacco mosaic virus particle: structure and assembly. *Philos. Trans. R. Soc. Lond. B. Biol. Sci.* **354,** 531–5 (1999).

63. Fraenkel-Conrat, H. Degradation of tobacco mosaic virus with acetic acid. *Virology* **4,** 1–4 (1957).

64. Mandelkow, E., Holmes, K. C. & Gallwitz, U. A new helical aggregate of tobacco mosaic virus protein. *J. Mol. Biol.* **102,** 265–85 (1976).

65. Schuster, T., Scheele, R. & Khairallah, L. Mechanism of self-assembly of tobacco mosaic virus protein: I. Nucleation-controlled kinetics of polymerization. *J. Mol. Biol.* (1979).

66. Turner, D. R. & Butler, P. J. Essential features of the assembly origin of tobacco mosaic virus RNA as studied by directed mutagenesis. *Nucleic Acids Res.* **14,** 9229–42 (1986).

67. Butler, P. J. G. Assembly of Tobacco Mosaic Virus. *Philos. Trans. R. Soc. B Biol. Sci.* **276,** 151–163 (1976).

68. Caspar, D. L. D. & Keiichi Namba. Switching in the self-assembly of tobacco mosaic virus. *Adv. Biophys.* **26,** 157–185 (1990).

69. Finch, J. T., Leberman, R., Yu-Shang, C. & Klug, A. Rotational Symmetry of the Two Turn Disk Aggregate of Tobacco Mosaic Virus Protein. *Nature* **212,** 349–350 (1966).

70. Finch, J. T. & Klug, A. Three-Dimensional Reconstruction of the Stacked-Disk Aggregate of Tobacco Mosaic Virus Protein from Electron Micrographs. *Philos. Trans. R. Soc. B Biol. Sci.* **261,** 211–219 (1971).

71. Durham, A. C. H. & Finch, J. T. Structures and roles of the polymorphic forms of tobacco mosaic virus protein. *J. Mol. Biol.* **67,** 307–314 (1972).

72. Sturtevant, J. M., Velicelebi, G., Jaenicke, R. & Lauffer, M. a. Scanning calorimetric investigation of the polymerization of the coat protein of tobacco mosaic virus. *Biochemistry* **20,** 3792–800 (1981).

73. Kegel, W. K. & Schoot Pv, P. van der. Competing hydrophobic and screened-coulomb interactions in hepatitis B virus capsid assembly. *Biophys. J.* **86,** 3905–13 (2004).

74. Namba, K. & Stubbs, G. Structure of tobacco mosaic virus at 3.6 A resolution: implications for assembly. *Science* **231,** 1401–6 (1986).

75. Culver, J. N., Dawson, W. O., Plonk, K. & Stubbs, G. Site-directed mutagenesis confirms the involvement of carboxylate groups in the disassembly of tobacco mosaic virus. *Virology* **206,** 724–30 (1995).

76. Butler, P. J. G. Structures and roles of the polymorphic forms of tobacco mosaic virus protein. *J. Mol. Biol.* **72,** 25–35 (1972).

77. Lau, W. L., Degrado, W. F. & Roder, H. The effects of pK(a) tuning on the thermodynamics and kinetics of folding: design of a solvent-shielded carboxylate pair at the a-position of a coiled-coil. *Biophys. J.* **99,** 2299–308 (2010).

78. Wang, H., Planchart, a & Stubbs, G. Caspar carboxylates: the structural basis of tobamovirus disassembly. *Biophys. J.* **74,** 633–8 (1998).

79. Lu, B., Stubbs, G. & Culver, J. N. Carboxylate interactions involved in the disassembly of tobacco mosaic tobamovirus. *Virology* **225,** 11–20 (1996).

80. Dujardin, E., Peet, C., Stubbs, G., Culver, J. N. & Mann, S. Organization of Metallic Nanoparticles Using Tobacco Mosaic Virus Templates. *Nano Lett.* **3,** 413–417 (2003).

81. Lim, J.-S. *et al.* Quantitative study of Au(III) and Pd(II) ion biosorption on genetically engineered Tobacco mosaic virus. *J. Colloid Interface Sci.* **342,** 455–61 (2010).

82. Górzny, M. Ł., Walton, A. S. & Evans, S. D. Synthesis of High-Surface-Area Platinum Nanotubes Using a Viral Template. *Adv. Funct. Mater.* **20,** 1295–1300 (2010).

83. Balci, S. *et al.* Copper nanowires within the central channel of tobacco mosaic virus particles. *Electrochim. Acta* **51,** 6251–6257 (2006).

84. Tsukamoto, R., Muraoka, M., Seki, M., Tabata, H. & Yamashita, I. Synthesis of CoPt and FePt 3 Nanowires Using the Central Channel of Tobacco Mosaic Virus as a Biotemplate. *Chem. Mater.* **19,** 2389–2391 (2007).

85. Miller, R. a, Presley, A. D. & Francis, M. B. Self-assembling light-harvesting systems from synthetically modified tobacco mosaic virus coat proteins. *J. Am. Chem. Soc.* **129,** 3104–9 (2007).

86. Endo, M., Wang, H., Fujitsuka, M. & Majima, T. Pyrene-stacked nanostructures constructed in the recombinant tobacco mosaic virus rod scaffold. *Chemistry* **12,** 3735–40 (2006).

87. Bruckman, M. a *et al.* Surface modification of tobacco mosaic virus with “click” chemistry. *Chembiochem* **9,** 519–23 (2008).

88. Le Droumaguet, C., Wang, C. & Wang, Q. Fluorogenic click reaction. *Chem. Soc. Rev.* **39,** 1233–9 (2010).

89. Niu, Z. *et al.* Study and characterization of tobacco mosaic virus head-to-tail assembly assisted by aniline polymerization. *Chem. Commun. (Camb).* 3019–21 (2006). doi:10.1039/b603780a

90. Bruckman, M. a *et al.* Role of hexahistidine in directed nanoassemblies of tobacco mosaic virus coat protein. *ACS Nano* **5,** 1606–16 (2011).

91. Hwang, D. J., Roberts, I. M. & Wilson, T. M. Expression of tobacco mosaic virus coat protein and assembly of pseudovirus particles in Escherichia coli. *Proc. Natl. Acad. Sci. U. S. A.* **91,** 9067–71 (1994).

92. Kyte, J. & Doolittle, R. F. A simple method for displaying the hydropathic character of a protein. *J. Mol. Biol.* **157,** 105–32 (1982).

# Chapter 3
# *Gold nanoparticle rings on Tobacco Mosaic Virus coat protein disks by intermolecular interaction*


Abstract

Gold nanoparticle rings are fabricated by directed assembly on to Tobacco Mosaic Virus coat protein disks. Guanidinium side groups on arginine residues behave as hydrogen-bond donors to sulfonate oxygens on bis(p-sulfonatophenyl)phenylphosphine functionalized gold nanoparticles. A similar interaction results in the binding of a gold nanoparticle in the center of the rings. The population of rings with a central nanoparticle can be regulated by modifying the pH of the solution.

*This chapter is based on the paper "Solution Phase Gold Nanorings on a Viral Protein Template" published in Nano Letters, 2012, 12 (2), pp 629-633. This author and Amy Blum are the sole contributors to this work.*

## 3.1 Introduction

There are numerous chemical handles that can be addressed on protein molecules such as amines and carboxylic acids, however, in many cases these moieties are so numerous that selective targeting of specific residues is virtually impossible. *Site directed mutagenesis* is commonly utilized in these cases to introduce a cysteine residue at a desired location. Despite the fact that the sulfhydryl side group of cysteine residues is relatively polar, in native proteins they most frequently appear among hydrophobic residues and are thus often solvent inaccessible[1]. This implies that one can often be confident that a cysteine mutation can be specifically targeted without collateral modification. Blum et al.[2] have thus successfully assembled virus- gold nanoparticle conjugates in various geometries using three different mutants of the Cowpea Mosaic Virus. Similarly, Miller et al.[3] have displayed the effectiveness of this approach to incorporate maleimide functionalized chromophores exclusively at the 123 position of TMV coat protein. With the generous donation of the plasmid for the 123 cysteine mutant (S123C) of TMV coat protein by the Francis group, we have attempted to bind citrate and bis(p-sulfonatophenyl)phenylphosphine (BSPP) particles. This method has proved largely unsuccessful for reasons that are detailed in the next section.

While there are a great deal of examples of successful use of site directed mutagenesis, it can be quite laborious to design and express a successful mutation. The state of protein fold modelling is still relatively immature, such that one cannot predict with accuracy whether a chosen mutant will still be able to function until it has been tested experimentally. For this reason, we hoped to find another mechanism by which to assemble our nanoparticles into the desired ring structure. The choice of using TMV coat protein proved fortuitous in this instance. Unlike many proteins it possesses few solvent-exposed amines. Indeed, the only exposed amines in the 20S disk structure are two guanidinium-possessing arginine residues on the upper and lower faces of the disk (*Figure 3.6*), and the N-terminus primary amine on the side of each

capsid. We determined that BSPP-stabilized gold nanoparticles are driven to assemble onto the arginine residues, resulting in 22 nm gold nanoparticle rings. The interaction appears to be driven by an electrostatic attraction between negatively charged sulfonate groups on the BSPP ligand and the positive guanidinium moieties on arginine, however, we suspect that an additional hydrogen-bonding interaction between these two groups is also responsible for the relative geometric precision of the interaction. Additionally, we have found that a nanoparticle can be bound in the center of the ring due to a similar group of arginine residues around the 20S disk pore. This interaction is pH dependent, as the adjacent Caspair pair carboxylate groups have a pKa of 7.2[4], and can thus be protonated and deprotonated in the stability range of the 20S structure, inhibiting or allowing nanoparticle binding. We have published these findings previously[5]. Some sections of that publication shall be excerpted here.

### 3.2 Site directed mutagenesis for templated ring assembly

We have attempted to utilize the same S123C mutation that the Francis group developed with the expectation that the thiol groups located on the surface of the disk (approximately 11 nm

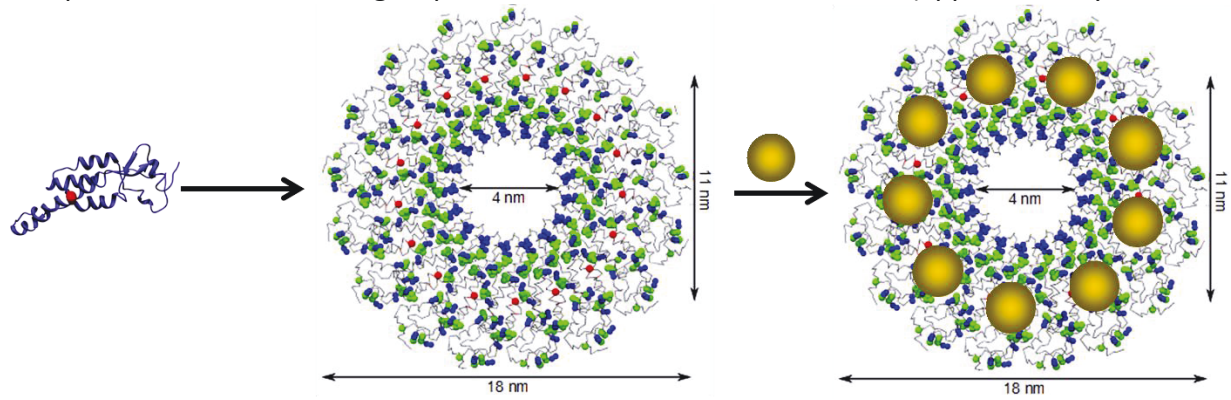


**Figure 3.1|** Schematic of assembly of gold nanoparticles on S123C mutation of TMV 20S disk. Green colored residues are amines while blue colored residues are carboxylic acids. The red colored residues indicate the S123C cysteine mutation.

from the center) would act as sites for gold nanoparticle binding *(Figure 3.1)*. The nanoparticles used were synthesized by a simple reduction of chloroauric acid with sodium borohydride in the presence of sodium citrate as a stabilizer.

Unfortunately, our attempts were largely unsuccessful. The reasons for this is that the cysteine mutation is relatively buried and sterically inaccessible, and is thus incapable of binding large

molecules and particles. It seems possible that if nanoparticles with longer ligands terminated in thiol-reactive groups such as maleimides are utilized, this problem may be circumvented. In the meantime, we decided to explore other methods of attachment.

### 3.3 Synthesis of BSPP-passivated gold nanoparticles

The ionic strengths required to stabilize the protein scaffold are such that citrate stabilized nanoparticles will flocculate. It was also predicted that these nanoparticles would not be stable to subsequent purification steps to separate rings from the free nanoparticles. Bis(p-sulfonatophenyl)phenyl phosphine *(Figure 3.2)* has become a popular ligand for the stabilization of aqueous gold nanoparticles – particularly in DNA self-assembly[6,7] - due to the significant stability to ionic strength it confers while remaining labile enough for displacement by thiols. Indeed, McMillan et al. have used BSPP ligands to assemble gold nanoparticles on to two-dimensional crystals of cysteine mutant chaperonin proteins to form highly organized arrays[8].

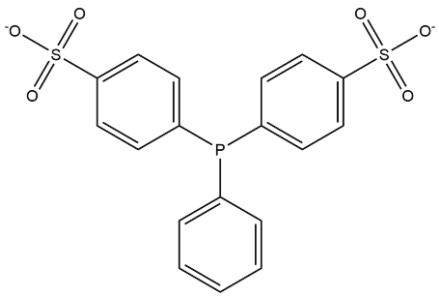

**Figure 3.2|** Structure of Bis(p-sulfonatophenyl)phenylphosphine.

BSPP has also received attention among organic chemists as an effective ligand for Suzuki-Miyaura coupling reactions[9]. BSPP complexes with metal ions in a +1 coordinate state[10] and can behave as a redox reagent in the conversion of $Au^0$ to $Au^+$. This implies that the resultant size of the nanoparticles is affected by the concentration of BSPP in solution. Since uncomplexed BSPP is prone to oxidation in water, the equilibrium size of BSPP-stabilized nanoparticles is dependent both on the initial BSPP concentration and on conditions that would influence the oxidation rate of BSPP such as temperature and oxygen concentration. This property has been utilized to produce hollow platinum nanoshells by initially synthesizing silver-platinum core-shells and then chemically oxidizing the core to $Ag^+$ with high concentrations of BSPP[11].

The strong association of BSPP with metal ions is advantageous for our system for two reasons; firstly, the exceedingly low pKa of the para-sulfonate groups ensures that the ligand displays a strong negative charge on the surface of the nanoparticle, resulting in a powerful inter-particle

repulsion. This enables their use in the relatively high salt concentrations required by biological materials. Secondly, if precipitated using ethanol or exceedingly high concentrations of salt, BSPP-stabilized gold particles (BSPP-Au NPs) are easily resuspended without loss of quality[12]. This provides a method to disperse the nanoparticles at a high particle concentration to encourage self-assembly without diluting the TMV scaffold, since we have observed a minimum concentration required for 20S disk assembly of approximately 11 µM in the wild-type TMV coat protein.

The BSPP-Au NPs synthesized for all our studies are between 3.5-5.0 nm in diameter and are stable for at least three months when stored at 4°C *(Figure 3.3)*.

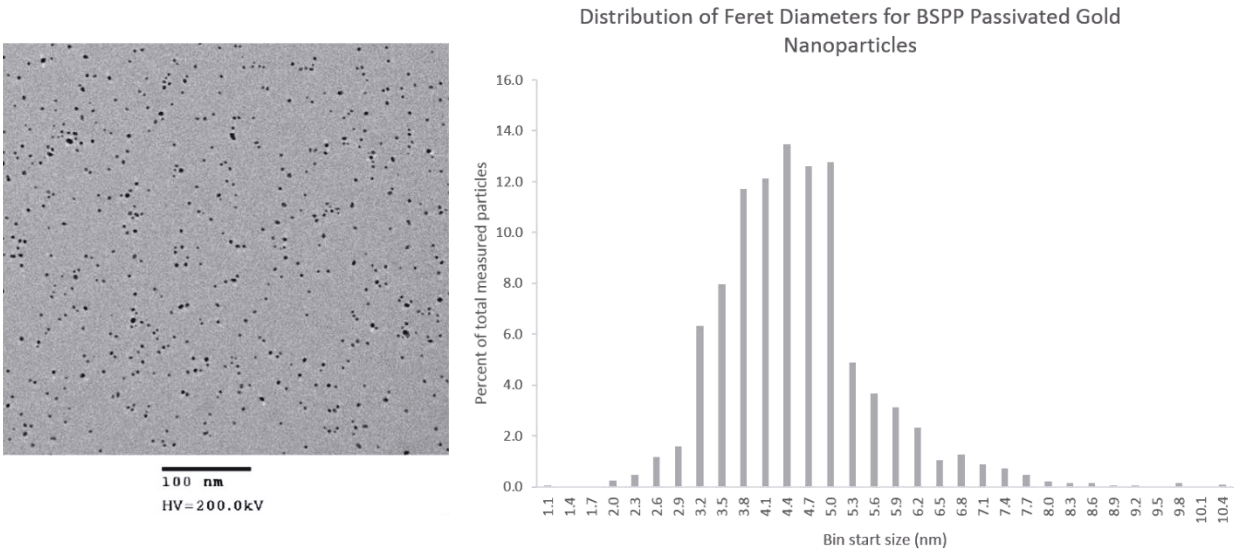


**Figure 3.3|** Particle analysis of BSPP-functionalized gold nanoparticles.

## 3.4 Assembly of nanoparticle rings

BSPP-Au nanoparticles are concentrated with spin filtration and then added to a buffered solution of TMVcp at various pH conditions between 5.5 and 7.5. Buffer concentrations were set so that the ionic strength was constant across the different conditions. A noticeably good yield of complete rings is obtained after a five day incubation period at room temperature. An analysis of the TEM images shows that ring diameter, inter-particle distance and the number of particles per ring do not change as the pH is varied. The ring diameter is 22.0 ± 2.2 nm. The invariance of ring dimensions across conditions indicates that the groups involved in binding

the nanoparticles are not significantly influenced by pH. An example set of TEM images is shown in *Figure 3.4*, a summary at each pH condition is illustrated in *Figure 3.5*.

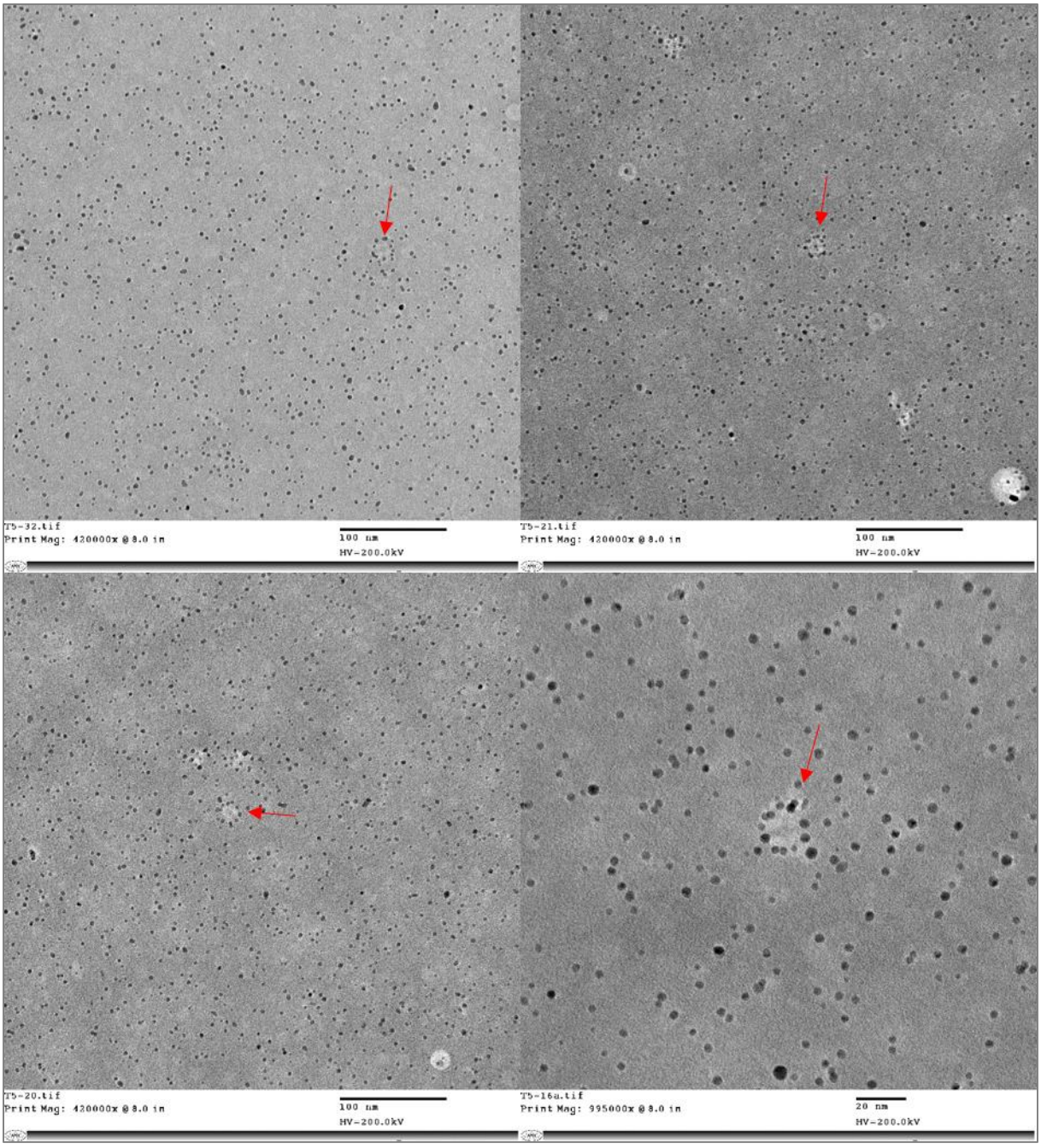


**Figure 3.4|** TEM images showing the contents of the assembly solution after incubating for five days. Red arrows indicate gold nanorings.

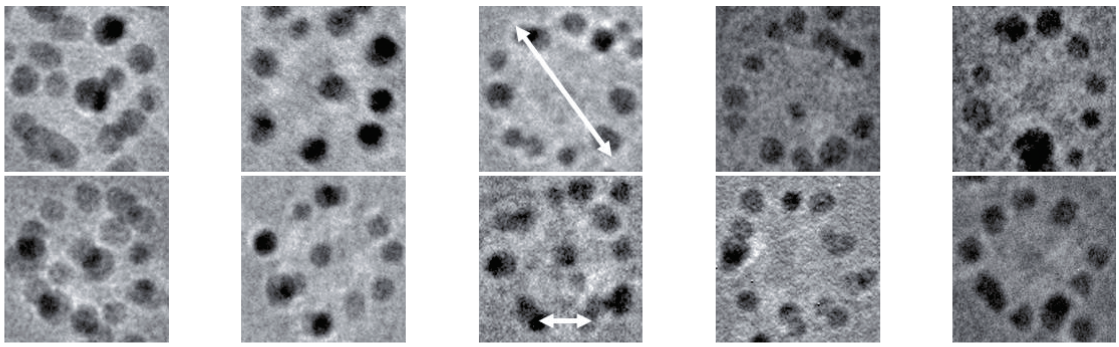

| pH | 5.5 | 6.0 | 6.5 | 7.0 | 7.5 |
|---|---|---|---|---|---|
| Central NP | 95% | 74% | 54% | 52% | 20% |

**Figure 3.5|** Summary of assembled nanoparticle rings along with the ratio of rings containing a central nanoparticle at each pH condition.

An average of ten nanoparticles are observed binding with their centers on the top-face edge of the TMVcp disks. This is confirmed by observing the binding solution under TEM within the first few hours of of incubation. Thus, the nanoparticles are located in the same region as the outer ring of arginine residues (Arg61) as illustrated in *Figure 3.6*. It appears that the positive charge of the arginine residues behaves as a target for the assembly of the negatively charged nanoparticles. However, there is also reason to believe that guanidinium hydrogens can behave as hydrogen bond donors to sulfonate oxygens on the BSPP ligand, since guanidinium and organosulfonate ions are known to self-assemble into crystalline lattices through robust hydrogen-bonded networks[13]. Preliminary experiments in isothermal titration calorimetry have revealed an exothermic interaction upon titrating TMVcp with BSPP. Enthalpies on the order of those expected for hydrogen bonding have been obtained, however, further optimization of experimental parameters is required before quantitative data can be extracted. This would then be the primary interaction driving nanoparticle ring assembly.

The inter-particle distance measured from the center of adjacent nanoparticles is approximately 5 nm, while that for BSPP nanoparticles on a grid is 7 nm. It seems that inter-

particle repulsion is alleviated once particles are incorporated into the rings. The reason for this is unclear, however, the steric crowding imposed by the phenyl rings of BSPP may result in ligand displacement if nanoparticles are placed in close proximity to one another.

TEM image analysis reveals that the proportion of complete rings among the total number of binding events ranges from 46-70% depending on pH. If rings which are only missing one nanoparticle are included, this range increases to 79-91%, suggesting that the main barrier to ring completion is kinetic; the last nanoparticle to be incorporated into the ring must be of appropriate size and must approach the TMVcp disk in a specific relative orientation and position. The large number of unfunctionalized disks can be attributed to the fact that the concentration ratio of nanoparticles (0.9 µM) against TMV coat protein (20 µM) is 4.5 %. This ratio was initially chosen as a diagnostic condition to evaluate the existence of any sort of interaction but was maintained when it was determined that complete rings could assemble.

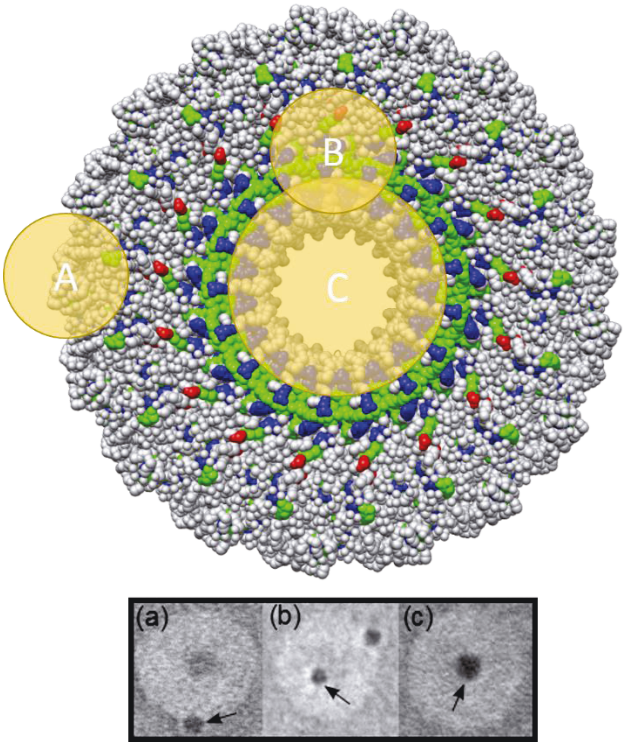


**Figure 3.6|** TEM images taken early in assembly period showing binding to (a) upper face edge of disk, (b) edge of inner pore and (c) on the pore itself. Schematic above illustrates the functionalities below each nanoparticle. Arginines are colored green, carboxylic acid residues in blue and the S123C cysteine mutation in red.

The most prominent change observed when varying pH is in the number of rings that possess a central nanoparticle. While the majority of the disks have central nanoparticles at pH values below 7.0, the number drops significantly as pH rises above. The arginine residues around the pore are likely responsible for binding the central nanoparticle. It is less clear which particular residues are involved. There are three arginine groups in the vicinity (Arg92, Arg90 and Arg46) but Arg92 and 46 are involved in α-helices and are expected to be unavailable. We have

concluded that the deprotonation of the Caspar carboxylates (mainly Glu50) is responsible for the increased negative charge above pH 7.0 and the decreased incidence of central nanoparticle binding. Our observation that the population of rings with central nanoparticles falls below 50% in this pH region supports this assertion. It is also observed that as pH is decreased the specificity of binding decreases – especially at pH 5.5. The result is that multiple nanoparticles bind inside the rings creating 'clusters' of nanoparticles on top of TMVcp disks. While these clusters are interesting structures, this renders pH 5.5 an impractical condition for ring self-assembly.

### 3.5 Monitoring nanoparticle rings by UV-Vis spectroscopy

As discussed in Chapter 1, adjacent plasmonic particles will undergo dipolar coupling, resulting in a red-shift in the combined nanoparticle plasmon resonance absorption. As gold nanoparticles assemble onto the 20S disk surface, one can expect such a coupling to occur. Since the change in the absorption profile is related to the number of particles in proximity, the assembly of the rings can be monitored in a UV-Vis spectrometer. In order to drive assembly, a very large concentration of nanoparticles is used. Unless corrected against a control solution (containing all the binding solution components without TMVcp), the detector is easily saturated and no useful data is obtained. This control solution is utilized in a dual-beam configuration in order to remove fluctuations in lamp intensity from the obtained spectra.

We observed a growth in absorbance between 570 nm and 600 nm consistent with the plasmon coupling of gold nanoparticles of their size *(Figure 3.7)*. Convoluted in this change in plasmon absorption is also an increase in the scattering volume of the assembling nanostructure as the number of nanoparticles incorporated increases. This effect results in an overall decrease in transmitted light to the spectrometer. By monitoring a wavelength where no absorption is expected (such as 800 nm), one can track the increase in scattering over time. The resulting kinetic curves have a biphasic shape, an initial period of rapid growth followed by a period of slower growth after 40 hours.

TEM samples obtained two days and five days after initiating assembly reveal that the majority of rings in the first 40 hours are missing only one or two particles – determined by the remaining space available for binding. After this period, one begins to observe rings with inter-particle spacing too small to be filled by additional particles which we label 'complete' rings.

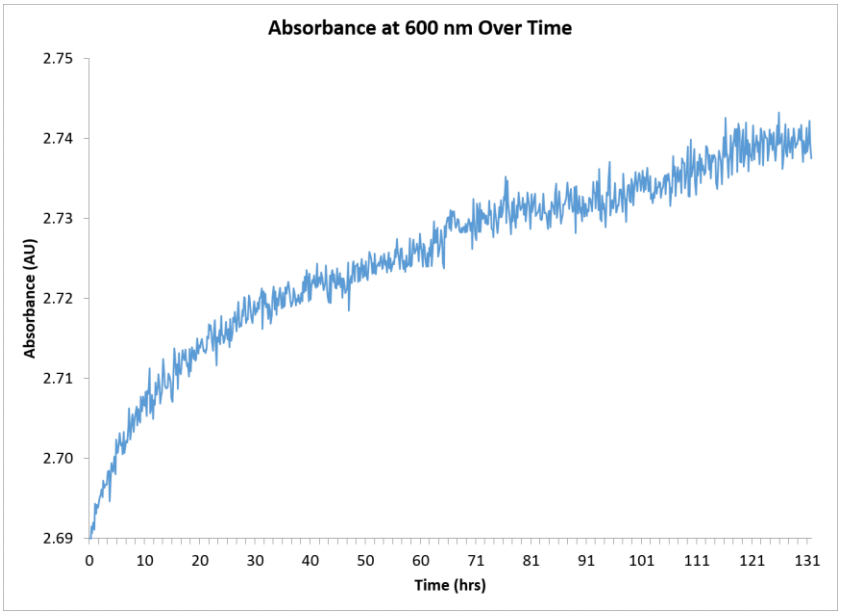


**Figure 3.7|** Increase in absorption at 600 nm. Signal is subtracted by a concentration matched nanoparticle control containing no TMV coat protein.

This is consistent with the biphasic growth kinetics observed. After 40 hours, growth is slowed as it becomes statistically less likely that a nanoparticle can approach a disk at the correct orientation to fill the remaining gap. Binding periods were fixed at 5 days despite indications that rings continued to assemble past this period.

There are significant differences in the change in spectra at various pH values *(Figure 3.8)* (the solution at pH 5.5 is not included in this analysis because it showed signs of precipitation at the end of the binding period). Each of the spectra also shows a dip in the 525 nm region. Based on measurements relating the dilution of our gold colloid solutions to the change in the absorbance of their associated plasmon, a drop of 0.1 absorbance units represents a drop in particle concentration as large as 0.8 µM. Thus, the observed drop in absorbance cannot be correlated to the number of particles involved in ring formation. Since there is no evidence of nanoparticle precipitation or aggregation, the source of the observed dip is an optical phenomenon that cannot be accounted for without first decoupling the various resonances elicited by these structures and their indiscriminant orientations in solution. It is, however, clear that the shape of the optical profile is highly correlated to the incidence of rings with central nanoparticles, and may be the

result of interference between the plasmonic resonance modes of the central nanoparticle and other plasmonic modes present.

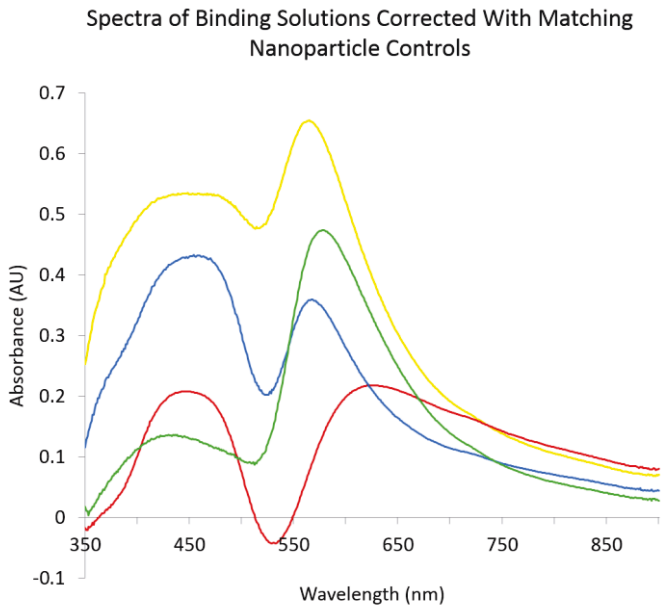


**Figure 3.8|** Spectra of assembly solutions at pH 6.0 (yellow), pH 6.5 (red), pH 7.0 (blue) and pH 7.5 (green), corrected by a concentration matched nanoparticle control containing no TMV coat protein.

The dip in the Absorbance spectrum is largest at pH 6.5 - the negative value of the valley at 525 nm is attributed to a slight mismatch in the concentrations of nanoparticles in the control relative to the assembly solution. At this pH, the population of TMVcp disks is high, while remaining far enough below the pKa of the inner carboxylate groups such that many of the rings obtain a central nanoparticle. The Absorbance at pH 7.0 is qualitatively similar in lineshape due to similar repulsion conditions as at pH 6.5. At pH 6.0, the population of disks (and thus the yield of gold nanorings) is smaller, even though the chance of having a central nanoparticle is larger. This results in a more asymmetric dip in the Absorbance. At pH 7.5, there are few disks, and the majority of the nanorings do not contain a central nanoparticle. This results in a highly asymmetric Absorbance peak at 575 nm, with a small dip at 525 nm.

## 3.6 Fluorescence spectroscopy

There are three natural amino acids which can contribute to a protein's intrinsic fluorescence; tryptophan, tyrosine and phenylalanine. While TMV possesses all three of these amino acids, tryptophan has a significantly stronger fluorescence and is often utilized to gain insight into the conformational state of a protein. Tryptophan residues are often located at various locations of a protein in different microenvironments. Polarizability, microviscosity, adjacency of charged groups and numerous other interactions will influence the intensity and Stokes shift of the

resulting fluorescence. Tryptophan is maximally excited at around 280 nm. Tryptophans buried in the low polarity hydrophobic pockets of a protein often fluoresce at around 331 nm at low yield. Conversely, tryptophans on the surface of a protein are exposed to the much higher polarity of an aqueous environment and fluoresce at longer wavelengths (around 350 nm) and with higher quantum yield[14].

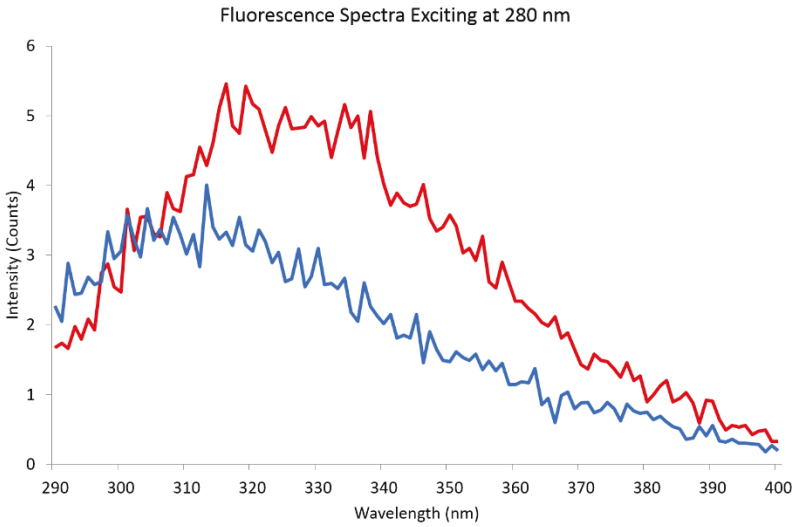


**Figure 3.9|** Fluorescence spectra of assembly solutions excited at 280 nm before (red) and after (blue) the five day incubation period.

As a second probe to observe nanoparticle binding, we acquired fluorescence spectra excited at 280 nm at the start of the assembly period and after five days *(Figure 3.9)*. We observed a decrease in fluorescence with a simultaneous blue shift of the peak maximum. This change is consistent with the binding of nanoparticles to the surface of the TMV coat protein. Tryptophans exposed to the solvent are likely to come in close proximity to ring nanoparticles. This results in a frequently observed quenching of fluorescence intensity as coupling between the nanoparticle plasmon and tryptophan increases the likelihood of non-radiative decay mechanisms and decreases the fluorescence lifetime[15]. Buried tryptophans do not undergo this quenching and thus become the dominant contributors to the overall fluorescence after the binding period is complete.

## 3.7 Gel electrophoresis and nanoparticle incorporation rate

In order to purify these structures, horizontal gel electrophoresis was used to separate free nanoparticles from the ring constructs *(Figure 3.10)*. This was carried out on the pH 6.5 condition since it yielded the largest number of rings. The optical plasmon absorption of the nanoparticles allows the visualization of two bands, the slower moving, less concentrated rings

and the faster, free nanoparticles in high concentration. A grayscale image of the gel was used to map normalized grayscale intensity across distance from the wells. This resulted in a plot where peak areas could be determined to extract an approximate nanoparticle incorporation rate by dividing the area underneath the nanoring peak by the total area of the two peaks.

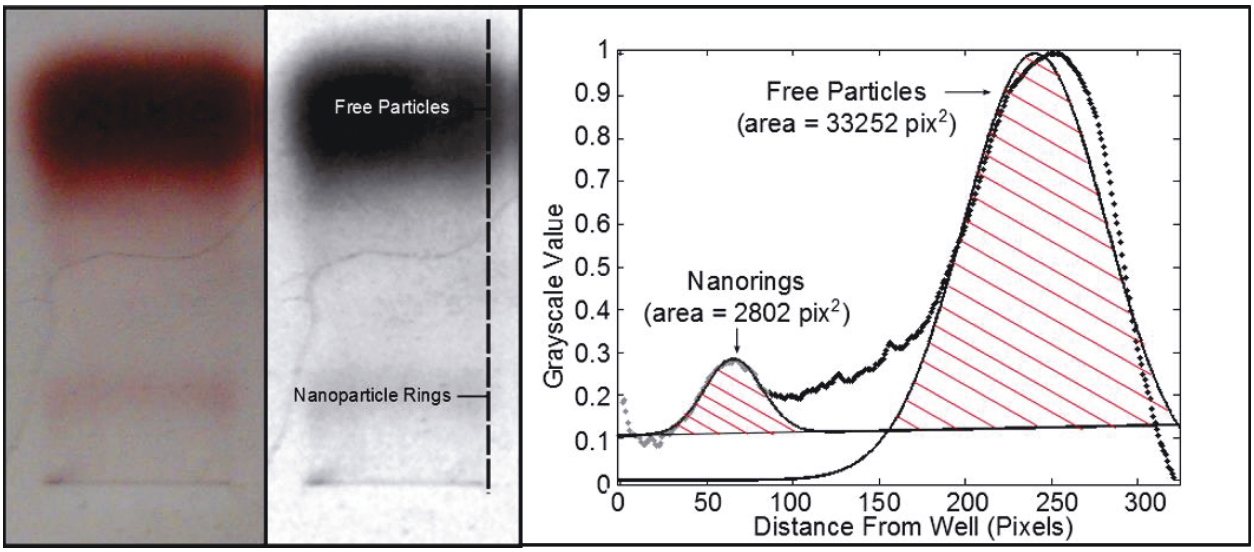


**Figure 3.10|** (Left) Photo taken of assembly solutions separated in agarose gel. (Middle) Image of agarose gel converted into greyscale. (Right) Gel band intensities are plotted and nanoparticle incorporation rate is determined by peak integration. Peaks are first fit to Gaussian curves.

Peaks were fit to a Gaussian curve before integration. A nanoparticle incorporation rate of 7.8% of the total number of nanoparticles was found. This result is supported by a TEM image analysis comparing the number of free nanoparticles and the number of particles incorporated into rings which yields a 6.0 ±2.7 % incorporation rate.

The logical subsequent step would be to excise the band corresponding to the purified rings and then extract them by agarose emulsification. When attempted this results in the recovery of TMV coat protein disks, several of which are bound to a few nanoparticles. No complete rings have been successfully isolated. It appears that in the process of purifying the free nanoparticles, the rings disassemble. This can be explained by the equilibrium nature of hydrogen bonding and the fact that nitrogen bound hydrogens produce relatively weak hydrogen bonds. On the other hand, there are presumably numerous BSPP ligands facing the arginine residues and each residue is capable of forming two hydrogen bonds. It is thus also

possible that the electric field applied on the rings during the electrophoresis experiment itself is detrimental to ring stability and that another purification method may be more successful. This is currently being investigated.

## 3.8 Methods

All substances were purchased at analytical grade with no further purification. Water used in all procedures was deionized using a Barnstead Diamond TII (Thermo Fisher) purification system. Monosodium phosphate, Disodium phosphate, sodium acetate, acetic acid and dithiothrietol (DTT) were purchased from Thermo Fisher Scientific (Pittsburgh, PA). Uranyl Acetate was purchased from SPI Supplies (West Chester, PA). All other chemicals were purchased from Sigma-Aldrich (St. Louis, MO)

Desalting and spin concentration was carried out using Corning Spin-X UF concentrators (VWR, Corning, NY) and unless otherwise specified, Specra/Por dialysis membranes (MWCO 3,500 kDa) were utilized for dialysis steps. All centrifugation was performed in a Sorvall RC6 Plus centrifuge.

**Transformation and Expression of S123C Mutant TMV Coat Protein.** Plasmids were graciously provided by the Matt Francis Group (Berkeley, California).

S123C Optimized DNA Sequence:

AGCTATAGCATTACCACCCCGAGCCAGTTTGTGTTTCTGAGCAGCGCCTGGGCGGATCCGATTGAACTG
ATTAACCTGTGCACCAATGCGCTGGGCAACCAATTTCAGACCCAGCAGGCGGCACCGTTGTGCAGCGTC
AGTTCAGCGAAGTTTGGAAACCGAGCCCGCAGGTTACCGTGCGCTTTCCGGATAGCGATTTTAAAGTGT
ATCGCTATAACGCCGTGCTGGATCCGCTGGTGACCGCGTGCTGGGCGCCTTTGATACCCGTAATCGTATC
ATTGAAGTGGAAAACCAGGCCAATCCGACCACCGCGGAAACCCTGGATGCGACCCGTCGTGTGGATGA
TGCCACCGTGGCGATTCGCTGTGCCACAATAACCTGATTGTGGAACTGATTCGTGGCACCGGCAGCTAT
AACCGTAGCAGCTTTGAAAGCAGCAGCGGCCTGGTGTGGACGAGCGGCCCGGCGACC

The procedure used for expression and purification of the S123C TMVCP is a modified version of that detailed by Francis et al.[16]

Tuner (DE3)pLysS competent cells (Novagen, San Diego, CA) were transformed with the vector, plated on LB-agar and incubated at 37°C overnight. A colony was removed from the plate and inserted into 50 mL of LB Broth containing 100 µg/mL ampicillin and placed in a shaker (250 rpm, 37°C) overnight. This culture was added to 1L of Terrific Broth containing 100 µg/mL ampicillin and shaken (250 rpm, 37°C) until the colony reached an optical density (600 nm) of 0.6-0.8. IPTG was added at this point to a final concentration of 30 µM. Cultures were grown for 24 hours at 30°C, harvested by centrifugation and stored at -80°C.

Cells from a 2L batch were thawed, resuspended in 200 mL of 20 mM triethanolamine (TEA) pH 7.2 and lysed by sonicating at a 60% duty cycle at 70% amplitude. The resulting lysate was clarified by ultracentrifugation for 30 minutes at 30,600xg. The supernatant was warmed to RT then stirred while adding a saturated ammonium sulphate solution dropwise to a final concentration of 35% (v/v). The white precipitate formed was isolated by ultracentrifugation for 30 minutes at 40,000xg then resuspended in 40 mL 20 mM TEA pH 7.2 with 2 mM DTT to avoid disulphide formation between cysteine mutations. The solution was dialyzed overnight against the same buffer to remove residual ammonium sulphate and then diluted to 700 mL in buffer before loading onto a DEAE Sepharose weak anion exchange column (GE Healthcare Life Sciences, Piscataway, NJ). The coat protein was eluted using a 0-300 mM gradient. Purity was confirmed by SDS-PAGE. Yields ranged between 9-10 mg.

**Assembly of S123C-TMV-CP Disks and Rods.** TMV coat protein stored at 4°C in TEA buffer (20 mM, pH 7) was dialyzed into the desired pH using acetate buffer for the pH range 5.0-5.5 and phosphate buffer for the pH range 6.0-7.5. The concentration of buffer used was set so that the ionic strength of the buffer was 100 mM. Dialysis was carried out over 24 hours at room temperature using Slide-A-Lyzer Dialysis Casettes (3.5 kDa MWCO) (Thermo Fisher Scientific). Protein concentration was determined by absorbance at 282nm ($\epsilon$ = 1.27 mL $mg^{-1}$ $cm^{-1}$)[17] using a Cary 100 Bio Spectrometer. The concentration of TMV coat protein was set at 0.4 mg/mL. After dialysis the protein was left to sit at room temperature for 24 hours for its assemblies to reach equilibrium.

**Synthesis of BSPP Passivated Gold Nanoparticles.** As detailed by Murphy et al.[18], tetrachloroauric acid ($2.5 \times 10^{-4}$ M) and sodium citrate ($2.5 \times 10^{-4}$ M) in 20 mL of deionized water was reduced by adding 1M of sodium borohydride dissolved in 0.6 mL with vigorous stirring to produce 3.5-5.0 nm nanoparticles. After 5 minutes, BSPP was dissolved in the solution to a concentration of 1 mg/mL. The nanoparticles were then stored at room temperature for 24 hours in the dark. When ready to use, the nanoparticle solution was desalted using a 1 mg/mL solution of BSPP and then spin concentrated to 400 µL with a SH-3000BK free bucket rotor at 3000xg[19].

**Nanoparticle Ring Assembly and Analysis.** 100 µL of concentrated BSPP passivated gold nanoparticles were added to 900 µL of TMV coat protein solution and stored in the dark at 23°C for three days. UV-Vis spectra in the 200-800 nm region were collected using a Cary 100 Bio instrument at the beginning and after the three day period. Kinetic data was collected for specific conditions by recording the UV-Vis spectrum every 10 minutes for the three day period. Fluorescence spectra were collected using a Cary Eclipse at an excitation wavelength of 280 nm. TEM samples were plated on 200-mesh carbon coated copper grids (Canemco, Lakefield, QC, Canada) for 5 minutes before wicking using filter paper and stained using 1% uranyl acetate or 2% phosphotungstic acid. Images were collected using a Philips CM200 TEM at 200kV. Analysis of UV-Vis and fluorescence data was carried out using MATLAB. TEM images were analyzed using ImageJ to determine the ratio of full to partial rings. Ring formation events were classified as 'Full (F)', 'Missing one nanoparticle (N-1)' and 'Incomplete (I)' as illustrated in *Figure 3.11*.

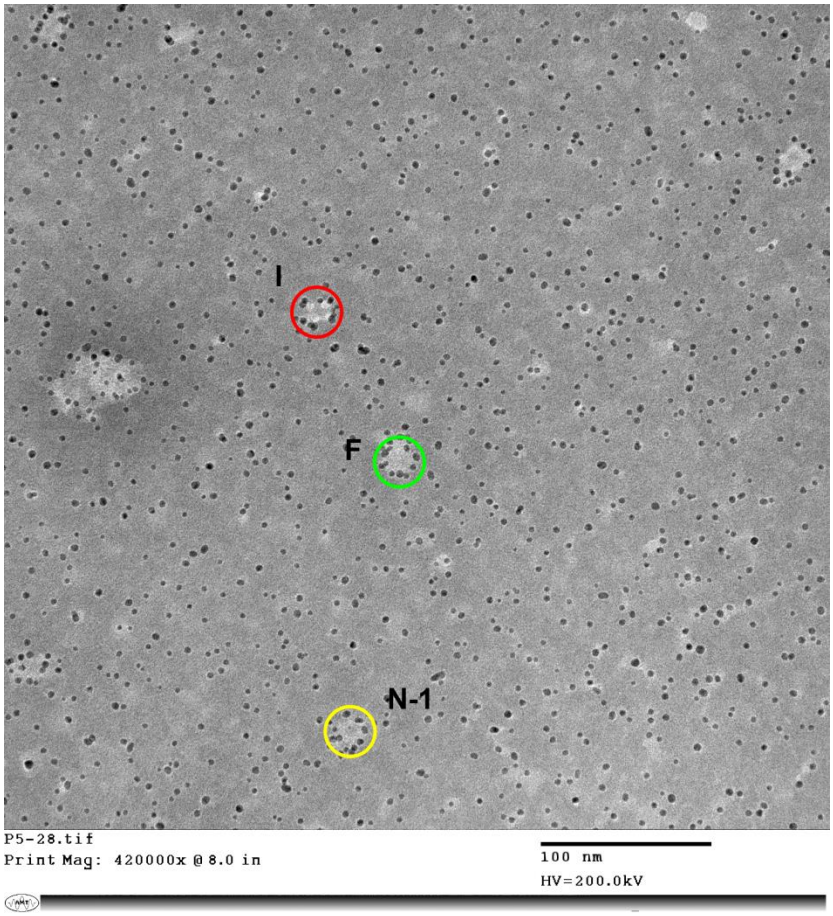


**Figure 3.11|** Illustration of how full (F), partial (N-1) and incomplete (I) rings are identified and sorted.

**Gel Electrophoresis.** Binding solutions of 1 mL were spin concentrated down to 50 µL and run in Bis-Tris running buffer (0.2 M, pH 6.5) in a horizontal agarose gel (1.5% agarose, 65V). The gel was subsequently photographed and converted to greyscale. Analysis of band intensities was carried out in ImageJ and Gaussian fits were applied using Matlab.

## 3.9 Conclusions

Gold nanoparticle rings, 22 nm in diameter, were assembled by the directed organization of BSPP-functionalized nanoparticles by arginine residues on the TMV disk surface. The dominant force appears to be hydrogen bonding between sulfonyl oxygen atoms on the sulfonic acid moieties of BSPP and the guanidinium hydrogens of arginine. A similar interaction drives the binding of nanoparticles on the center of the disk. This interaction is gated by adjacent carboxylic acid groups which, through deprotonation, can prevent the binding of nanoparticles

by electrostatic repulsion. While the hydrogen bonding interaction cannot provide the structural integrity of covalent attachment, the reversible nature of the interaction adds a dynamic aspect to this plasmonic system which warrants further investigation.

This study illustrates the utility of virus capsids as templates for self-assembly to create rings on a scale that is yet unachievable by other means. It is hoped that a working purification method can eventually be conceived so that spectroscopic properties of the rings can be extracted. The removal of the large number of free nanoparticles in the solution will enable quantitative analysis and comparison with theoretical models described in Chapter 1. Admittedly, the quality of the rings produced using this procedure does not compete well with the precision obtained using top-down photolithographic methods, the likely reason is that with numerous arginines on the surface of the disk and the relatively large area binding area provided by the nanoparticles, the nanoparticles are given too much spatial freedom. This has prompted the use of conjugation strategies to functionalize the edge of the disk in the hopes that the small area available for binding on the edge would impose constraints that result in more precise ring geometries. This is discussed in detail in the next two chapters.

## Citations


1. Nagano, N., Ota, M. & Nishikawa, K. Strong hydrophobic nature of cysteine residues in proteins. *FEBS Lett.* **458,** 69–71 (1999).

2. Blum, A. S. *et al.* Cowpea Mosaic Virus as a Scaffold for 3-D Patterning of Gold Nanoparticles. *Nano Lett.* **4,** 867–870 (2004).

3. Miller, R. a, Presley, A. D. & Francis, M. B. Self-assembling light-harvesting systems from synthetically modified tobacco mosaic virus coat proteins. *J. Am. Chem. Soc.* **129,** 3104–9 (2007).

4. Butler, P. J. G. Structures and roles of the polymorphic forms of tobacco mosaic virus protein. *J. Mol. Biol.* **72,** 25–35 (1972).

5. Zahr, O. K. & Blum, A. S. Solution phase gold nanorings on a viral protein template. *Nano Lett.* **12,** 629–33 (2012).

6. Schiffels, D., Liedl, T. & Fygenson, D. K. Nanoscale structure and microscale stiffness of DNA nanotubes. *ACS Nano* **7,** 6700–10 (2013).

7. Zhang, C., Yang, J. & Xu, J. Circular DNA logic gates with strand displacement. *Langmuir* **26,** 1416–9 (2010).

8. McMillan, R. A. *et al.* Ordered nanoparticle arrays formed on engineered chaperonin protein templates. *Nat. Mater.* **1,** 247–52 (2002).

9. Strotman, N. A. *et al.* Catalyst-controlled regioselective Suzuki couplings at both positions of dihaloimidazoles, dihalooxazoles, and dihalothiazoles. *J. Org. Chem.* **75,** 1733–9 (2010).

10. Zhang, J., Langille, M. R. & Mirkin, C. a. Photomediated synthesis of silver triangular bipyramids and prisms: the effect of pH and BSPP. *J. Am. Chem. Soc.* **132,** 12502–10 (2010).

11. Yang, J., Lee, J. Y., Too, H.-P. & Valiyaveettil, S. A bis(p-sulfonatophenyl)phenylphosphine-based synthesis of hollow Pt nanospheres. *J. Phys. Chem. B* **110,** 125–9 (2006).

12. Han, X., Goebl, J., Lu, Z. & Yin, Y. Role of salt in the spontaneous assembly of charged gold nanoparticles in ethanol. *Langmuir* **27,** 5282–9 (2011).

13. Russell, V. a. & Ward, M. D. Two-dimensional hydrogen-bonded assemblies: the influence of sterics and competitive hydrogen bonding on the structures of guanidinium arenesulfonate networks. *J. Mater. Chem.* **7,** 1123–1133 (1997).

14. Burstein, E. A., Vedenkina, N. S. & Ivkova, M. N. FLUORESCENCE AND THE LOCATION OF TRYPTOPHAN RESIDUES IN PROTEIN MOLECULES. *Photochem. Photobiol.* **18,** 263–279 (1973).

15. Dulkeith, E. *et al.* Fluorescence Quenching of Dye Molecules near Gold Nanoparticles: Radiative and Nonradiative Effects. *Phys. Rev. Lett.* **89,** 203002 (2002).

16. Dedeo, M. T., Duderstadt, K. E., Berger, J. M. & Francis, M. B. Nanoscale protein assemblies from a circular permutant of the tobacco mosaic virus. *Nano Lett.* **10,** 181–6 (2010).

17. Fraenkel-Conrat, H. Degradation of tobacco mosaic virus with acetic acid. *Virology* **4,** 1–4 (1957).

18. Gole, A. & Murphy, C. J. Seed-Mediated Synthesis of Gold Nanorods: Role of the Size and Nature of the Seed. *Chem. Mater.* **16,** 3633–3640 (2004).

19. Loweth, C. C. J., Caldwell, W. B. W., Peng, X., Alivisatos, a. P. & Schultz, P. G. DNA-Based Assembly of Gold Nanocrystals. *Angew. Chemie Int. Ed.* **38,** 1808–1812 (1999).

# Chapter 4
# *Covalent modification of the TMV coat protein N-terminus*


Abstract

The conjugation of two different carboxylic acids to TMV coat protein using carbodiimide chemistry is reported. The first molecule, α-lipoic acid, is conjugated to the S123C mutant of TMVcp as a handle for the self-assembly of gold nanoparticles into rings. The second molecule, 5-azidopentanoic acid, is conjugated to wild-type TMV coat protein as a method of increasing the functional versatility of TMV as a template for self-assembly. It is determined that the 20S disk phase of TMVcp possesses an N-terminus that is sterically hindered by the adjacent C-terminus which hampers conjugation efficiency. This is not the case in the other aggregation states of TMV coat protein. The S123C mutant of TMVcp is found to have an extraordinary preference for the 20S disk, resulting in generally low conjugation yields of α-lipoic acid.

## 4.1 Introduction

The use of non-covalent, intermolecular interaction for templated self-assembly is attractive for its ease of execution. Requiring no prior modification of the protein capsid, it holds no risks in compromising the integrity of the scaffold. Unfortunately, the location of the arginine residues utilized in Chapter 3 provide little steric constraint and do not take advantage of the shape of the protein. The result are rings that deviate from an ideal circular geometry. One of the advantages of using a protein-based scaffold is the existence of an extensive library of conjugation methods for the implementation or modification of chemical functionality on the protein surface.

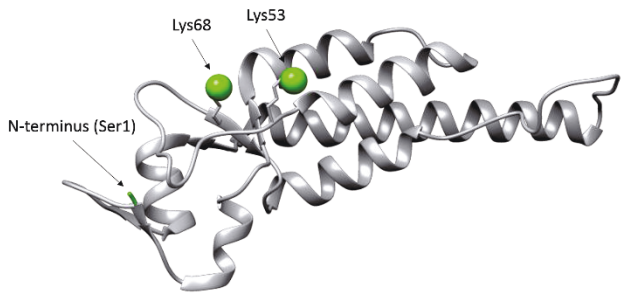


**Figure 4.1|** Illustration of TMVcp subunit with primary amines (Lys53, Lys68 and N-terminus) shown in green.

The choice of TMV coat protein is particularly fortuitous because of the three primary amines present on the capsid (Lys 53, Lys 68 and the N-terminus), Perham et al. have found that only Lys 68 and the N-terminus are accessible for reaction *(Figure 4.1)*[1]. Furthermore, Lys 68 is relatively hindered unless the coat protein is in a disassembled state. Gallwitz has shown that reaction of 4-sulfo-phenylisothiocyanate with intact TMV predominantly modifies the N-terminus[2]. The reactivity of the lysines in the 20S disk assemblies is not as well characterized but it is conceivable that they would be similarly hindered.

This chapter describes our attempts at the exclusive modification of the TMV capsid protein N-terminus in the 20S disk form. In the continued pursuit of producing geometrically precise nanoparticle rings, α-lipoic acid is conjugated to the N-terminus, providing a dithiolane moiety that remains stable until reacted with gold nanoparticles. The bidentate attachment provides a robust linkage between nanoparticles and TMV coat proteins. To expand the functionality of the 20S disk as a template, we have also conjugated azidopentanoic acid to the N-terminus, producing a platform for the circular assembly of alkyne functionalized molecules through copper catalyzed azide-alkyne cycloaddition.

## 4.2 Conjugation of proteins by carbodiimides

Carbodiimides are attractive molecules for protein modification because they can be utilized in mild conditions, circumventing the need to refold the protein – a laborious and often impossible task. They also result in a conjugate containing no additional atoms and are thus known as a zero-length cross-linkers. Carbodiimides are utilized by organic chemists as dehydration agents and will react with carboxylic acids to form an O-acylisourea. This acylating agent is vulnerable to nucleophilic attack at the carbonyl carbon. For protein conjugation, carbodiimides are almost exclusively used to conjugate carboxylic acids and amines, resulting in an amide bond and the loss of a water molecule.

EDC (1-ethyl-3-(3-dimethylaminopropyl)carbodiimide hydrochloride) is perhaps one of the most popular carbodiimides for conjugating carboxylates to amines and was initially adapted to the purpose by Hoare and Koshland[3] *(Figure 4.2)*. It has since been used to modify carboxylic acid residues with small molcules[4], conjugate enzymes to polymers[5], cross-link proteins to create films on silicon[6] and bind peroxidases to single-walled carbon nanotubes[7] among many examples. EDC also reacts with thiolates and alcohols (A Steglich esterification) to form

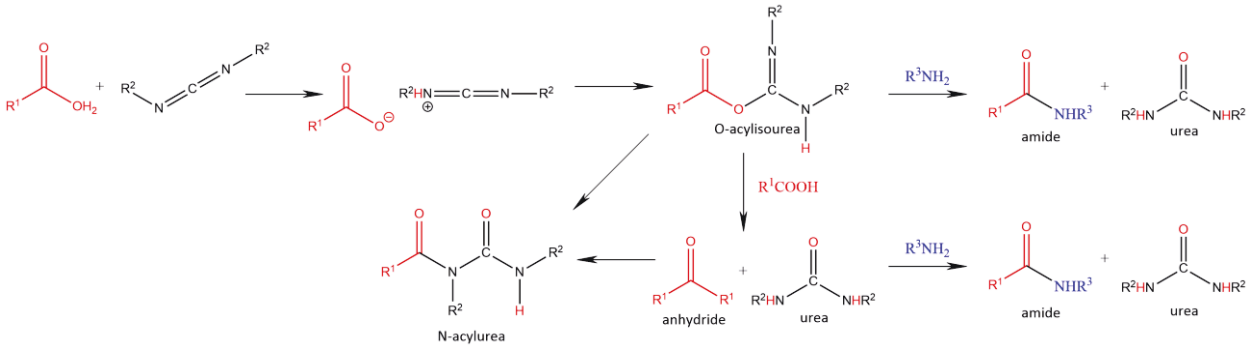


**Figure 4.2|** Reactions of EDC with carboxylic acids. The O-acylisourea intermediate may react with a primary amine to form an amide linkage or react with another carboxylic acid to form an anhydride which similarly reacts with amines to form amides. An undesired rearrangement of O-acylisourea to N-acylurea is an undesired side reaction which negatively impacts yield.

thioesters and esters respectively, however, the rate is significantly slower than the coupling with amines and so this does not interfere with yield in most circumstances.

Proteins often cannot remain intact in organic solvents and thus bioconjugation strategies usually occur in aqueous solution. Unfortunately, while EDC is stable for several hours in water[8], the o-acylisourea intermediate, upon reaction with the carboxylate, is rapidly hydrolyzed in water. It can also undergo an undesirable rearrangement into the stable N-acylurea[9]. This problem is resolved by adding N-hydroxysuccinimide (NHS), or a more water-soluble derivative, N-hydroxysulfosuccinimide (sulfo-NHS) to the reaction[10] *(Figure 4.3)*. NHS and sulfo-NHS will react with the unstable o-acylisourea intermediate to form an amine reactive NHS-ester with a half-life of 4-5 hours at pH 7[11]. The NHS moiety is easily displaced through nucleophilic substitution by amines, resulting in the desired amide. Sulfo-NHS is most often used in aqueous conditions due to the increased solubility of the subsequent ester.

The long half-life of the NHS-ester allows the use of a two-stage reaction protocol. First activating the carboxylic acid with EDC and sulfo-NHS, quenching the EDC, and then transferring the NHS-ester to the amine-containing molecule or protein. This is particularly useful when targeting amines on proteins without modifying carboxylic acids which are also invariably present, avoiding unwanted protein cross-linking. A two-step method is also advantageous because the activation of the carboxylic acid by EDC and NHS or sulfo-NHS is favored at a lower pH of 5-6, while the reaction of the NHS-ester with amines is optimal at pH 7-8. The EDC can be quenched before the second step with β-mercaptoethanol which reacts rapidly at the sulfhydryl group with remaining EDC[12]. This eliminates the need to purify the NHS-ester before transfer to the amine target.

If the carboxylate one desires to conjugate is not on the protein, one can avoid having to

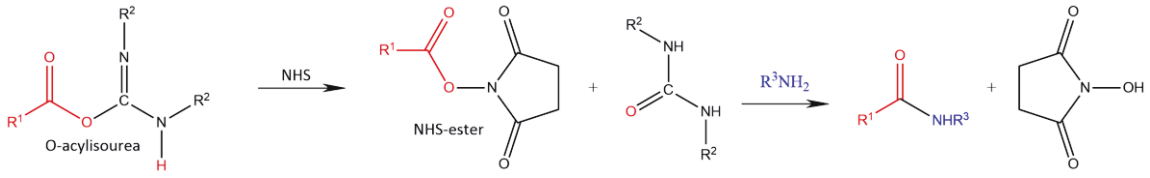


**Figure 4.3|** Reaction of O-acylisourea with N-hydroxysuccinimide and its derivatives to form an 'activated' carboxylic acid NHS-ester. This long lived species can react with amines to form amides.

synthesize fresh NHS-ester for every conjugation by carrying out the carboxylate-activating step in an organic solvent. In these cases, dicyclohexylcarbodiimide (DCC) is often used instead of

EDC in a dried solvent such as tetrahydrofuran (THF) with NHS instead of sulfo-NHS[13]. DCC rapidly reacts in the presence of a carboxylic acid and NHS to form an activated NHS-ester. The side product, dicyclohexylurea, like many dialkylureas, is poorly soluble and quickly precipitates. This makes its separation by filtration relatively simple. The reaction can be carried out in stoichiometric amounts and often the crude product is utilized without further purification. The advantage of this method is that the NHS-ester can be isolated and then stored for extended periods of time. It also allows a more accurate measure of the concentration of ester during the functionalization of the protein, as unwanted reactions to non-target residues can occur in some proteins when exposed to high concentrations of NHS-esters.

Both the aqueous two-stage method using EDC and sulfo-NHS as well as the isolated NHS-ester method utilizing DCC and NHS have been explored in the following studies with varying success depending on the carboxylic acid we attempted to conjugate to the TMVcp N-terminus.

## 4.3 Functionalization of S123C TMVcp N-terminus with α-lipoic acid

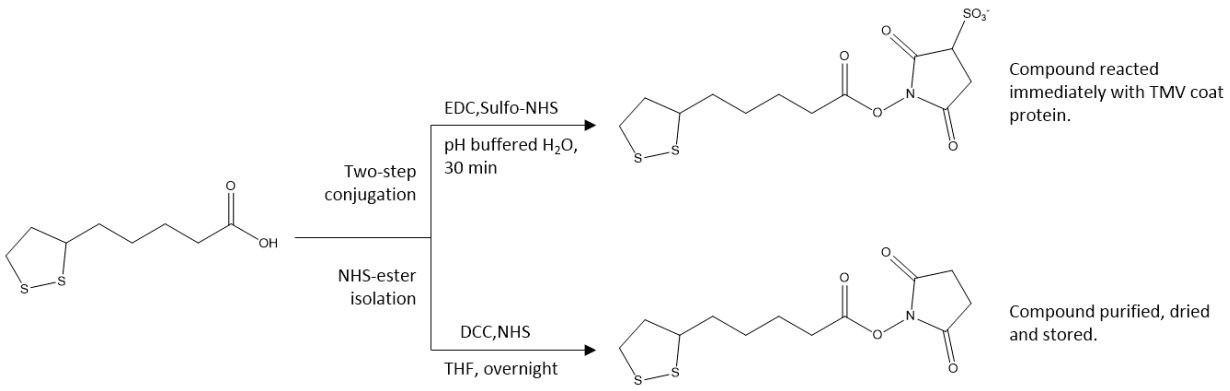


**Figure 4.4|** Reaction schemes illustrating activation of α-lipoic acid by either two-step conjugation with EDC and Sulfo-NHS in pH buffered aqueous solution or NHS-ester isolation by DCC and NHS in organic solvents.

In the course of working with both the wild-type and S123C mutant of TMVcp, we discovered that the two species had distinctly different stabilities and assembly behaviors. As described in Chapter 2, the wild-type TMV coat protein forms mostly helices at low pH conditions (pH < 6.5), 20S disks at moderate pH conditions (pH < 7.0) and disassembles into a-protein at basic pH conditions (pH > 7.0). The wild-type species also tends to disassemble from either helices or disks at concentrations below 11 µM and at low temperature. The S123C mutant differs from

the wild-type coat protein by a single mutation from a serine to a cysteine at the 123 position. While seemingly a minor modification, there are significant changes in the assembly behavior of the protein. Most prominently, the coat protein no longer forms helices in significant number. Instead, the 20S disk phase is favored until it begins to disassemble into a-protein above pH 7.0. There appears to be no lower limit to concentration that is required for disk assembly, and temperature appears to have no effect. In general, it appears this small mutation greatly stabilizes the 20S disk phase. This has been confirmed by the Francis group[14]. This promoted stability was thought to be of great advantage, since the helical phase was undesired for ring assembly, and thus the S123C mutant was chosen as the coat protein for conjugation studies with the purpose of subsequent ring assembly.

The two-step conjugation procedure was initially used for the conjugation of α-lipoic acid to TMVcp due to its popularity in biochemistry. A typical two-step EDC/Sulfo-NHS conjugation is carried out as follows; Lipoic acid is mixed with sulfo-NHS and EDC in a 5:5:2 ratio and incubated on a shaker for 30 minutes. The absolute amount utilized is determined by the desired ratio of N-lipoyloxy succinimide to TMVcp under the assumption that the activation reaction goes to completion – the final concentration of the ester after 30 minutes is equivalent to the concentration of EDC used. This assumption, while likely inaccurate, provided a method of quantification to utilize as a reference point. After the initial 30 minute incubation, the reaction is quenched with β-mercaptoethanol and an amount corresponding to the desired ester:TMVcp ratio is transferred to a solution of TMVcp. This conjugation step is incubated overnight before excess reagents are dialyzed out and the conjugation yield is determined by electrospray ionization mass spectroscopy coupled to a reverse-phase HPLC (LC-ESI MS). It should be noted that generally one cannot entirely rely on mass spectroscopy information to quantitate yield as the conjugated products may possess different ionization potentials, however, we have found that a relatively accurate picture of the relative concentrations of conjugated proteins is obtained when combining the mass spectroscopy data with chromatographic data obtained from the HPLC component.

The conjugated TMVcp is expected to have a mass of 17680 g/mol. As is shown in *Figure 4.5*, for a ratio of 100:1 at pH 7.0, only the unconjugated TMVcp appears. This was the case for various

pH conditions and ester:TMVcp ratios, however, a 100:1 ratio of ester to TMVcp was the highest possible ratio we could explore with this method due to the poor solubility of α-lipoic acid in aqueous media. It was believed that if the ester could be synthesized in organic solvents which could readily solubilize α-lipoic acid, a higher concentration of the ester with more accurate knowledge of the true ester:TMVcp concentration ratio would be possible.

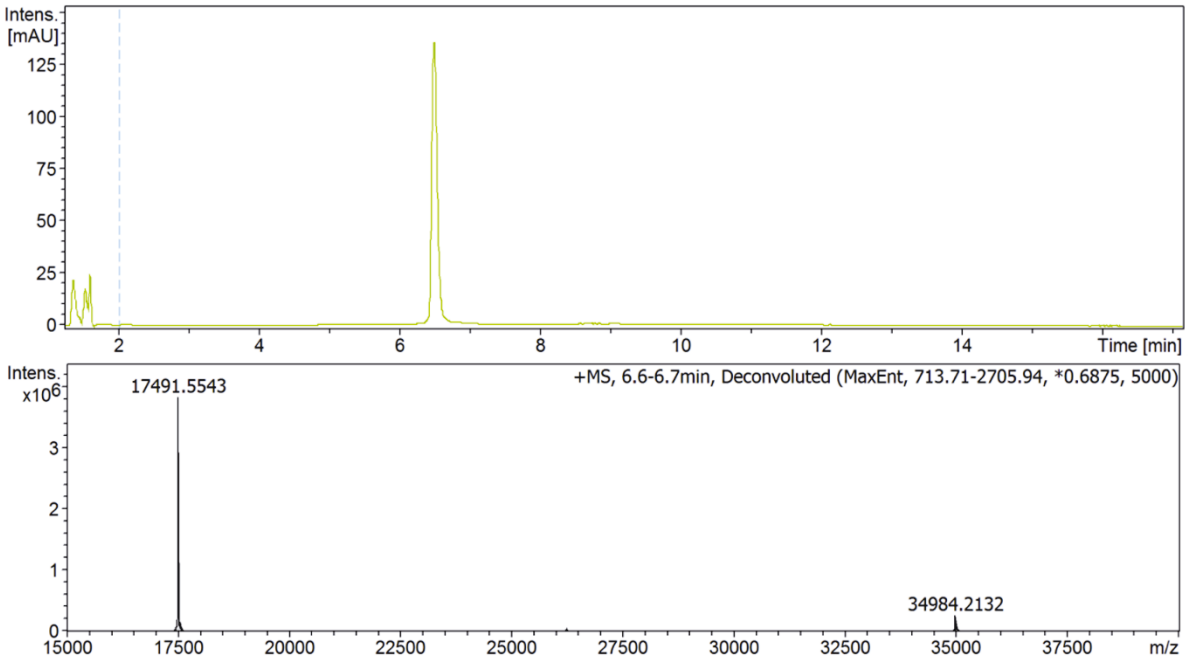


**Figure 4.5|** HPLC trace (above) and mass spectrometry (below) of failed attempt at two-step EDC/sulfo-NHS conjugation of α-lipoic acid in phosphate buffer at pH 7.0 set at an ionic strength of 0.1 M. TMVcp occasionally appears as a dimer (34984.2132 g/mol). Ester:TMVcp ratio was 100:1.

The ester synthesis, unlike the two-step method, uses a stoichiometric amount of DCC, NHS and α-lipoic acid dissolved in mildly polar solvents such as dichloromethane or tetrahydrofuran. The reaction is highly efficient. Indeed, the crude product is often used without further purification after filtering the insoluble dicyclohexylurea side product[15]. Due to the fact that the success of the conjugation would not only be influenced by the reactivity of the NHS-ester and the target N-terminal amine, but also the aggregation state of the TMVcp, a deductive approach was not possible and various pH and ionic strength conditions had to be screened. Lower pH values,

while increasing the rate of the competing hydrolysis pathway for the NHS-ester, would favor the 20S disk phase, which obscures the Lys68 residue and prevents its undesired modification. On the other hand, the N-terminal amine has a pKa of approximately 8.0[16] and is likely to be protonated and thus unable to behave as an effective nucleophile. At more basic conditions, the N-terminus becomes an effective nucleophile and the NHS-ester has a long half-life for hydrolysis, however, both these factors risk the modification of the Lys68 residue.

A ratio of 300:1 N-lipoyloxy succinimide to TMVcp was utilized to ensure that the hydrolysis of the ester at lower pH values did not deprive the protein of available reactant prematurely. LC-ESI MS results revealed that at pH values between 6.5 and 7.5, conjugation was consistently poor yielding (examples at pH 6.5 and 7.0 are shown in *Figure 4.6(a) and Figure 4.6(b)* respectively. This was the case regardless of the ratio of ester to TMVcp, which suggested that hydrolysis was not the limiting factor but perhaps the nucleophilicity or solvent accessibility of the amine.

At pH 8.0 and above, extensive modification of the coat protein occurs *(Figure 4.6(c))*. Unconjugated (17492 g/mol), singly conjugated (17680 g/mol), double conjugated (17868 g/mol), triple conjugated (18056 g/mol) and quadruple conjugated (18244 g/mol) coat protein is apparent. Three of these conjugations can be attributed to the N-terminus and two lysines (indicating an unfolding of the coat protein). The fourth conjugation is likely the result of nucleophilic attack by the cysteine thiol side group which has a pKa around 8.2. Closer inspection of the location of the cysteine mutation reveals an adjacent arginine residue (Arg122) which may further promote the nucleophilic, thiolate form through coulombic charge stabilization. This effect has been noted previously by Abad et al. in the labelling of cysteines with 4-[$^{18}$F]fluorobenzoate[17]. This modification can be prevented by incubating the coat protein with a reducing agent such as dithiothrietol (DTT) prior to and during conjugation so that the thiol moiety remains protonated and unavailable.

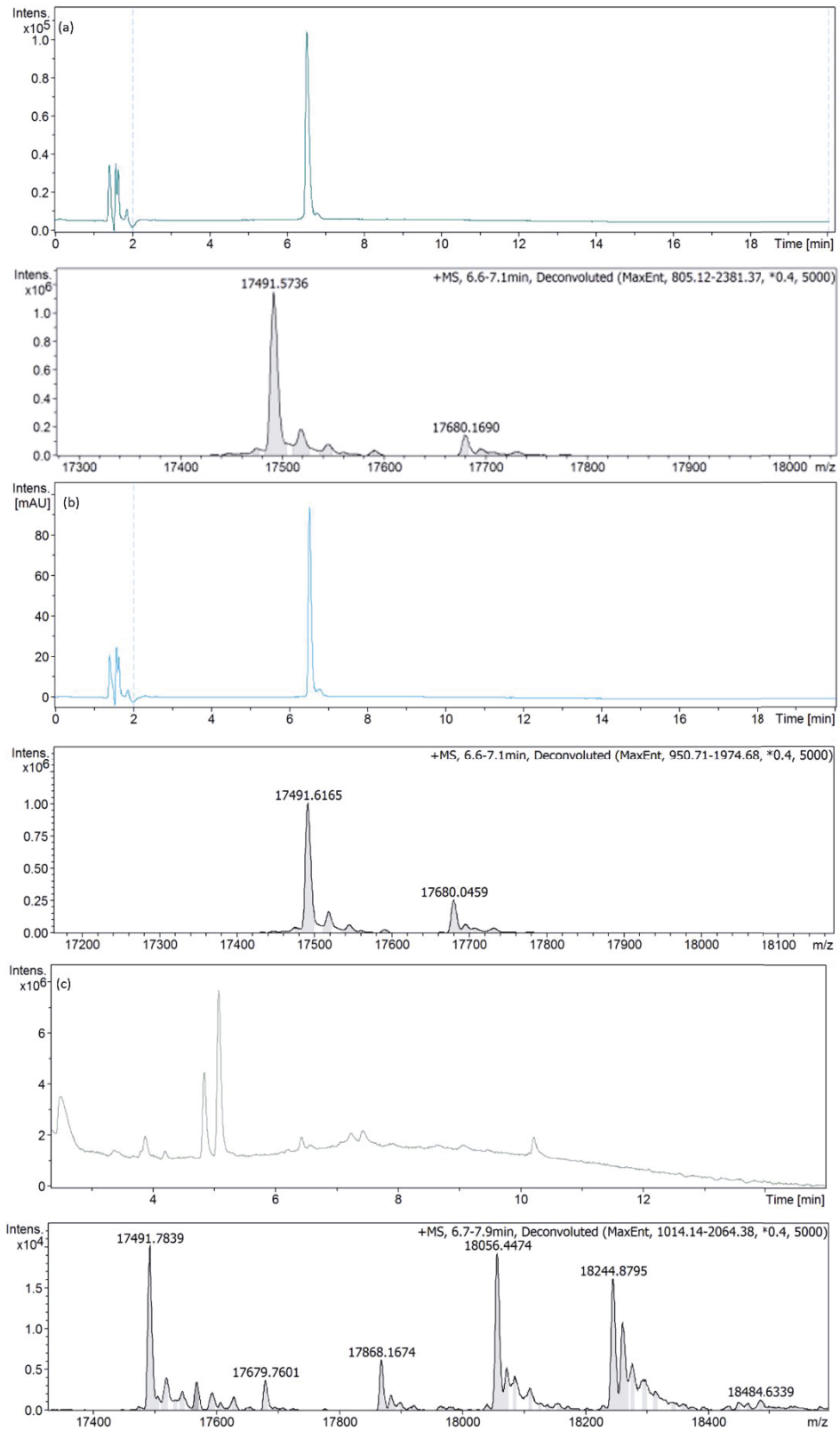


**Figure 4.6|** ESI-LCMS data of the conjugation of TMVcp with N-lipoyloxy succinimide at pH 6.5 (a), pH 7.0 (c) and pH 8.0 (c). All reactions are in phosphate buffer set at an ionic strength of 0.1 M. Ester:TMVcp ratio was 300:1.

The extensive conjugation of the coat protein suggests that it is at least partially present in a-protein form where Lys68 is exposed. The modification of the internal Lys53 suggests that the modification of Lys68 with α-lipoic acid results in the unfolding of the coat protein and the exposure of this normally obscured residue. This is not wholly unreasonable as α-lipoic acid possesses an alkyl chain long enough to introduce significant hydrophobic character to its target, disrupting the interactions responsible for the protein's secondary structure.

Since the disassembly into a-protein is driven by electrostatic repulsion, we expected that if the ionic strength of the solution was increased, the disk phase could re-establish itself. In another study, the change in conjugation efficiency was evaluated at pH 8.3 at low (50 mM) and high (400 mM) ionic strengths *(Figure 4.7)*. At the low ionic strength condition, at this slightly higher pH, there are as many as six conjugations of α-lipoic acid to the coat protein (the additional sites are likely hydroxyl groups). Upon increasing the ionic strength to 400 mM, only three conjugations appear in significant amount with the fourth – attributed to Arg53 – virtually eliminated. This suggests that the ionic strength could be increased further to prevent conjugation of Arg68. Combined with DTT, this would eliminate all conjugations except the desired N-terminal conjugation. However, there is still a significant unconjugated population which indicates that nucleophilicity of the amine is not the sole barrier to complete conjugation of the N-terminus, and that steric hinderance may play a significant role. The following section involving the conjugation of 5-azidopentanoic acid to the N-terminus of wild-type TMV coat protein explores this further.

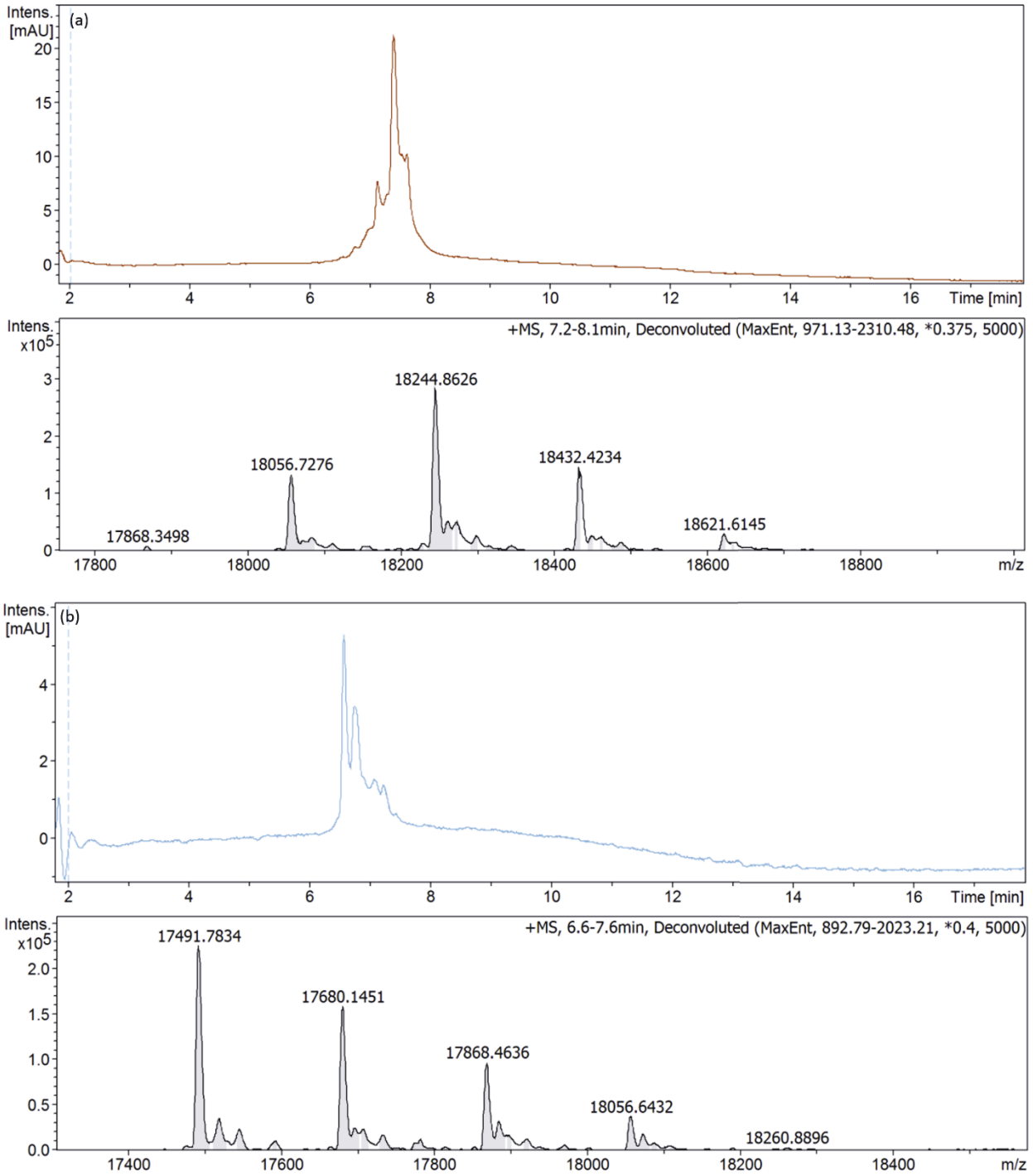


**Figure 4.7|** ESI-LCMS data of the conjugation of TMVcp with N-lipoyloxy succinimide in carbonate buffer at pH 8.3 at (a) 50 mM ionic strength and (b) 0.4 M ionic strength. Ester:TMVcp ratio is 50:1.

## 4.4 Functionalization of wild-type TMVcp N-terminus with 5-azidopentanoic acid

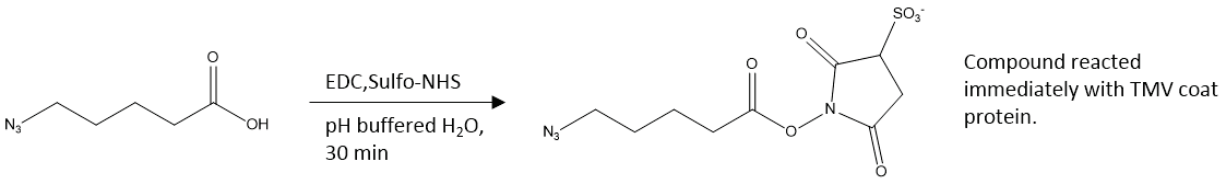


**Figure 4.8|** Reaction scheme illustrating activation of 5-azidopentanoic acid by two-step conjugation with EDC and Sulfo-NHS in pH buffered aqueous solution.

For the conjugation of 5-azidopentanoic acid (5-APA) to TMVcp, the wild-type form of the coat protein was utilized (wt-TMVcp). This is because, unlike the conjugation of α-lipoic acid for the eventual assembly of gold nanoparticle rings, the attachment of an azide to the N-terminus would have a much wider applicability. This versatility would be limited by using a mutant that did not possess the full self-assembly properties of wild-type TMV coat protein.

A two-step EDC/sulfo-NHS method was chosen for the conjugation (*Figure 4.8*) since the solubility of 5-APA in water is much higher than α-thioctic acid, and thus high ratios of ester to

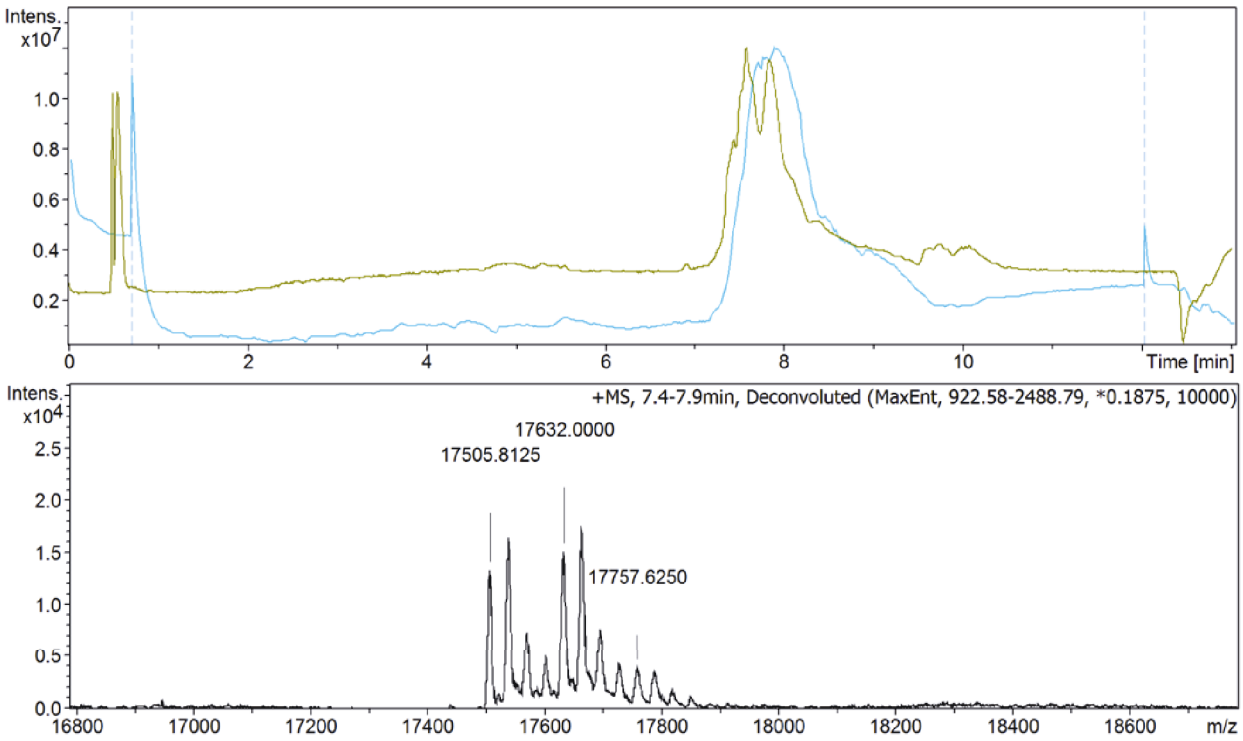


**Figure 4.9|** ESI-LCMS data of the two-step EDC/sulfo-NHS conjugation of wild-type TMVcp with 5-azidopentanoic acid. Reaction is buffered with phosphate at pH 7.0 at an ionic strength of 0.1 M.

TMVcp could be achieved. Furthermore, the higher cost of 5-APA makes it unsuitable for the larger scales needed for its isolated synthesis in organic media. Qualitative conjugation efficiencies were measured by ESI-LCMS as in the previous section. What is immediately striking *(Figure 4.9)* is that the conjugation efficiencies obtained are much higher for the same ester ratios utilized for α-lipoic acid. At a 100:1 ester:TMVcp ratio at pH 7.0, there is already approximately 50% yield of azide conjugated TMVcp (indicated by the appearance of a 17632 g/mol mass peak). A curious observation is the presence of peaks that are 16 g/mol larger than the mass of wild-type TMVcp and singly conjugated TMVcp. The origin of these peaks is currently unknown but control studies with unconjugated TMVcp shows similar additional peaks with 16 g/mol spacing. This effect may be a consequence of the ionization method utilized in the mass spectrometer.

The significantly larger propensity for reaction at the N-terminus in the wild-type protein appears to be related to the ability of the TMV coat protein to form helical structures. This ability is hindered in the mutant TMVcp, which favors the 20S disk phase almost exclusively. In contrast, the wild-type protein exists in a dynamic equilibrium between a-protein, 20S disks, lock washers and helices. As illustrated in *Figure 4.10*, the exposure of the N-terminus to the

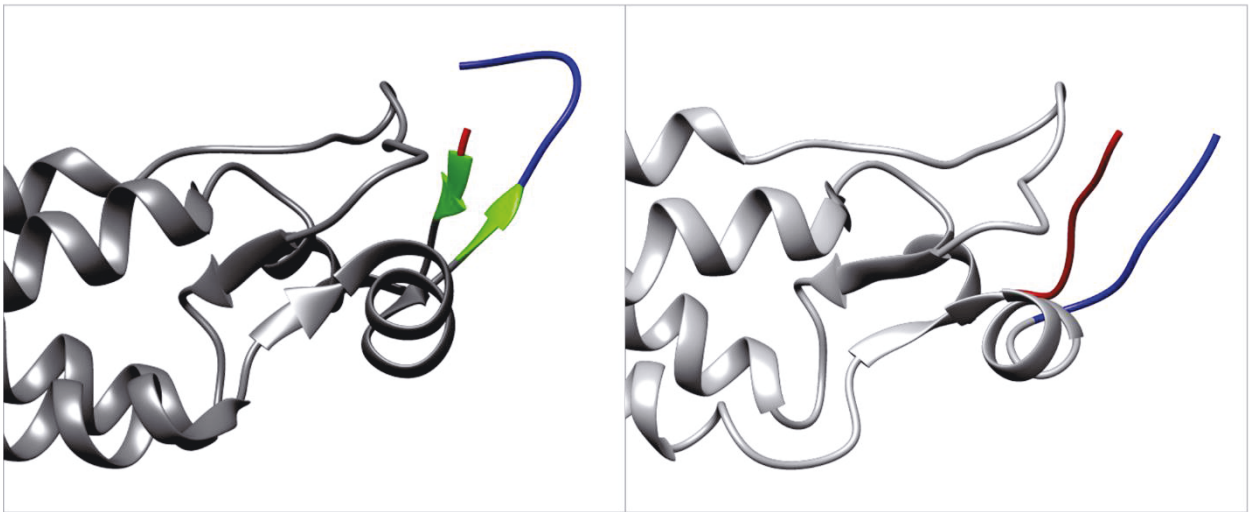

**Figure 4.10|** Conformation of TMV coat protein in a 20S disk (left) and lock-washer or helical rod (right). The red coloring shows the unstructured portion of the N-terminus. The green coloring shows the beta sheet formation responsible for retracting the N-terminus behind the unstructured C-terminus. The blue color illustrates the unstructured portion of the C-terminus which obscures the N-terminus in the 20S disk.

solvent is highly dependent on the aggregation state of the coat protein. In the 20S disk, the unstructured portion of the N-terminus appears to exist in a 'retracted' state due to a beta-sheet formation that begins two residues away. The unstructured portion of the C-terminus is long by contrast, and may act to obscure the N-terminus sterically from incoming NHS-esters. In a helical aggregate, such as the lock-washer or helical rod, the beta-sheet disassembles near the N-terminus and its unstructured portion becomes comparable to the C-terminus, likely increasing its exposure to the solvent and possible reactants.

## 4.5 Methodologies

All substances were purchased at analytical grade with no further purification. Water used in all procedures was deionized using a Barnstead Diamond TII (Thermo Fisher) purification system. Monosodium phosphate, disodium phosphate and sodium carbonate were purchased from Thermo Fisher Scientific (Pittsburgh, PA). All other chemicals were purchased from Sigma-Aldrich (St. Louis, MO).

**Mass spectrometry.** Analysis was performed using a Dionex U3000 HPLC coupled to a Bruker maXis Impact QTOF ESI mass spectrometer in positive potential mode. HPLC separation was run on a BEH C4 column using a gradient starting with an 80:20 mixture of 0.1% formic acid in water and 0.1% formic acid in acetonitrile and ending with only 0.1% formic acid in acetonitrile over 15 minutes. The flow rate used was 0.2 mL/min.

**Two-step EDC/sulfo-NHS conjugation.** All conjugations maintained a 2:5:5 ratio of EDC:sulfo-NHS:carboxylic acid. The carboxylic acid (either α-lipoic acid or 5-azidopentanoic acid) is dissolved with sulfo-NHS in 1 mL of buffer at the chosen condition. EDC is mixed last to begin the reaction. After a 30 minute incubation at room temperature, β-mercaptoethanol is added to 20x the concentration of EDC used. 100 µL of this solution is transferred to 900 µL of TMV coat protein solution buffered at the desired conditions and the solution is incubated at room temperature overnight. Excess reagents are removed by dialysis.

**Synthesis of N-lipoyloxy succinimide.** In 10 mL of dry THF, α-lipoic acid (0.01 M), NHS (0.01 M) and DCC (0.01 M) are dissolved with DCC added last. The reaction is allowed to proceed

overnight. Crude product is vacuum filtered to remove the urea byproduct and dried by rotary evaporation. The product is then recrystallized in toluene.

**Conjugation of TMVcp with pre-synthesized ester.** Since the ester was not appreciably soluble in water, it was dissolved in DMSO before addition to buffered TMV coat protein solutions. Experiments were run such that there was always 10% DMSO in the final conjugation solution. This amount of DMSO is observed to have no effect on TMVcp behavior. After addition of ester, solutions are incubated overnight. Excess reagent is removed by dialysis.

## 4.6 Conclusion

In summary, the conjugation of amines by NHS-esters, while often a simple procedure, is strongly affected in its application to TMV coat protein by the aggregation state of the coat protein itself. The wild-type TMV coat protein is more amenable to conjugation due to the fact that it exists in dynamic equilibrium between chiral and a-chiral aggregates, allowing chiral aggregates such as rods and lock-washers to be easily modified. The S123C mutant, on the other hand, disproportionately favors the 20S disk phase which is an advantage for ring formation but has an obscured N-terminal amine which compromises conjugation efficiency. Future work will involve further exploring the optimization of the conjugation of wild-type TMVcp. Also, it is likely that the N-terminus in the 20S disk can be made more accessible by extending it using site directed mutagenesis. Similar efforts have been reported by Francis et al.[18] which managed to significantly increase N-terminal conjugation yields.

## Citations


1. Perham, R. N. & Richards, F. M. Reactivity and structural role of protein amino groups in tobacco mosaic virus. *J. Mol. Biol.* **33,** 795–807 (1968).

2. Gallwitz, U. T. E., King, L., Perham, R. N. & Germany, W. Preparation of an Isomorphous Heavy-atom Derivative of Tobacco Mosaic Virus by Chemical Modification with 4-Sulpho-phenylisothiocyanate. 257–264 (1974).

3. Hoare, D. G. & Koshland, D. E. . J. A Method for the Quantitative Modification and Estimation of Carboxylic Acid Groups in Proteins. *J. Biol. Chem.* **242,** 2447–2453 (1967).

4. Yamada, H., Imoto, T., Fujita, K., Okazaki, K. & Motomura, M. Selective modification of aspartic acid-101 in lysozyme by carbodiimide reaction. *Biochemistry* **20,** 4836–4842 (1981).

5. Tyagi, R., Roy, I., Agarwal, R. & Gupta, M. N. Carbodi-imide coupling of enzymes to the reversibly soluble insoluble polymer Eudragit S-100. *Biotechnol. Appl. Biochem.* **28,** 201–206 (1998).

6. Tengvall, P., Jansson, E., Askendal, A., Thomsen, P. & Gretzer, C. Preparation of multilayer plasma protein films on silicon by EDC/NHS coupling chemistry. *Colloids Surfaces B Biointerfaces* **28,** 261–272 (2003).

7. Yu, X. Peroxidase activity of enzymes bound to the ends of single-wall carbon nanotube forest electrodes. *Electrochem. commun.* **5,** 408–411 (2003).

8. Gilles, M. A., Hudson, A. Q. & Borders, C. L. Stability of water-soluble carbodiimides in aqueous solution. *Anal. Biochem.* **184,** 244–8 (1990).

9. Iwasawa, T., Wash, P., Gibson, C. & Rebek, J. Reaction of an Introverted Carboxylic Acid with Carbodiimide. *Tetrahedron* **63,** 6506–6511 (2007).

10. Staros, J. V., Wright, R. W. & Swingle, D. M. Enhancement by N-hydroxysulfosuccinimide of water-soluble carbodiimide-mediated coupling reactions. *Anal. Biochem.* **156,** 220–222 (1986).

11. Cuatrecasas, P. & Parikh, I. Adsorbents for affinity chromatography. Use of N-hydroxysuccinimide esters of agarose. *Biochemistry* **11,** 2291–2299 (1972).

12. Grabarek, Z. & Gergely, J. Zero-length crosslinking procedure with the use of active esters. *Anal. Biochem.* **185,** 131–5 (1990).

13. Hermanson, G. T. *Bioconjugate Techniques*. 1323 (Academic Press, 2010). at <http://books.google.ca/books/about/Bioconjugate_Techniques.html?id=alooWMkRMk0C&pgis=1>

14. Francis, M. B. Personal communication.

15. Shi, L. *et al.* Plasmon resonance scattering spectroscopy at the single-nanoparticle level: real-time monitoring of a click reaction. *Angew. Chem. Int. Ed. Engl.* **52,** 6011–4 (2013).

16. Wetzel, R., Halualani, R., Stults, J. T. & Quan, C. A general method for highly selective crosslinking of unprotected polypeptides via pH-controlled modification of N-terminal .alpha.-amino groups. *Bioconjug. Chem.* **1,** 114–122 (1990).

17. Abad, S. *et al.* Rapid and high-yielding cysteine labelling of peptides with N-succinimidyl 4-[18F]fluorobenzoate. *Chem. Commun. (Camb).* **48,** 6118–20 (2012).

18. Obermeyer, A. C., Jarman, J. B. & Francis, M. B. N-terminal modification of proteins with o-aminophenols. *J. Am. Chem. Soc.* **136,** 9572–9 (2014).

# Chapter 5
# *Gold nanoparticle rings on N-terminally modified TMVcp disks*


## Abstract

The synthesis of gold nanoparticle rings by the reaction of BSPP-functionalized gold nanoparticles and α-lipoic-acid conjugated TMVcp (αLA-TMVcp) is reported. Unlike those assembled through non-covalent methods (Chapter 3), these rings were found to be significantly more stable to spin filtration and dialysis in order to separate complete rings from free nanoparticles. Unfortunately, these purification methods still fail to maintain the integrity of the rings at the time of writing. They require further optimization before we can obtain a spectroscopic characterization of pure solutions of gold nanoparticle rings.

## 5.1 Introduction

The gold-sulfur bond is ubiquitous in gold-based self-assembly systems. The interaction is utilized extensively in DNA-gold nanoconjugate assembly[1,2], self-assembled monolayers on gold substrates[3] and protein-nanoparticle conjugation. Although all noble metals show some degree of affinity for thiols, the Au-S bond is by far the most stable. While the details of this ligand chemistry are quite complex, it is currently established that $Au^+$ 6s electrons covalently bond to two of the four sulfur($sp^3$) hybrid orbitals, with an additional contribution from gold d-electrons, in an S-Au(I)-S configuration. This requires that the thiol be deprotonated, however a sulfhydryl will still weakly coordinate through sulfur lone pair electrons[4].

While undoubtedly a powerful interaction, studies in DNA-gold nanoconjugation have revealed that monothiol functionalized gold can unbind in aqueous solution due to competitive binding of other ligands[5]. This manifests as lowered gold-DNA conjugate yields. This problem is alleviated by utilizing molecules terminated in multiple thiol-anchors, such as the use of trithiol-capped DNA by Mirkin et al[6]. The resulting polyvalent interactions create more robust linkages that are unlikely to fail during synthesis and purification of nanoparticle conjugates. Lipoic acid has been used extensively for this reason through the bioconjugation strategies discussed in the preceding chapter. It was our hope that this polyvalent interaction would allow us to create gold nanoparticle rings which were more resilient to the processing steps required for purification. Herein reported is the fabrication of gold nanoparticle rings through the assembly of BSPP-stabilized gold nanoparticles on lipoic acid-modified TMVcp.

An interesting result of the collaboration between nanochemistry and biology in the fabrication of biologically templated nanostructures is the appropriation of traditionally biochemical techniques for nanostructure purification. Agarose gel electrophoresis has been used extensively to purify DNA-nanoparticle conjugates[7], peptide-functionalized nanoparticles[8] and virus-templated nanoparticles[9]. Sucrose gradient density centrifugation has also been used to separate virus-encapsidated gold nanoparticles[10], streptavidin linked nanoparticle dimers[11] and iron-oxide mineralized Cowpea Mosaic Virus[12]. While superbly effective in yielding high purity structures, the excision and extraction process for the isolation of the desired product in gel

electrophoresis is time consuming and results in significant loss. Density centrifugation can alleviate loss but requires extensive trial and error to determine optimal conditions for separation.

Dialysis and centrifuge filtration are significantly faster methods of protein purification with high retention, but have been problematic for nanoparticle purification. The high surface energy characteristic of metal nanoparticles can result in strong adhesive interactions between the nanoparticles and the cellulose or polypropylene based filters utilized in centrifuge filtration. Furthermore, since commercial filters are designed with simple protein desalting and concentration in mind, they rarely allow the passage of particles larger than 4-5 nm (the equivalent of a 100 kDa molecular weight cut-off). Commercial dialysis membranes, on the other hand, are sold with a much wider range of cut-offs and could feasibly separate free nanoparticles up to 20 nm in size. However, this requires that nanoparticles be stabilized with strong binding ligands to avoid their displacement over time in aqueous media. Fortunately, it is evident that BSPP-stabilized nanoparticles are both low-binding and stable to these methods and we have taken advantage of this stability to purify our nano-rings using these two techniques.

## 5.2 Assembly of nano-rings on α-lipoic acid functionalized TMV coat protein

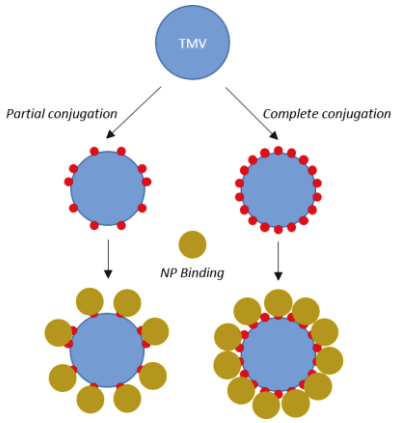


**Figure 5.1|** Schematic of the predicted effect of complete and partial conjugation on ring assembly.

There are two main stages that principally determine the quality of nanoparticle rings templated by N-terminally modified TMVcp; the efficiency of the N-terminal conjugation, and the binding of gold nanoparticles to the modified N-terminus. While there remains uncertainty in the efficacy of the conjugation of TMVcp with α-lipoic acid (αLA), we decided to proceed to the binding of nanoparticles for two reasons. The first is that we expected a statistical distribution of αLA-TMVcp subunits within a 20S disk aggregate of subunits. If this is the case, despite a partial yield, nanoparticles should distribute themselves evenly across the edge of the disk. If the

yield is above a minimum, the inter-particle spacing would remain small enough to allow plasmonic coupling *(Figure 5.1)*. The second reason is that BSPP functionalized AuNPs tend to assemble into linear assemblies by increasing the salt concentration in solution[13]. This mechanism may result in the side-by-side assembly of nanoparticles around the TMVcp disk, with both covalent and non-covalent bonding, resulting in complete rings. We did not expect such rings to remain complete during purification, however, similar measurements to those carried out in Chapter 3 could be made to compare the rings fabricated by the two methods.

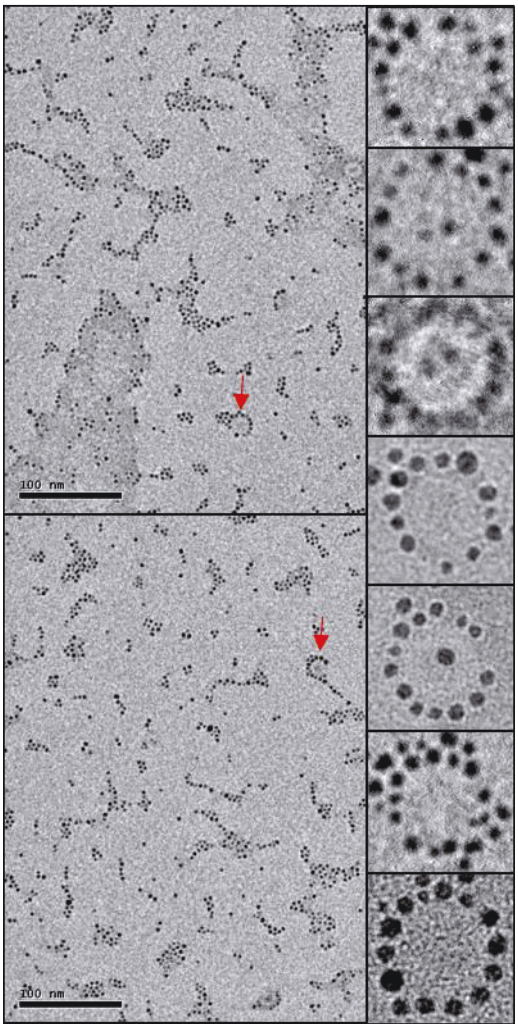


**Figure 5.2|** Surveys of unpurified ring solutions (left) and cropped images of individual conjugated TMVcp templated rings.

As mentioned in chapter 4, we have discovered that the S123C mutant of TMVcp displays an extraordinary preference for the 20S disk phase. In fact, we have observed that the 20S disk remains stable at concentrations at least 100 times lower than the 11 µM limit of the wild-type TMV coat protein. The main advantage of this finding is that the BSPP NPs need not be concentrated by such a large factor (50x for hydrogen-bonded AuNP rings) to achieve the necessary ratio of nanoparticles to TMVcp. Our method of assembly remains analogous to that of nano-rings in Chapter 3, with modifications to the absolute concentrations of TMV and gold nanoparticles to take advantage of the mutant's low-concentration stability. In these studies, the nanoparticle:TMV concentration ratio was maintained above 1:1 in order to prevent gold nanoparticles bridging multiple 20S disks.

Assembled rings have a diameter of 24.7 ± 1.1 nm with a center-to-center inter-particle distance of 5.1 ± 0.7 nm. This is consistent with the binding of ≈3.5 nm particles to the edge of the 18 nm 20S disk. We were

pleased to note that several complete or N-1 rings were observed. As is illustrated in *Figure 5.2*, the rings are arranged with significantly higher precision than is observed for H-bonded rings which supports the assertion that the edge of the disk provides additional support.

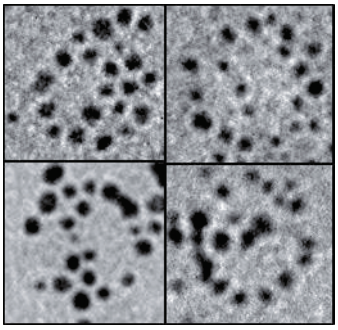

**Figure 5.3|** Examples of rings with top-face nanoparticle clusters.

In order to create the best chance for ring formation, the conjugated TMVcp solutions utilized were those produced at basic conditions (>pH 8.0) – which provided the highest degree of N-terminal conjugation but often resulted in the conjugation of other residues. The consequence of this choice is apparent in multiple instances where rings contain several particles bound on the top face of the disk *(Figure 5.3)*. The locations of the particles coincide with that of Lys68 and Cys123 and, therefore, appears to be the consequence of the additional conjugation of these sites by the NHS-ester. Presumably at least some of the clustering on the face of the disk is driven by the same hydrogen-bonding interaction which led to the assembly of rings in chapter 3. This interaction can be inhibited by incubating the conjugated TMV coat protein in BSPP before the addition of nanoparticles, thus blocking the arginine sites.

In order to isolate the rings, a combination of dialysis and spin filtration was utilized, both with a 100 kDa molecular weight cut-off, corresponding to a pore size of 5 nm. These two techniques removed a significant amount of free nanoparticles and left only aggregates templated by the TMVcp protein. As can be seen in *Figure 5.4*, the purification of the rings reveals the incomplete nature of the TMVcp conjugation, with the loss of most complete rings. An interesting effect are partial rings that are complete on one side. Such semicircular rings suggest that the linear assembly behavior of BSPP that can 'fill in' gaps in the conjugation of the 20S disks may survive purification with further optimization of the procedure.

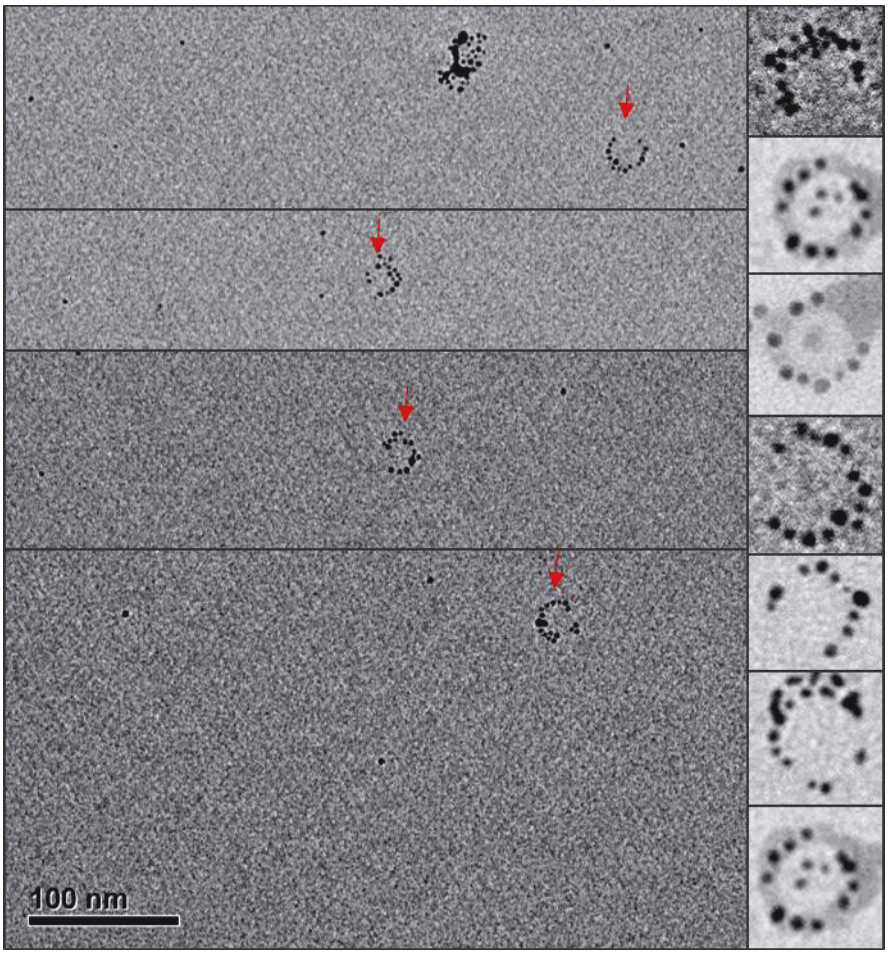


**Figure 5.4|** Surveys (left) and cropped images (right) of templated rings after purification by dialysis and spin filtration revealing incomplete nature of conjugation.

## 5.3 Monitoring the growth of ring solutions over time using UV-Vis spectroscopy

The growth of the rings over time can be tracked by UV-Vis *(Figure 5.5)*. TEM revealed a large degree of linear assembly by the free BSPP nanoparticles and thus the 600 nm peak could not be associated with only the growth of rings. Remarkably, an increase in absorption around 450 nm is observed with ring growth, similar to that observed in chapter 3.

On account of the clustering of nanoparticles on the upper disk surface, a pH study to observe whether the presence of a central nanoparticle could be tuned by deprotonating the Caspar carboxylates would not be fruitful until the over-conjugation issue is addressed.

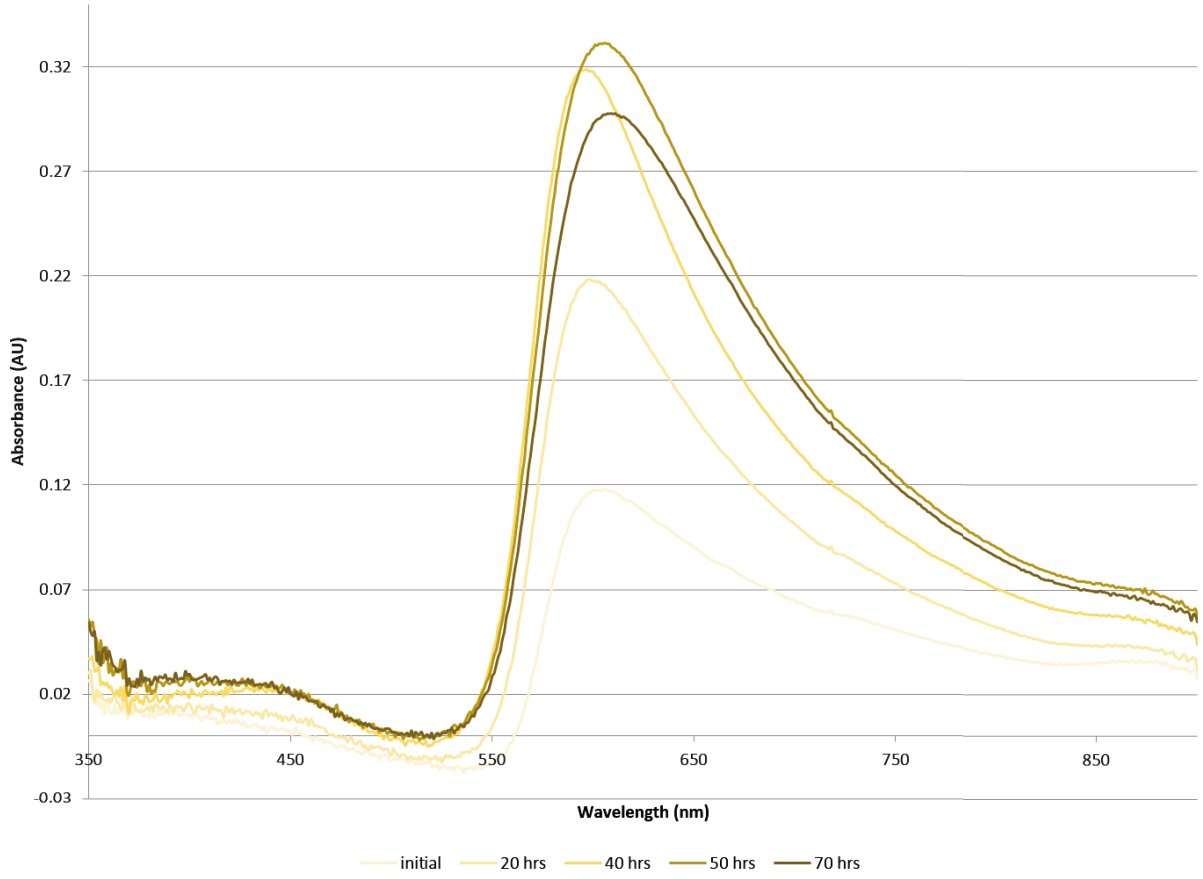


**Figure 5.5|** Change in UV-Vis spectrum over time as rings assemble on α-lipoic acid conjugated TMVcp. Solutions are blanked against matching concentration nanoparticle control solutions.

## 5.4 Dark-field spectroscopy and imaging

As was discussed in chapter 1, the permittivity is a complex function of wavelength. Absorption spectra of a solution of rings can only provide information on the imaginary component of the permittivity. By measuring the degree of scattering as a function of wavelength, a calculation of the complete complex permittivity is possible since both absorbed and scattered radiation is recorded as a function of wavelength.

In collaboration with Dr. Jennifer Chen at York University in Toronto, the extraction of dark field scattering spectra on solutions of nanoparticle rings has recently begun. This experiment incorporates a dark field microscope for imaging which is coupled to diode array for spectral

analysis. Ring solutions are plated on glass or indium tin oxide (ITO) slides functionalized with (3-aminopropyl)trimethoxysilane (APTMS) which increases the affinity of gold nanoparticles for the substrate resulting in a film. A typical experiment illuminates this film while collecting transmitted light at a 45° angle away from the incident beam. An advantage of utilizing 5 nm particles is that they are not expected to scatter light appreciably individually, and instead, must be present as plasmonically coupled structures in order to appear visible. Such aggregates appear as diffraction limited spots from which a spectrum of the aggregate can be extracted. Ideally, the visible aggregates are either ring structures, partial ring structures or clustered rings as is shown by TEM. A correlated system that allows the study of selected aggregates by scanning electron microscopy (SEM) as well as dark-field scattering is currently underway. This will allow the identification of the structure providing the recorded scattering spectrum.

Preliminary scattering data has been obtained for individual structures obtained from ring solutions at two different pH values (*Figure 5.6*). While some aggregates show a single peak centered around 500 nm, the majority produce a scattering profile that appears to consist of two overlapping modes, a peak centered at approximately 485 nm and a peak between 580-600 nm. The absorption spectra recorded of ring solutions corrected against matching nanoparticle controls for covalently templated rings are consistent with those of hydrogen-bond assembled rings in chapter 3.

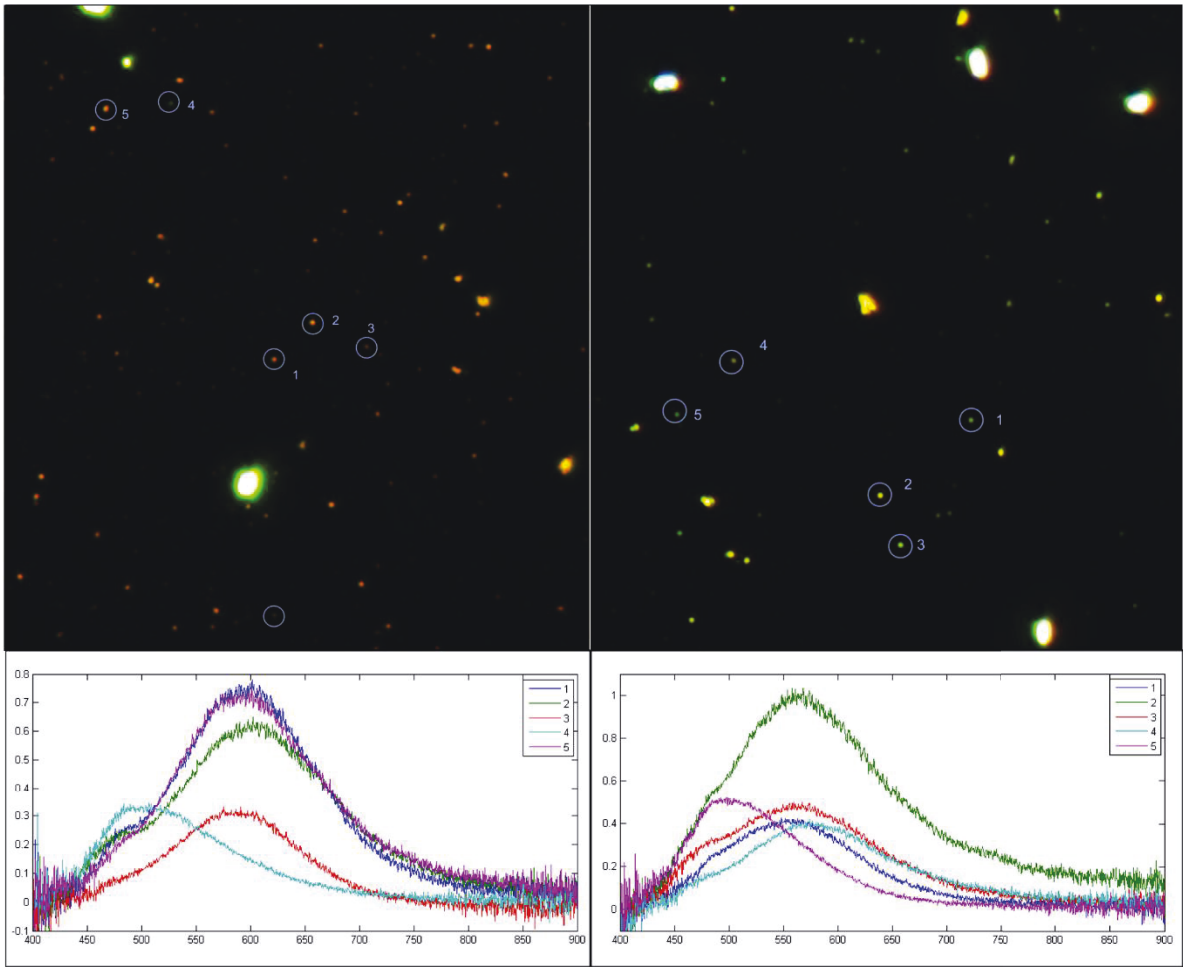


**Figure 5.6|** Dark-field imaging and spectra of diffraction limited spots located on a APTMS-functionalized glass substrate plated with an unpurified ring solution assembled at pH 7.0 (left) and pH 7.5 (right).

## 5.5 Methodologies

All substances were purchased at analytical grade with no further purification. Water used in all procedures was deionized using a Barnstead Diamond TII (Thermo Fisher) purification system. Monosodium phosphate, Disodium phosphate, sodium acetate, acetic acid and dithiothrietol (DTT) were purchased from Thermo Fisher Scientific (Pittsburgh, PA). Uranyl Acetate was purchased from SPI Supplies (West Chester, PA). All other chemicals were purchased from Sigma-Aldrich (St. Louis, MO)

Desalting and spin concentration was carried out using Corning Spin-X UF concentrators (VWR, Corning, NY) and unless otherwise specified, Specra/Por dialysis membranes (MWCO 3,500 kDa) were utilized for dialysis steps. All centrifugation was performed in a Sorvall RC6 Plus centrifuge.

**Assembly and purification of nanoparticle rings on α-lipoic acid functionalized TMV coat protein.** TMVcp was conjugated as described in chapter 4. BSPP-functionalized gold nanoparticles (synthesis detailed in chapter 3) were concentrated after synthesis from 10 mL to 2 mL. The pH and ionic strength of the nanoparticle solution was set using concentrated stocks of phosphate buffer. Conjugated TMVcp was added last to a final concentration of 0.4 µM which approximated a 5:1 ratio of gold nanoparticles to TMVcp.

Ring solutions were purified first by dialysis through in a 100 kDa MWCO cellulose acetate snake skin membrane (SpectraPor) followed by spin filtration using 100kDa MWCO Corning Spin-X UF concentrators with three buffer washes.

**Analysis of nanoparticle rings.** TEM samples were plated on 200-mesh carbon coated copper grids (Canemco, Lakefield, QC, Canada) for 5 minutes before wicking using filter paper and stained using 1% uranyl acetate or 2% phosphotungstic acid. Images were collected using a Philips CM200 TEM at 200kV or FEI Technai T12 at 120kV. UV-Vis spectra in the 200-800nm region were collected using a Cary 100 Bio instrument. Dark-field scattering spectra were recorded by Dr. Jennifer Chen at York University.

Analysis of UV-Vis and fluorescence data was carried out using MATLAB. TEM images were analyzed using ImageJ

## 5.6 Conclusion

Nanoparticle rings have been assembled on TMV coat protein conjugated to α-lipoic acid. Due to the poor conjugation efficiency noted in chapter 4, these rings do not possess the desired resilience which prompted this method of ring assembly. Fortunately, the tendency for BSPP-functionalized gold nanoparticles to form linear arrays allows partially assembled rings to 'fill in the gaps', resulting in virtually complete rings in unpurified rings solutions. These ring solutions display optical characteristics previously observed in hydrogen-bond templated rings in chapter 3 in both absorption and dark-field scattering spectra.

Due to the diffraction limited nature of surface optical techniques, the exact nature of the structures for which these spectra are recorded is currently unknown, however, by utilizing an ITO substrate, a correlated analysis is possible using scanning electron microscopy. An identifying mark can be placed on the substrate in the area of the measured spectrum which can be located in an SEM survey. These efforts are currently ongoing.

The nature of the extinction mode between 450-485 nm as a magnetic resonance is currently unclear. Theoretical models involving the various structures (both cleanly assembled rings and clustered rings) obtained in unpurified ring solutions are currently being pursued to elucidate the possible electronic mechanisms involved.

## Citations


1. Loweth, C. C. J., Caldwell, W. B. W., Peng, X., Alivisatos, a. P. & Schultz, P. G. DNA-Based Assembly of Gold Nanocrystals. *Angew. Chemie Int. Ed.* **38,** 1808–1812 (1999).

2. Fan, J. a *et al.* DNA-enabled self-assembly of plasmonic nanoclusters. *Nano Lett.* **11,** 4859–64 (2011).

3. Sellers, H., Ulman, A., Shnidman, Y. & Eilers, J. E. Structure and binding of alkanethiolates on gold and silver surfaces: implications for self-assembled monolayers. *J. Am. Chem. Soc.* **115,** 9389–9401 (1993).

4. Häkkinen, H. The gold-sulfur interface at the nanoscale. *Nat. Chem.* **4,** 443–55 (2012).

5. Sharma, J., Chhabra, R., Liu, Y., Ke, Y. & Yan, H. DNA-templated self-assembly of two-dimensional and periodical gold nanoparticle arrays. *Angew. Chem. Int. Ed. Engl.* **45,** 730–5 (2006).

6. Li, Z. Multiple thiol-anchor capped DNA-gold nanoparticle conjugates. *Nucleic Acids Res.* **30,** 1558–1562 (2002).

7. Zhang, X., Liu, B., Dave, N., Servos, M. R. & Liu, J. Instantaneous attachment of an ultrahigh density of nonthiolated DNA to gold nanoparticles and its applications. *Langmuir* **28,** 17053–60 (2012).

8. Bartczak, D. & Kanaras, A. G. Preparation of peptide-functionalized gold nanoparticles using one pot EDC/sulfo-NHS coupling. *Langmuir* **27,** 10119–23 (2011).

9. Soto, C. M. *et al.* Separation and recovery of intact gold-virus complex by agarose electrophoresis and electroelution: application to the purification of cowpea mosaic virus and colloidal gold complex. *Electrophoresis* **25,** 2901–6 (2004).

10. Loo, L., Guenther, R. H., Basnayake, V. R., Lommel, S. A. & Franzen, S. Controlled encapsidation of gold nanoparticles by a viral protein shell. *J. Am. Chem. Soc.* **128,** 4502–3 (2006).

11. Zon, V. B., Sachsenhauser, M. & Rant, U. Preparation of gold nanoparticle dimers via streptavidin-induced interlinking. *J. Nanoparticle Res.* **15,** 1974 (2013).

12. Aljabali, A. a. a. *et al.* Charge Modified Cowpea Mosaic Virus Particles for Templated Mineralization. *Adv. Funct. Mater.* **21,** 4137–4142 (2011).

13. Han, X., Goebl, J., Lu, Z. & Yin, Y. Role of salt in the spontaneous assembly of charged gold nanoparticles in ethanol. *Langmuir* **27,** 5282–9 (2011).

# Chapter 6
# *Azide-terminated TMVcp as a platform for click chemistry*


Abstract

TMV coat proteins modified with N-terminal azides (as described in Chapter 4) are utilized as a template in two instances. First, for functionalization by alkyne terminated polymers. These conjugates display abnormal assembly behavior as observed by TEM but the cause of this has not yet been fully evaluated.

The second application is the conjugation of TMV to DNA oligomers. TMVcp-DNA conjugates are utilized to bind gold nanoparticles functionalized with complimentary DNA strands, combining the structural complexity of a protein scaffold with the precision of DNA self-assembly.

## 6.1 Introduction

In 2001, Sharpless et al. described the development of a set of highly reproducible and selective chemical reactions for the rapid fusion of organic molecules through a heteroatom bridge1. These reactions, termed 'click chemistries', must be high yielding, regiospecific, easy to purify and widely applicable in many conditions. Such properties are achieved through a high thermodynamic preference for product formation. One of the most representative and well known reactions of this family is the copper-catalyzed Huisgen 1,3-dipolar cycloaddition of azides and alkynes. The copper-catalyzed azide-alkyne cycloaddition (CuAAC) combines two molecules possessing an azide and alkyne through a triazole bridge in a virtually quantitative fashion. Perhaps most striking is the inordinate insensitivity of this reaction to a wide variety of conditions, allowing its application in both organic and aqueous media, in liquid[2] and solid phase[3]. Combined with the relative inertness of azides and alkynes[4], the CuAAC reaction has an attractive orthogonal property that avoids laborious protection and deprotection steps.

The copper catalyst is instrumental in the progression of the reaction and must be available in a +1 oxidation state. While the body of information derived from mechanistic studies of the CuAAC is vast, a complete understanding of the mechanism remains obscured due to the complexity of the interaction of the copper ion with the alkyne during intermediate steps of the reaction *(Figure 5.1)*. In general, studies have suggested that multiple copper ions are involved in activating the alkyne and positioning the azide suitably for cycloaddition[5].

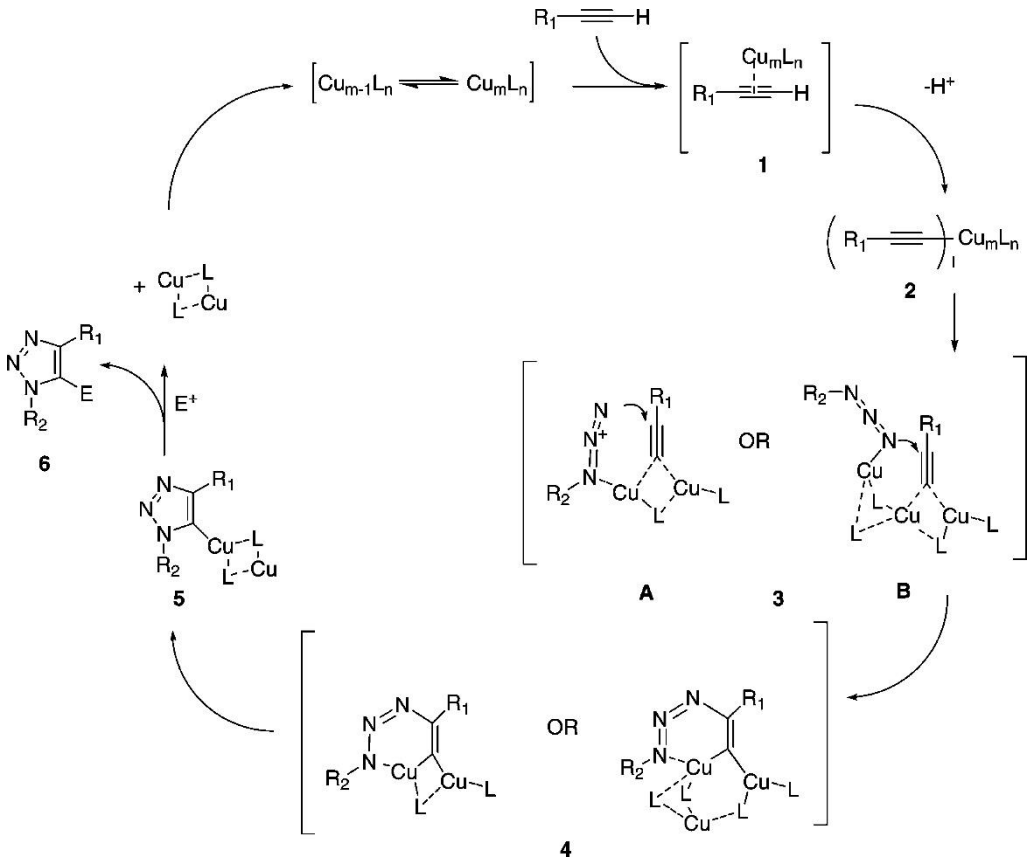


**Figure 6.1|** Mechanism of copper catalyzed azide-alkyne cycloaddition with possible intermediates[2]. © 2008 Reprinted with permission from ACS Publications.

While the copper-catalyzed cycloaddition can proceed adequately in the presence of the azide, alkyne and Cu(I) salt, several additives can accelerate the reaction and ensure quantitative efficiency. In aqueous solution, Cu(I) is relatively unstable and easily oxidized to Cu(II) or undergoes disproportionation to Cu(0) and Cu(II). This lability can be inhibited with the use of polytriazole ligands, such as Tris(3-hydroxypropyltriazolylmethyl)amine (THPTA), which stabilize the Cu(I) oxidation state upon complexation[6]. Copper in the +1 oxidation state can be supplied directly in the form of a salt, however, reactions tend to be slow and undergo undesired side reactions[3]. Increased robustness is provided by using a Cu metal with an oxidizing agent or Cu(II) salts with a reducing agent, the former method is comparatively slower due to the heterogeneity of the catalyst. The use of ascorbate as a reducing agent was initially avoided for bioconjugation due to the formation of reactive byproducts of ascorbate oxidation as well as the copper-mediated generation of reactive oxides[7]. However, recent studies screening various reaction conditions with coumarin azide have revealed that these detrimental effects can be

virtually eliminated by adding aminoguanidine to intercept oxidation products of ascorbate, and by maintaining a large concentration of ligand relative to copper to simultaneously stabilize the Cu(I) oxidation state and intercept reactive oxygen species[8].

The triazole bridging unit is inert to redox reactions and hydrolysis with electronic properties similar to a amide bond[9]. The ease of click chemistry and particularly CuAAC is appealing as a drug discovery tool for the synthesis of novel biomolecule conjugates that are generally difficult to modify with specificity due to the large density of functional groups they tend to display. A similar challenge asserts itself in the use of biomolecules for materials science. The synthetic paradigm of click chemistry is necessary in such systems where one wishes to chemically modify complex molecules in mild conditions. The field of polymer, dendrimer and other polymeric synthesis has already benefitted greatly from CuAAC[10] and this has inspired its use for biological molecules, such as in the functionalization of peptides[11] and the attachment fluorophores to oligonucleotides[12].

In this chapter we report the attachment of polylysine (PLYS) and polyethyleneoxide (PEG) to the N-terminus of TMVcp. The ultimate goal of this endeavor is to assert control over the natural self-assembly of the coat protein to form alternative ABAB assemblies of stacked disks through electrostatic attraction between the synthetic polymers (*Figure 6.3*). The integration of the complex properties of biomolecules with current synthetic materials is a popular endeavor with promising applications including the implementation of biocompatibility and metal-free catalysis[13].

In a collaboration with the Sleiman group at McGill University, we also describe the attachment of an alkyne functionalized oligonucleotide to the N-terminus of TMVcp. We hope that this virus-DNA hybrid system can provide a method for the assembly of gold nanoparticles functionalized with complimentary oligonucleotides into rings with diameters that are determined by the length of the oligonucleotide. This would provide a greater degree of geometric control over that offered by the coat protein itself, while still providing the structural benefits of a robust virus capsid protein.

## 6.2 Fluorecein alkyne derivative to probe TMVcp conjugate efficiency

Considering that both the synthetic polymers as well as the oligonucleotides we wished to attach to the TMVcp N-terminus are relatively large and dynamic molecules, it is conceivable that attempts to click these molecules may be hindered, not by the azide-conjugated TMVcp, but rather the dynamics and structure of these molecules themselves. To decouple these two factors to an extent, an alkyne modified fluorescein probe was utilized to determine if the azide-conjugated TMVcp could be accessed by a small molecule.

In this study 5-azidopentanoic acid (5-APA) conjugated to wild-type TMVcp synthesized in chapter 4 was 'clicked' to an alkyne derivative of fluorescein at pH 7.0. After removal of excess reagents by dialysis, the attachment of fluorescein to the TMV coat protein was evident by the appearance of peaks at 495 nm, 323 nm and 286 nm *(Figure 5.2)*.

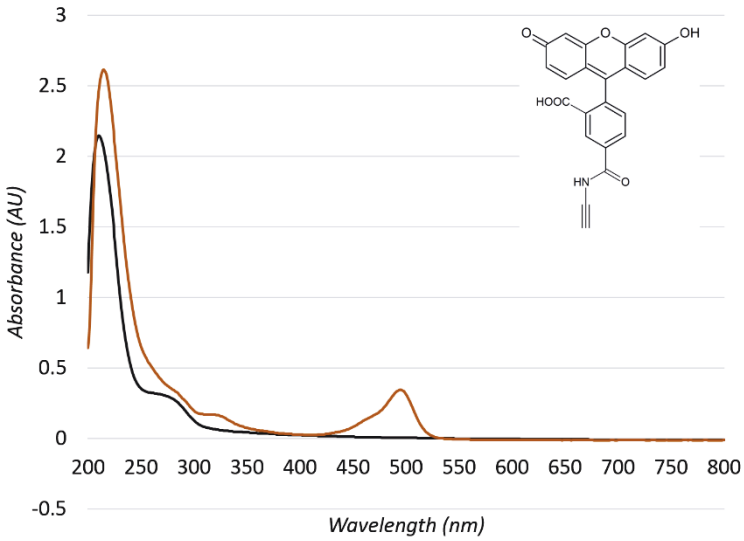


**Figure 6.2|** UV-Vis Absorption spectra of azide-TMVcp conjugated before (black) and after (orange) click reaction with alkyne-derivatized fluorescein.

Fluorescein exists as four differently charged species in aqueous solution; dianion, anion, neutral and cationic protolytic forms[14]. All four of these species contribute to the absorption spectrum of fluorescein and their relative populations are determined by pH, ionic strength and temperature. Therefore, in order to extract quantitative information on the number of 'clicked' dyes relative to the number of TMVcp molecules, fluorescein standards must be made at the exact conditions of the click reaction. This work is currently ongoing. Considering the highly efficient nature of CuAAC, it is expected that the yield of attached fluorescein will reflect the yield of TMVcp that was successfully conjugated by 5-APA in chapter 4, providing an alternate method to ESI-LCMS for determination of conjugation yield.

## 6.3 Functionalization of TMVcp with polylysine and polyethyleneoxide by CuAAC

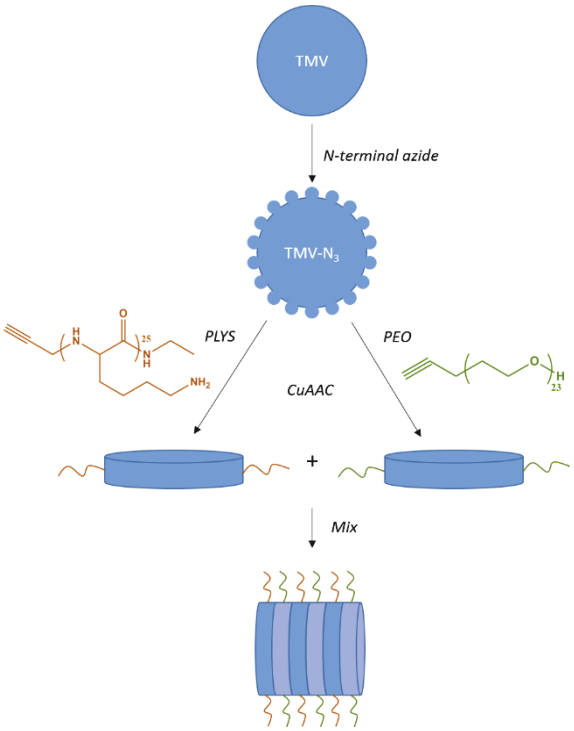


**Figure 6.3|** Schematic of ABAB assembly using TMVcp 20S functionalized with either PEO or PLYS.

There are several reports of the functionalization of viruses with synthetic polymers. The functionalization of cowpea mosaic virus with PEG resulting in a reduction of immunogenicity (the ability of a substance to provoke an immune response) in mice has been reported by Finn et al[15]. CPMV has also been functionalized with neoglycopolymers for recognition by glucose-binding protein concanavalin A[16]. Recombinant adenovirus has been similarly modified with PEG, resulting in a resistance to antibodies in mice[17]. While there are a few examples utilizing click chemistry for the modification of TMV coat protein[18,19], this author has not found any examples of the modification of TMVcp with synthetic polymers. We envisage that one could 'hijack' the natural self-assembly system of the TMV coat protein by modifying the external surface of the TMV 20S disk or helical rod using polyelectrolytes to direct the assembly of these units through electrostatic interaction. As an illustration, we report the attempted functionalization of TMV disks with either polyethyleneoxide or polylysine to drive an ABAB-type stacking of disks *(Figure 5.3)*. By conjugating a dye to one of the two modified disk types, one could assemble chromophores with fixed spacing between each disk. This project is a collaborative effort with the Kumaraswamy and Sengupta groups at the National Chemical Laboratory in Pune, India. These two groups provided alkyne-functionalized PEG (1052 g/mol) and PLYS (3283 g/mol) which we conjugate to the TMV-azide platform synthesized as described in Chapter 4.

In short, 5-azidopentanoic acid (5-APA) N-terminally functionalized wild-type TMVcp (wt-TMVcp) at either pH 5.7 as rods or pH 7.0 as disks are clicked to either alkyne functionalized

PEG or PLYS using Cu(II) sourced from copper sulfate and complexed to tris(3-hydroxypropyltriazolylmethyl)amine. The Cu(II) ion is reduced to Cu(I) by sodium ascorbate. Aminoguanidine is added to scavenge reactive oxygen species and protect the coat protein.

The conjugation of 5-APA to wt-TMVcp does not visibly alter the behavior of TMVcp as observed by TEM. However, the coat protein does display a significantly higher affinity for the carbon substrate of the TEM grid than its unconjugated counterpart. Likely related to this effect is the tendency for disks to adhere to the sides of rods as the sample dries on the grid, suggesting the promotion of inter-molecular interactions between the azides on the sides of the rods and the residues exposed on the faces of the disks.

After the click reaction, it is immediately apparent that reaction with either PEO or PLYS results in a significant change in TMVcp assembly behavior and stability, since click reactions that are allowed to proceed overnight result in precipitation of the conjugated protein. To avoid this, the reaction time was shortened to only a few hours before removing reactants through spin filtration. The protein shows no apparent changes by TEM after spin filtration, however, when allowed to incubate at room temperature overnight, abnormal structures and aggregates are observed depending on the pH at which the click reaction proceeds and the resulting polymer conjugates are incubated *(Figure 5.4)*.

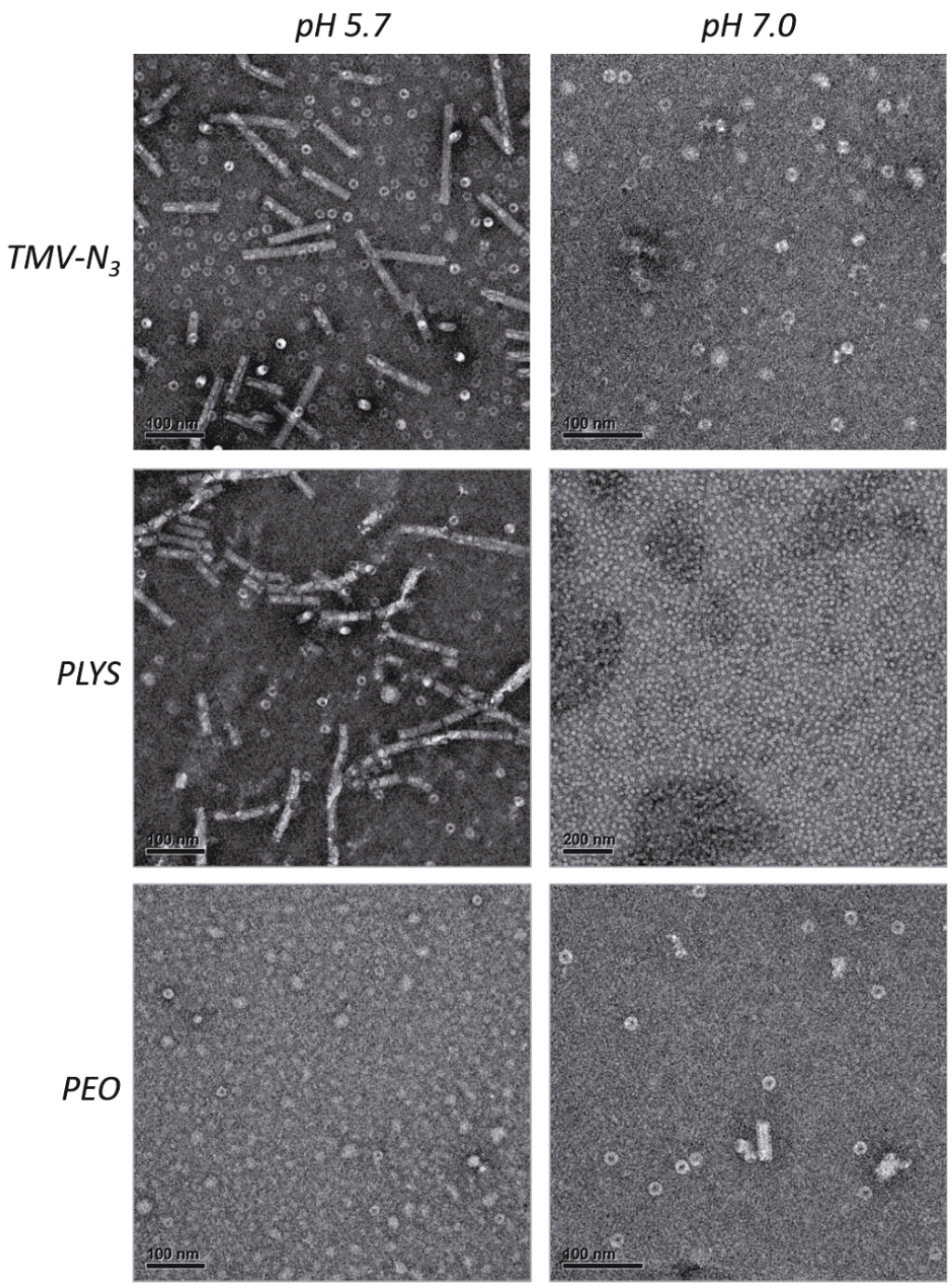


**Figure 6.4|** TEM images of TMVcp after CuAAC reaction, purification by spin filtration and 24 hour dialysis.

The most striking effect is that of polylysine modified TMVcp. At pH 5.7, unmodified wt-TMVcp exists mainly in the helical rod phase, with few instances of 20S disks. In contrast, within 24 hours of conjugation to PLYS, TMVcp rods appear segmented and the population of 20S disks in solution increases dramatically. We postulated that the attachment of PLYS at the N-terminus decreases the tendency for the coat protein to assemble helically, and the result is a slow depolymerization of the rods. Analyzing the TMVcp solution before and after the click reaction by circular dichroism supports this assertion *(Figure 5.5)*, revealing a significant change in ellipticity at 230 nm after attachment of the polymers.

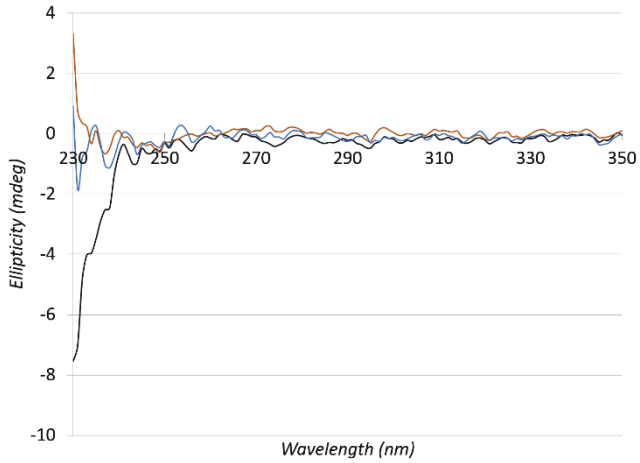


**Figure 6.5|** Circular dichroism of TMVcp conjugated to 5-APA (black), after click reaction with polylysine (orange) and with polyethylene oxide (blue).

However, control studies where all components of the click reaction are provided except for copper reveal a similar segmenting effect in the rods and an increase in disk population. If instead sodium ascorbate is omitted no such effect is evident and rods are intact. It appears that the disassembly behavior is not due to the coupling of PLYS to the TMV N-terminus but the presence of ascorbate in the solution itself, however it is unlikely that sodium ascorbate can influence the rod assembly of TMVcp so dramatically as it has been used extensively in the past for the metallization of TMV rods and such an effect has not been reported[20–22]. Another explanation is that PLYS may associate with TMVcp helices in a non-covalent manner and trigger a disassembly of rods through an inter-molecular mechanism which is prevented by the presence of copper-THPTA complex that remains adhered to TMVcp after filtration. As is discussed below, the presence of this complex has intriguing effects on assembly.

At pH 7.0, TMVcp remains as disks before and after reaction, however, some disks appear to have aggregated in various orientations on the TEM grid surface. Similar aggregates are observed in both controls where copper or ascorbate are absent *(Figure 5.6)* and so it may be

that this effect is due to non-covalent interactions between positively charged polylysine and the carboxylates prevalent over the TMVcp disk surface. It is conceivable that these polyelectrolytes can layer on top of the disk and behave as a 'glue' for other disks. On the other hand, one would expect disks wrapped in polymers to appear distinctly different with the stain used to visualize the protein under TEM, which is not the case. At both pH values, it is clear that TMVcp assembly is strongly influenced by the CuAAC reagents, which interferes with the determination of a successful conjugation taking place. The disassembly behavior at pH 5.7 cannot be resolved until the effect of each reagent on TMVcp is deconvoluted.

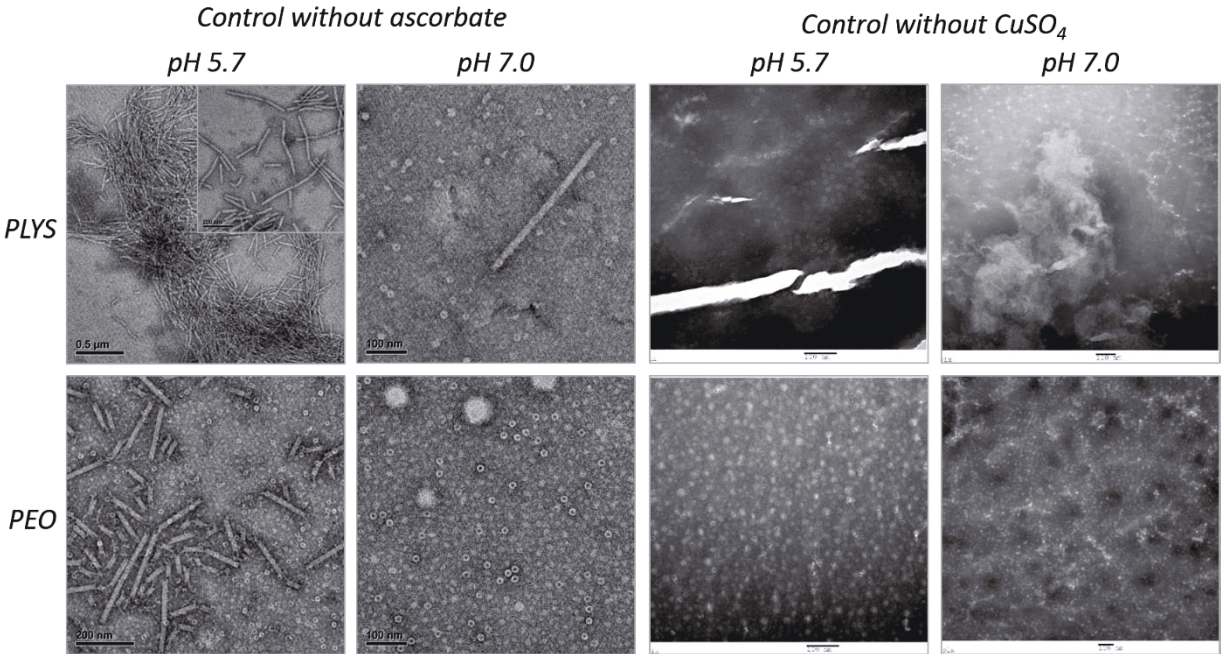


**Figure 6.6|** Control samples revealing the unexpected effects of sodium ascorbate and copper sulfate in the absence of reaction.

The conjugation of polyethyleneoxide to TMVcp showed similar effects. At pH 5.7, all rods are found to be completely disassembled except in the absence of ascorbate. There is a notable decrease in aggregations of disks compared to polylysine, however, there were also a larger number of amorphous aggregates observed under TEM. It is possible that PEO induces an aggregation of the coat proteins. This is supported by protocols which use PEO to precipitate proteins for purification[23], however, significantly larger concentrations of PEO are used.

It is clear that more detailed investigations must be carried out to elucidate the effects of PEO and PLYS with TMVcp. TEM cannot provide more information than confirming of the presence

of rods, disks or amorphous aggregates and thus studies that can evaluate the integrity of the protein subunit itself are necessary. One such study would involve monitoring the tryptophan fluorescence of TMVcp upon exposure to each of the click reaction components. Increases in fluorescence at 320-350 nm often suggest an unfolding of a protein as tryptophan fluoresces more intensely when exposed to the high dielectric constant of the buffer. Attempts to analyze conjugates using LC-ESI MS to observe the expected increase in mass of the TMVcp have failed to date. SDS-PAGE gel electrophoresis of the conjugates show no change in mobility compared to the azide-functionalized TMVcp and thus we currently expect that no click reaction is occurring at these conditions.

An observation worth noting is the intriguing effect that copper salts appear to have on the aggregation of TMV disks and rods. In controls forgoing sodium ascorbate (thus preventing the cycloaddition), TMVcp in disk phase at pH 7.5 was found to aggregate side-by-side into large islands. At pH 5.7, rods aggregated into 'spaghetti'-like clusters and also displayed a significant increase in length. Both these observations can be explained by the complexation of Cu(II) between coat proteins as salt-bridges, however, copper sulfate is first mixed in an excess of THPTA before mixing with TMVcp so it is unclear how this may occur with the steric bulk of this large ligand.

In conclusion, it is clear that the undesired effects of the reactants on TMVcp must be dealt with before we can proceed with the characterization of the protein-polymer conjugates. At this point, it is conceivable that the non-covalent interaction of the polymers with TMVcp make them unavailable for cycloaddition to the N-terminal azide. Future work will involve an exploration of various reactant concentrations in the hopes that lower concentrations of sodium ascorbate and alkyne-functionalized polymers may inhibit unwanted interactions. We note that a complete functionalization of all coat proteins in a disk is likely unnecessary to drive ABAB stacking and thus perhaps reacting at a polymer deficit will help resolve some of these issues.

## 6.4 TMVcp-DNA hybrids for templated DNA-NP conjugate assembly

The use of DNA-protein conjugates has proliferated mainly as a bioanalytical tool or to facilitate the assembly of biologically based nanostructures[24]. A highly sensitive immunoassay, the immuno-PCR, developed by Sano et al.[25] and used frequently in clinical diagnoses, involves the use of DNA-immunoglobulin conjugates which bind target antigens and allow their low-concentration detection through amplification of the attached DNA strand by PCR. DNA-streptavidin conjugates are commonly used to immobilize biotinylated proteins on subtrates for biochip sensor applications[26,27]. Oligonucleotides are often utilized as a bridge between proteins and inorganic materials such as nanoparticles. DNA-protein conjugates can be easily attached to nanoparticles functionalized with complimentary DNA sequences for distance controlled ligation of fluorescent proteins with plasmonic nanoparticles[28]. DNA-protein conjugates can also be used in conjunction with DNA origami scaffolds for the precise arrangement of functional proteins on various two-dimensional and three-dimensional geometries[29].

We wished to take advantage of the precise nature of oligonucleotide Watson-Crick base paring to the robust TMVcp disk scaffold to precisely arrange gold nanoparticles functionalized with complimentary oligonucleotides. The advantages of DNA self-assembly have been discussed extensively in chapter 2. The utilization of TMVcp as the scaffold removes the need to create complex 3D DNA origami structures to behave as substrates and potentially provides a cheaper alternative to traditional DNA-templated self-assembly which can be applied on a larger scale.

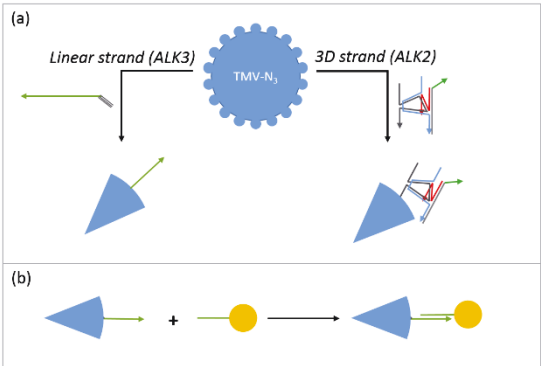


**Figure 6.7|** (a) Schematic for attachment of either the linear, flexible ALK3 oligonucleotide sequence or the 3D, rigid, ALK2 'rung'. (b) Schematic of subsequent attachment of DNA-nanoparticle conjugates possessing complimentary DNA sequence.

In this collaboration with the Sleiman group at McGill university, two alkyne-derivatized oligonucleotide structures were synthesized for

attachment to 5-APA conjugated TMVcp by CuAAC click chemistry *(Figure 5.7)*. The first is a basic linear oligonucleotide chain consisting of 20 nucleotides terminated by an alkyne at the 3' end (ALK3). The second is a system of four oligonucleotide chains which are assembled into a three-dimensional 'rung' (ALK2). This structure was expected to behave as an inflexible counterpart to ALK3, to avoid potential issues involving the unstructured nature of the linear oligonucleotide if they arose. ALK2 possesses an overhang which contains the recognition site for the DNA-nanoparticle conjugate whereas ALK3 in its entirety behaves as a recognition site.

In short, S123C TMVcp mutant functionalized with 5-APA is conjugated to either ALK2 or ALK3 using CuAAC click chemistry. After dialysis to remove excess reagents, nanoparticle-DNA conjugates possessing a sequence complimentary to ALK2 or ALK3 are mixed with the TMVcp-DNA hybrids to assemble rings. Preliminary results reveal possible assembly events utilizing the linear ALK3 strand *(Figure 5.8)*. These appear as single nanoparticle-TMVcp disk attachments with an edge-to-edge distance of 7.8 ±1.5 nm which coincides with the predicted 6.8 nm length predicted for the association of ALK3 with its complimentary sequence. The recent results showing the poor efficiency of N-terminal conjugation to the S123C mutant of TMVcp discussed in chapter 4 provide a likely reason for the low number of associations. Attempts to characterize TMVcp-DNA hybrids by ESI-LCMS have failed, showing a complete disappearance of even unconjugated TMVcp. Use of the rigid ALK2 sequence has shown no indication of nanoparticle assembly, the absence of even low-levels of association suggest that the alkyne moiety on the nucleotide structure may be too hindered for reaction with those N-termini modified with azide moieties.

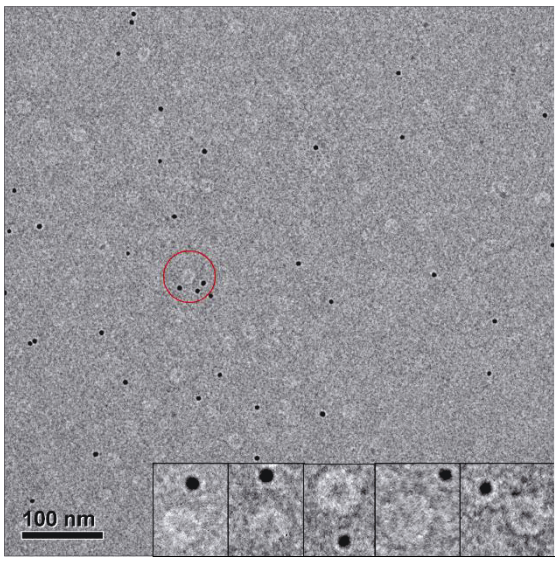


**Figure 6.8|** TEM images of possible assemblies utilizing ALK3 linear DNA conjugated to S123C TMVcp and mixed with nanoparticles conjugated to complimentary DNA strands.

Before appreciable progress can be made in this pursuit, the efficiency of the N-terminal conjugation for S123C TMVcp must be addressed. In the meantime, the use of wt-TMVcp may somewhat alleviate this issue as it appears to be easier to modify, however, using this species is complicated by its low stability at low concentration.

## 6.5 Methodologies

All substances were purchased at analytical grade with no further purification. Water used in all procedures was deionized using a Barnstead Diamond TII (Thermo Fisher) purification system. Monosodium phosphate, Disodium phosphate, sodium acetate, acetic acid were purchased from Thermo Fisher Scientific (Pittsburgh, PA). Uranyl Acetate was purchased from SPI Supplies (West Chester, PA). All other chemicals were purchased from Sigma-Aldrich (St. Louis, MO)

Desalting and spin concentration was carried out using Corning Spin-X UF concentrators (VWR, Corning, NY) and unless otherwise specified, Specra/Por dialysis membranes (MWCO 3,500 kDa) were utilized for dialysis steps. All centrifugation was performed in a Sorvall RC6 Plus centrifuge.

**Copper-catalyzed azide-alkyne cycloaddition of alkyne functionalized polymers to azide-modified TMVcp.** Azide-terminated wt-TMVcp (23 μM) dialyzed into phosphate buffer (pH 7.0, [I] = 0.1 M) or acetate buffer (pH 5.7, [I] = 0.1) is mixed with either alkyne-derivitized polylysine or polyethyleneoxide (230 μM) (1:10 TMVcp:polymer) in an Eppendorf tube. In a separate container, $CuSO_4$ (50 μM) and THPTA (250 μM) are mixed together then added to the TMVcp-polymer solution. Aminoguanidine (5 mM) is added followed by sodium ascorbate (5 mM) to initiate reaction. Controls omit either $CuSO_4$ or sodium ascorbate. Typical total reaction volumes are 250 μL. After two hours reagents are removed by spin filtration using Corning Spin-X concentrators with 5 kDa MWCO.

**Circular dichroism.** CD studies were performed at 25 °C on a JASCO J-810 spectropolarimeter using a 1 mm path length cuvette. Temperature was kept constant using the Peltier unit. Spectra were recorded from 400–230 nm with three acquisitions recorded for each spectrum.

**Copper-catalyzed azide-alkyne cycloaddition of alkyne-functionalized DNA to azide-modified TMVcp.** Azide-terminated S123C-TMVcp (14 μM) dialyzed into phosphate buffer (pH 7.0, [I] = 0.1 M) and mixed with either ALK2 or ALK3 alkyne-functionalized DNA (23 μM) in an Eppendorf tube. In a separate container, $CuSO_4$ (50 μM) and THPTA (250 μM) are mixed together then added to the TMVcp-polymer solution. Aminoguanidine (5 mM) is added followed by sodium ascorbate (5 mM) to initiate reaction. Reactions are allowed to proceed overnight before purification by dialysis.

**Attachment of DNA-functionalized nanoparticles to DNA-TMVcp conjugates.** 50 μL of DNA-NP conjugates containing the complimentary DNA sequence to either ALK2 or ALK3 (5.1 μM) is mixed with 250 μL of TMVcp (5 μM) functionalized with ALK2 or ALK3 respectively. Solutions are incubated for three days before analysis by TEM.

**Analysis of TMVcp-polymer conjugates and TMVcp-DNA templated nanoparticle rings by TEM.** TEM samples were plated on 200-mesh carbon coated copper grids (Canemco, Lakefield, QC, Canada) for 5 minutes before wicking using filter paper and stained using 1% uranyl acetate or 2% phosphotungstic acid. Images were collected using a Philips CM200 TEM at 200kV or FEI Technai T12 at 120kV.

## 6.6 Conclusion

While there are numerous intriguing applications for the use of TMVcp disks as templates for click chemistry, the pursuit is unquestionably hindered by the inefficiency of the N-terminal modification of TMVcp - the S123C mutant in particular. Current efforts are focused on addressing this issue. The TMVcp-polymer hybrids do not suffer this issue as acutely due to the higher efficiency of conjugations involving wt-TMVcp, however, numerous ambiguities exist in the cause of the anomalous self-assembly behavior observed which require a detailed analysis of the interaction of CuAAC click chemistry reagents with TMVcp.

## Citations


1. Kolb, H. C., Finn, M. G. & Sharpless, K. B. Click Chemistry: Diverse Chemical Function from a Few Good Reactions. *Angew. Chem. Int. Ed. Engl.* **40,** 2004–2021 (2001).

2. Meldal, M. & Tornøe, C. W. Cu-catalyzed azide-alkyne cycloaddition. *Chem. Rev.* **108,** 2952–3015 (2008).

3. Tornøe, C. W., Christensen, C. & Meldal, M. Peptidotriazoles on Solid Phase: [1,2,3]-Triazoles by Regiospecific Copper(I)-Catalyzed 1,3-Dipolar Cycloadditions of Terminal Alkynes to Azides. *J. Org. Chem.* **67,** 3057–3064 (2002).

4. Rostovtsev, V. V, Green, L. G., Fokin, V. V & Sharpless, K. B. A stepwise huisgen cycloaddition process: copper(I)-catalyzed regioselective "ligation" of azides and terminal alkynes. *Angew. Chem. Int. Ed. Engl.* **41,** 2596–9 (2002).

5. Bock, V. D., Hiemstra, H. & van Maarseveen, J. H. CuI-Catalyzed Alkyne-Azide "Click" Cycloadditions from a Mechanistic and Synthetic Perspective. *European J. Org. Chem.* **2006,** 51–68 (2006).

6. Chan, T. R., Hilgraf, R., Sharpless, K. B. & Fokin, V. V. Polytriazoles as copper(I)-stabilizing ligands in catalysis. *Org. Lett.* **6,** 2853–5 (2004).

7. S, F. Oxidative scission of plant cell wall polysaccharides by ascorbate-induced hydroxyl radicals. (1998). at <http://www.biochemj.org/bj/332/bj3320507.htm>

8. Hong, V., Presolski, S. I., Ma, C. & Finn, M. G. Analysis and optimization of copper-catalyzed azide-alkyne cycloaddition for bioconjugation. *Angew. Chem. Int. Ed. Engl.* **48,** 9879–83 (2009).

9. Kolb, H. C. & Sharpless, K. B. The growing impact of click chemistry on drug discovery. *Drug Discov. Today* **8,** 1128–1137 (2003).

10. Johnson, J. A., Finn, M. G., Koberstein, J. T. & Turro, N. J. Construction of Linear Polymers, Dendrimers, Networks, and Other Polymeric Architectures by Copper-Catalyzed Azide-Alkyne Cycloaddition "Click" Chemistry. *Macromol. Rapid Commun.* **29,** 1052–1072 (2008).

11. Punna, S., Kuzelka, J., Wang, Q. & Finn, M. G. Head-to-tail peptide cyclodimerization by copper-catalyzed azide-alkyne cycloaddition. *Angew. Chem. Int. Ed. Engl.* **44,** 2215–20 (2005).

12. Seo, T. S., Li, Z., Ruparel, H. & Ju, J. Click chemistry to construct fluorescent oligonucleotides for DNA sequencing. *J. Org. Chem.* **68,** 609–12 (2003).

13. Lutz, J.-F. & Börner, H. G. Modern trends in polymer bioconjugates design. *Prog. Polym. Sci.* **33,** 1–39 (2008).

14. Sjöback, R., Nygren, J. & Kubista, M. Absorption and fluorescence properties of fluorescein. *Spectrochim. Acta Part A Mol. Biomol. Spectrosc.* **51,** L7–L21 (1995).

15. Raja, K. S. *et al.* Hybrid virus-polymer materials. 1. Synthesis and properties of PEG-decorated cowpea mosaic virus. *Biomacromolecules* **4,** 472–6

16. Sen Gupta, S., Raja, K. S., Kaltgrad, E., Strable, E. & Finn, M. G. Virus-glycopolymer conjugates by copper(I) catalysis of atom transfer radical polymerization and azide-alkyne cycloaddition. *Chem. Commun. (Camb).* 4315–7 (2005). doi:10.1039/b502444g

17. Kreppel, F. & Kochanek, S. Modification of adenovirus gene transfer vectors with synthetic polymers: a scientific review and technical guide. *Mol. Ther.* **16,** 16–29 (2008).

18. Bruckman, M. a *et al.* Surface modification of tobacco mosaic virus with "click" chemistry. *Chembiochem* **9,** 519–23 (2008).

19. Yi, L. *et al.* Sulfonium alkylation followed by "click" chemistry for facile surface modification of proteins and tobacco mosaic virus. *Tetrahedron Lett.* **50,** 759–762 (2009).

20. Bromley, K. M., Patil, A. J., Perriman, A. W., Stubbs, G. & Mann, S. Preparation of high quality nanowires by tobacco mosaic virus templating of gold nanoparticles. *J. Mater. Chem.* **18,** 4796 (2008).

21. Balci, S. *et al.* Copper nanowires within the central channel of tobacco mosaic virus particles. *Electrochim. Acta* **51,** 6251–6257 (2006).

22. Knez, M. *et al.* Spatially Selective Nucleation of Metal Clusters on the Tobacco Mosaic Virus. *Adv. Funct. Mater.* **14,** 116–124 (2004).

23. Karasev, A. V. *Plant-produced Microbial Vaccines*. 130 (Springer Science & Business Media, 2009). at <http://books.google.com/books?id=jQWheUK9fWQC&pgis=1>

24. Niemeyer, C. M. Semisynthetic DNA-protein conjugates for biosensing and nanofabrication. *Angew. Chem. Int. Ed. Engl.* **49,** 1200–16 (2010).

25. Sano, T., Smith, C. & Cantor, C. Immuno-PCR: very sensitive antigen detection by means of specific antibody-DNA conjugates. *Science (80-. ).* **258,** 120–122 (1992).

26. Niemeyer, C. M., Sano, T., Smith, C. L. & Cantor, C. R. Oligonucleotide-directed self-assembly of proteins: semisynthetic DNA—streptavidin hybrid molecules as connectors for the generation of macroscopic arrays and the construction of supramolecular bioconjugates. *Nucleic Acids Res.* **22,** 5530–5539 (1994).

27. Niemeyer, C. Self-assembly of DNA-streptavidin nanostructures and their use as reagents in immuno-PCR. *Nucleic Acids Res.* **27,** 4553–4561 (1999).

28. Hazarika, P., Kukolka, F. & Niemeyer, C. M. Reversible Binding of Fluorescent Proteins at DNA–Gold Nanoparticles. *Angew. Chemie* **118,** 6981–6984 (2006).

29. Storhoff, J. J. & Mirkin, C. A. Programmed Materials Synthesis with DNA. *Chem. Rev.* **99,** 1849–1862 (1999).

# Chapter 7
# *Conclusions and future work*

## 7.1 Conclusions

This dissertation examined the use of virus coat proteins to organize nanostructured materials on a length scale that is costly and time-consuming using contemporary lithographic methods which pervade the field of nanostructure fabrication. Until the complexities of biomolecular interaction are further elucidated, the appropriation of biological machinery for the fabrication of synthetic structures will make complex nanostructures accessible through templated assembly. Methods that bridge top-down lithography and bottom-up self-assembly will in turn facilitate the introduction of these complex nanostructures into commercially viable technologies.

We demonstrated that the use of TMVcp disks to template nanoparticle ring assembly produces plasmonically coupled rings on a scale that has yet to be matched by other means. If artificial magnetism is confirmed to arise from such structures, they will be one of the first examples of a solution-phase metamaterial. The fact that such structures are fabricated in solution expedites large scale synthesis and increases their flexibility for integration into other systems. The optical properties of these structures can be tuned by varying the pH the assembly solution, which may be due to difference in facial binding due to protonation/deprotonation of Caspar pairs.

The conjugation of α-lipoic acid to the TMVcp N-terminus creates handles for the assembly of nanoparticles into rings with a higher level of geometric precision than those assembled on the TMVcp disk by inter-molecular attraction. The strength of covalent assembly appears to result in an increased resilience to rapid purification techniques such as spin filtration which will simplify characterization using ensemble spectroscopic measurements. While the yield and quality of rings assembled in this manner is currently hindered by the poor conjugation efficiency of the S123C mutant of TMVcp in the 20S disk phase, covalently bound rings do show structurally induced optical properties. Their assembly is driven by a combination of partial combination and a tendency for BSPP-functionalized nanoparticles to assemble adjacent to one another at higher salt concentrations. Preliminary measurements on individual nanostructures suggest that these optical phenomena arise from structural considerations, but this must be

confirmed with studies that are able to characterize individual structures such as electron energy loss spectroscopy and dark-field scattering.

While many questions remain as to the emergent optical properties these ring structures possess, much of this ambiguity lies in a lack of experimental data to support the several theoretical models that have been conceived by such groups as Norlander[1] and Engheta[2]. TMV coat protein and other biological templates provide a means to explore such theoretical predictions experimentally, guiding future endeavors in the fields of metamaterials and plasmonics.

In order to enhance the functional diversity of the TMVcp disk as a template, we functionalized the N-terminus with an azide moiety. This provided the means to conjugate alkyne-functionalized molecules through copper catalyzed azide-alkyne cycloaddition, a highly specific and flexible and orthogonal chemical reaction. With this method we attempted to conjugate two synthetic polymers; polylysine and polyethylene oxide. While both have revealed significant changes in the self-assembly behavior of wt-TMVcp, control studies have suggested the likely presence of unwanted interactions between the reactants and TMVcp itself. Requiring more detailed studies on the effects of each reactant on the self-assembly behavior of TMVcp. Successfully altering the self-assembly behavior of TMVcp introduces the potential for hierarchal assembly, such as the controlled arrangement of rings assembled on the face of TMVcp disks into arrays.

The attachment of oligonucleotides and three-dimensional DNA rungs to the TMV N-terminus using click chemistry intended to illustrate how the chemical diversity and resilience of a protein capsid can be combined with the highly precise and reproducible interactions of DNA self-assembly systems to create rings with tunable diameters. Unfortunately, this pursuit is stalled by the poor conjugation efficiency of the S123C TMVcp mutant when assembled as an achiral 20S disk. If successful, the enormous library of DNA origami structures becomes available for attachment in predictable geometries (such as rings for TMVcp disks). This powerful tool set has limitless possibilities for the arrangement of virus capsids into larger

assemblies, resulting in more complex templates and consequently, more complex metal nanostructures.

## 7.2 Future work

*TMV coat protein disks for non-covalent templated assembly*

The self-assembly of nanoparticles on a protein scaffold involving only inter-molecular interactions between nanoparticle ligands and specific residues on the protein is an attractive approach to ring assembly if only because it requires no modification of the protein itself. In chapter 3, the assembly of gold nanoparticles functionalized with BSPP ligands on TMVcp disks is likely driven by hydrogen bonding between sulfonyl oxygens and guanidinium hydrogens on arginine residues. This is a simple extension of arginine's typical role in proteins as a hydrogen bond donor for association to negatively charged molecules.

Isothermal titration calorimetry (ITC) will help further elucidate the interactions involved. Since the BSPP ligand predominantly determines the surface chemistry of the particles, one need not recreate the full conditions of binding for an ITC study. Titration with the ligand alone at matching buffer conditions is likely to suffice and may be advantageous since stoichiometric information can be extracted. TEM images taken after purification show a significant degree of surviving associations. This suggests that modifications to the method may lead to successful isolation of complete rings. Emphasizing mild techniques such as dialysis over potentially more disruptive techniques like centrifugal filtration may provide a solution.

Finally, the large presence of unassociated TMVcp disks indicates that higher nanoparticle:TMVcp ratios should be explored. If the population of rings is large enough one may be able to extract spectroscopic information from solutions of rings that are only partially purified by dialysis.

*N-terminal conjugation of TMV coat protein*

The use of NHS-esters is a powerful tool to modify primary amines and is especially useful in a protein such as TMVcp - which has no other easily exposed amines in the 20S disk phase. It is clear, however, that the current system of N-terminal conjugation of the S123C mutant of TMVcp is not viable. The obstruction of the N-terminus in the 20S disk phase cannot be surmounted by simple alterations to reaction conditions such as pH, ionic strength or temperature. The complexity of protein dynamics complicates the search for chemical additives that may alter the accessibility of the N-terminus, however, it is conceivable that salts such as calcium may encourage the transition into the chiral lock-washer phase since they have the capacity to form salt-bridges between Caspar pairs. This would result in the unravelling of the β-sheet adjacent to the N-terminus and extend it further into the solution as explained in chapter 4.

Failing this, site-directed mutagenesis can be utilized to extend the N-terminus. Francis has shown that the addition of only three additional residues can dramatically increase the reactivity of the N-terminus[3]. Another option is to use the wild-type species of TMVcp for conjugation. Unfortunately, wt-TMVcp disassembles at low concentrations. Also, chiral structures such as the helix and lock-washer are favored in acidic conditions where the nucleophilicity of the N-terminus will be subdued. This could be alleviated by using large ester:TMVcp ratios and thus further study is warranted.

*Modified TMV coat protein disks for covalent templated assembly*

The use of α-lipoic acid conjugated TMVcp is a promising alternative to the non-covalent assembly of chapter 3. The added geometric precision derived from 'side' assembly rather than 'face' assembly on the disk surface is clearly apparent. The potential increase in versatility obtained by functionalizing TMVcp with a terminal azide for copper catalyzed azide-alkyne cycloaddition will allow the assembly of other metals that can be stabilized with ligands possessing alkynes. Furthermore, such a template allows one to utilize the powerful toolset of DNA self-assembly to create structures of hierarchal complexity. The potential of both systems

is currently hampered by the limited conjugation efficiency detailed in chapter 4, therefore, addressing this issue will significantly promote these pursuits.

The study of rings that did assemble using single structure techniques such as dark-field scattering have supplied intriguing results. Other techniques capable of focusing on individual structures such as electron energy loss spectroscopy can further shed light on the electronic properties of sub-wavelength nanoparticle rings at this scale. Such a technique will also allow the study of partial rings and ring clusters individually, allowing one to determine the relative contributions of each in collective measurements such as UV-Vis spectroscopy. Collective measurements are necessary to evaluate metamaterial behavior because properties such as negative refractive index emerge as a result of the collective interaction of many such nanoparticle structures which behave as 'meta-atoms'.

## Citations


1. Nordlander, P., Oubre, C., Prodan, E., Li, K. & Stockman, M. I. Plasmon Hybridization in Nanoparticle Dimers. *Nano Lett.* **4,** 899–903 (2004).

2. Alù, a, Salandrino, a & Engheta, N. Negative effective permeability and left-handed materials at optical frequencies. *Opt. Express* **14,** 1557–67 (2006).

3. Obermeyer, A. C., Jarman, J. B. & Francis, M. B. N-terminal modification of proteins with o-aminophenols. *J. Am. Chem. Soc.* **136,** 9572–9 (2014).